

---

Electronic Theses and Dissertations, 2020-

---

2022

## Broadband Power Amplifier Design with High Power, High Efficiency and Large Back-off Range

Yuchen Cao  
*University of Central Florida*

Find similar works at: <https://stars.library.ucf.edu/etd2020>  
University of Central Florida Libraries <http://library.ucf.edu>

This Doctoral Dissertation (Open Access) is brought to you for free and open access by STARS. It has been accepted for inclusion in Electronic Theses and Dissertations, 2020- by an authorized administrator of STARS. For more information, please contact [STARS@ucf.edu](mailto:STARS@ucf.edu).

---

### STARS Citation

Cao, Yuchen, "Broadband Power Amplifier Design with High Power, High Efficiency and Large Back-off Range" (2022). *Electronic Theses and Dissertations, 2020-*. 1365.  
<https://stars.library.ucf.edu/etd2020/1365>

BROADBAND POWER AMPLIFIER DESIGN WITH HIGH POWER, HIGH EFFICIENCY  
AND LARGE BACK-OFF RANGE

by

YUCHEN CAO  
M.S Wichita State University, 2016

A dissertation submitted in partial fulfilment of the requirements  
for the degree of Doctor of Philosophy  
in the Department of Electrical and Computer Engineering  
in the College of Engineering and Computer Science  
at the University of Central Florida  
Orlando, Florida

Fall Term  
2022

Major Professor: Kenle Chen

© 2022 Yuchen Cao

## ABSTRACT

As modern communication system technology develops, the demand for devices with smaller size, higher efficiency, and larger bandwidth has increased dramatically. To achieve this purpose, a novel architecture of load modulated balanced amplifier (LMBA) with a unique load-modulation characteristic different from any existing LMBAs and Doherty power amplifiers (DPAs) was presented, which is named as Pseudo-Doherty LMBA (PD-LMBA). Based on a special combination of control amplifier (carrier) and balanced amplifier (peaking) together with proper phase and amplitude controls, an optimal load-modulation behavior can be achieved for PD-LMBA leading to maximized efficiency over extended power back-off range. More importantly, the efficiency optimization can be achieved with only a static setting of phase offset at a given frequency, which greatly simplifies the complexity for phase control. Furthermore, the co-operations of the carrier and peaking amplifiers in PD-LMBA are fully de-coupled, thus lifting the fundamental bandwidth barrier imposed on Doherty-based active load modulation.

However, since PD-LMBA has CA over-driving concerns, a new load-modulated power amplifier (PA) architecture, Asymmetric Load-Modulated Balanced Amplifier (ALMBA), is proposed based on PD-LMBA. And a subsequent improved type – continuous mode Hybrid Asymmetric Load Modulation Balanced Amplifier (H-ALMBA) has been developed. The two sub-amplifiers (BA1 and BA2) of the balanced topology in an LMBA are set as peaking amplifiers with different thresholds when cooperating with the control amplifier (CA) as the carrier, forming a hybrid load modulation behavior between Doherty and ALMBA. Compared to standard LMBA, the proposed H-ALMBA has a three-way load modulation with CA, BA1 and BA2 through proper amplitude control and phase alignment. Thus, this new mode offers extended power back-off range and enhanced back-off efficiency without suffering from difficulty and complexity in wideband design as imposed on three-way Doherty PAs. Based on comprehensive theoretical derivation and analy-



sis, the proposed H-ALMBA is designed and implemented using commercial GaN transistors and wideband quadrature couplers. Moreover, the continuous-mode matching is applied to the carrier amplifier achieving a maximized wideband efficiency at power back-off. This is the first time that continuous mode and ALMBA have been used in combination, and very satisfactory results have been achieved, exhibiting the highest 10-dB output power back-off (OBO) drain efficiency (DE) ever reported for wideband load-modulation PAs. The developed prototype experimentally demonstrates wide bandwidth from 0.55–2.2 GHz. The measurement exhibits an efficiency of 63–82% at peak output power, 51–62% for 5-dB OBO, and 50–66% for 10-dB OBO within the design bandwidth. When stimulated by a 20-MHz long term evolution (LTE) signal with 10.5-dB peak to average power ratio (PAPR), a 50–55% average efficiency is measured over the entire bandwidth at an average output power around 33 dBm.

## **ACKNOWLEDGMENTS**

I would like to express my appreciation to my advisor, Prof. Kenle Chen for his great support, hands-on teaching, an abundant amount of advice and encouragement throughout my Ph.D. study. Also, I would like to thank the members of my dissertation committee, Profs. Xun Gong, Mahdi Assefzadeh, Reza Abdolvand, and Stephen Kuebler for taking the time to review this work and provide valuable comments. I would also like to thank my friends, Mr. Haifeng Lyu, Dr. Wei Ouyang, and Dr. Junyi Huang for their constant friendship and support. In addition, I am extremely grateful to my wife, Shenwen Wu, my parents Chengbo Cao and Huizhen Xu, who endured this long journey with me, always offering support, tolerance and love. And lastly, I would like to thank the funding support from the National Science Foundation (NSF) CCSS program.

## TABLE OF CONTENTS

LIST OF FIGURES . . . . .	xi
LIST OF TABLES . . . . .	xix
CHAPTER 1: INTRODUCTION . . . . .	1
1.1 Motivation . . . . .	1
1.2 Dissertation Outline . . . . .	3
CHAPTER 2: PSEUDO-DOHERTY LOAD-MODULATED BALANCED AMPLIFIER .	4
2.1 Introduction . . . . .	4
2.2 Advanced Pseudo-Doherty LMBA Theory . . . . .	7
2.2.1 Review of LMBA . . . . .	8
2.2.2 Pseudo-Doherty LMBA Mode . . . . .	9
2.2.3 Amplitude Control of PD-LMBA . . . . .	12
2.2.4 Phase Control of PD-LMBA . . . . .	13
2.3 Practical Design of PD-LMBA for Optimized Efficiency over Extended Power Back-off Range . . . . .	15
2.3.1 Amplitude Control for Extended Power Back-off Range . . . . .	16

2.3.2 Phase Control for Maximized Back-off Efficiency . . . . .	17
2.4 Wideband RF-Input PD-LMBA Design . . . . .	19
2.4.1 Wideband BA Design . . . . .	21
2.4.2 Wideband CA Design . . . . .	22
2.4.3 Wideband BA-CA Phase Offset Design . . . . .	23
2.4.4 Overall Schematic and Simulation Results . . . . .	25
2.5 Implementation and Experimental Results . . . . .	27
2.5.1 Continuous-Wave Measurement . . . . .	29
2.5.2 Modulated Measurement . . . . .	33
2.6 Conclusion . . . . .	34
 CHAPTER 3: ASYMMETRICAL LOAD MODULATED BALANCED AMPLIFIER . .	 35
3.1 Introduction . . . . .	35
3.2 Asymmetrical LMBA Theory . . . . .	38
3.2.1 Generalized Asymmetrical LMBA Mode . . . . .	39
3.2.2 Pseudo-Doherty Biasing and Current-Generator Modeling . . . . .	40
3.2.3 Load Modulation Analysis of PD-ALMBA . . . . .	44
3.2.4 Amplitude and Phase Control of PD-ALMBA . . . . .	47

3.3 Verification using Emulated Ideal PD-ALMBA Model . . . . .	50
3.3.1 Emulation of Ideal PD-ALMBA Model . . . . .	50
3.3.2 Simulation Results . . . . .	52
3.4 Practical Design of Ultra-Wideband PD-ALMBA . . . . .	54
3.4.1 Design of Asymmetrical Balanced Amplifier . . . . .	55
3.4.2 Design of Control Amplifier . . . . .	58
3.4.3 BA-CA Phase Offset Design Over Ultra-Wide Bandwidth . . . . .	60
3.4.4 Overall Schematic and Simulation Results . . . . .	63
3.5 Implementation and Experimental Results . . . . .	64
3.5.1 Continuous-Wave Measurement . . . . .	65
3.5.2 Modulated Measurement . . . . .	69
3.6 Conclusion . . . . .	71
 CHAPTER 4: CONTINUOUS-MODE HYBRID ASYMMETRICAL LOAD-MODULATED BALANCED AMPLIFIER . . . . .	 73
4.1 Introduction . . . . .	73
4.2 Hybrid Asymmetrical LMBA Theory . . . . .	76
4.2.1 Generic Quadrature-Coupled Load Modulation . . . . .	77

4.2.2 Modeling of Carrier and Peaking Generators . . . . .	79
4.2.3 Load Modulation Analysis of H-ALMBA . . . . .	83
4.2.4 Amplitude and Phase Control of H-ALMBA . . . . .	87
4.2.5 Efficiency Enhancement of CA: Necessity and Approach . . . . .	90
4.3 Practical Design of Ultra-Wideband Continuous-Mode H-ALMBA . . . . .	92
4.3.1 Design of Control Amplifier in Continuous Mode . . . . .	93
4.3.2 Design of Balanced Amplifier with Asymmetrical Gate-Bias Setting . . . . .	96
4.3.3 Wideband BA-CA Phase Offset Design . . . . .	99
4.3.4 Overall Schematic and Simulation Results . . . . .	100
4.4 Implementation and Experimental Results . . . . .	103
4.4.1 Continuous-Wave Measurement . . . . .	104
4.4.2 Modulated Measurement . . . . .	108
4.5 Conclusion . . . . .	109
 CHAPTER 5: HIGHLY MINIATURIZED AND WIDEBAND 3-dB QUADRATURE HY- BRID USING SLOW-WAVE COUPLED LINE . . . . .	 111
5.1 Introduction . . . . .	111
5.2 Analysis of Symmetric Slow-Wave Coupling Structure . . . . .	113

5.3 Design Considerations of Slow-Wave Coupler . . . . .	115
5.4 Simulation and Measurement Results . . . . .	117
5.5 Conclusion . . . . .	119
CHAPTER 6: SUMMARY . . . . .	121
LIST OF REFERENCES . . . . .	122

## LIST OF FIGURES

Figure 2.1: Pseudo-Doherty LMBA overview: (a) schematic representation, (b) simulated efficiency profile comparison between Class-B amplifier, conventional DPA, asymmetrical DPA, and pseudo-Doherty LMBA (simulation is based on bare-die GaN devices to emulate the ideal transistor models). . . . .	5
Figure 2.2: Ideal generalized schematic of the output combining network for analyzing the proposed PD-LMBA architecture: (a) $P_{OUT} < P_{Max}/OBO$ , (b) $P_{OUT} \geq P_{Max}/OBO$ . . . . .	9
Figure 2.3: Dynamic BA and CA load impedances using the ideal generalized model ( $OBO = 10$ dB). . . . .	12
Figure 2.4: Simulation setup of the proposed PD-LMBA using realistic GaN transistors for analysis and verification. . . . .	14
Figure 2.5: Simulation results of PAE and gain verses output power at 2.3 GHz under different $V_{BA,GS}$ bias setting. . . . .	16
Figure 2.6: Determination of the optimal phase offset based on simulated large-signal performance at 2.3 GHz: using ideal CSP ( $= 33$ dBm) with various phase settings versus using optimized control amplifier ( $\theta_{ca} = -10^\circ$ ). . . . .	18
Figure 2.7: Equivalent-circuit model of CGH40010 showing the parasitics. . . . .	19
Figure 2.8: Simulated efficiency profile at 2.3 GHz under different $\theta_{ca}$ setting. . . . .	20



Figure 2.9: Simulated optimal BA-CA phase offset at different frequencies and design of TL-based wideband phase shifter for merging the BA and CA inputs. . . .	21
Figure 2.10: Power-swept CW simulation results of the PD-LMBA for best phase tuning setting at different frequencies. . . . .	23
Figure 2.11: Simulated drain DC current versus output power of BA (two BAs in total) and CA at 2.3 GHz. . . . .	25
Figure 2.12: Circuit schematic overview of designed PD-LMBA. . . . .	26
Figure 2.13: Fabricated pseudo-Doherty LMBA prototype. . . . .	27
Figure 2.14: Simulated power efficiency comparison between consistent $V_{GS,BA}$ , $V_{DS,CA}$ , and optimal $V_{GS,BA}$ (-5 to -4 V), $V_{DS,CA}$ (10 to 14 V) at $P_{max}$ and 10-dB OBO levels from 1.5 to 2.7 GHz. . . . .	28
Figure 2.15: Measured output power at various OBO levels from 1.5 to 2.7 GHz. . . . .	29
Figure 2.16: Measured power efficiency at various OBO levels from 1.5 to 2.7 GHz. . . .	30
Figure 2.17: Measured gain at various OBO levels from 1.5 to 2.7 GHz. . . . .	31
Figure 2.18: Power-swept measurement of efficiency and gain from 1.5 to 2.7 GHz. . . .	32
Figure 2.19: Measured output power and average efficiency with 9.5-dB-PAPR LTE signal from 1.5 to 2.7 GHz. . . . .	32
Figure 2.20: Output spectrum from modulated measurement using a 10-MHz 9.5-dB-PAPR LTE signal centered at 1.6, 1.8, 2.0, 2.2, 2.4 and 2.6 GHz. . . . .	33

Figure 3.1: Overview of pseudo-Doherty asymmetrical LMBA. . . . .	36
Figure 3.2: Ideal generalized schematic of the output combining network for analyzing the proposed PD-ALMBA architecture: (a) $P_{\text{OUT}} < P_{\text{max}}/\text{OBO}$ , (b) $P_{\text{OUT}} \geq$ $P_{\text{max}}/\text{OBO}$ . . . . .	38
Figure 3.3: Normalized currents of $I_c$ and $I_{b1}$ when $\beta_{\text{bo}} = 0.5$ for different PA modes, i.e., PD-LMBA, PD-ALMBA, and Doherty PA. . . . .	43
Figure 3.4: The dependence between $\sigma$ and $\alpha$ various given target OBO. . . . .	47
Figure 3.5: The continuum of BA1, BA2 and CA load modulations using the ideal gen- eralized model for $\text{OBO} = 10$ dB and various CA-LM ratio, $\alpha$ . . . . .	49
Figure 3.6: Emulated model setup of the proposed PD-ALMBA with bare-die GaN tran- sistors. . . . .	50
Figure 3.7: Simulated BA1, BA2 and CA currents using emulated PD-ALMBA model at 1.7 GHz for different LM ratios: a) $\alpha = 1$ , b) $\alpha = 1.5$ , c) $\alpha = 2$ . . . . .	51
Figure 3.8: Simulated BA and CA load modulation trajectories of different $\alpha$ at 1.7 GHz using emulation PD-ALMBA model. . . . .	53
Figure 3.9: Simulated power-swept efficiency of different $\alpha$ at 1.7 GHz. . . . .	54
Figure 3.10: (a) Simulation setup of the proposed PD-ALMBA using realistic GaN tran- sistors de-embedded with parasitic networks; (b) Design of TL-based wide- band phase shifter for merging the BA and CA inputs. . . . .	55
Figure 3.11: BA matching design at maximum power. . . . .	56

Figure 3.12: Determination of the optimal BA-CA phase offset based on dual-input circuit schematic in Fig. 3.6 at 1.0 GHz through phase-swept input stimulus of CA. . . . .	57
Figure 3.13: Simulated optimal BA1-CA phase offset at different frequencies. . . . .	58
Figure 3.14: Load modulation of $Z_{b1}$ and $Z_{b2}$ across the entire bandwidth for $\alpha = 1.5$ . . .	59
Figure 3.15: Simulated CA load-modulation behavior across the entire frequency band. .	60
Figure 3.16: Circuit schematic overview of designed PD-LMBA. . . . .	61
Figure 3.17: Power-swept CW simulation results of the designed PD-ALMBA with the best BA-CA phase setting at different frequencies: (a) drain efficiency, (b) PAE. . . . .	62
Figure 3.18: Fabricated PD-ALMBA prototype. . . . .	63
Figure 3.19: Measured drain DC current versus output power of BA1, BA2 and CA at 1.4 GHz, when $\alpha$ is set to 1 and 1.5, respectively. . . . .	65
Figure 3.20: Measured output power at various OBO levels from 0.55 to 2.2 GHz. . . . .	66
Figure 3.21: (a) Measured drain efficiency at various OBO levels from 0.55 to 2.2 GHz. (b) Measured PAE at various OBO levels from 0.55 to 2.2 GHz. . . . .	67
Figure 3.22: Measured gain at various OBO levels from 0.55 to 2.2 GHz. . . . .	68
Figure 3.23: Power-swept measurement of efficiency and gain from 0.55 to 2.2 GHz. . .	68

Figure 3.24: Measured average drain efficiency, output power and ACLR with 20-MHz 10.5-dB-PAPR LTE signal at 0.55, 0.7, 0.9, 1.1, 1.3, 1.5, 1.7, 1.9 and 2.1 GHz. . . . .	69
Figure 3.25: Output spectrum from modulated measurement using a 20-MHz 10.5-dB-PAPR LTE signal centered at 0.55, 0.7, 1.1, 1.3, 1.5, 1.7, 2.0 and 2.2 GHz. . . . .	70
Figure 3.26: Output spectrum comparison between PD-LMBA and ALMBA from modulated measurement using a 40-MHz 10.5-dB-PAPR dual-carrier LTE-A signal centered at 1.0 and 1.7 GHz. . . . .	71
Figure 4.1: H-ALMBA overview: (a) schematic and (b) simulated efficiency profile comparison between Class-B amplifier, conventional DPA, PD-LMBA, and H-ALMBA (simulation is based on bare-die GaN devices to emulate the ideal transistor models). . . . .	75
Figure 4.2: Generalized schematic of quadrature-coupled three-way load modulation (H-ALMBA): (a) low-power region (CA only), (b) Doherty region (CA+BA1), (c) ALMBA region (CA+BA1+BA2). . . . .	78
Figure 4.3: Comparison of fundamental currents (normalized to $I_{\text{Max,C/B}}$ ) of all three amplifiers in H-ALMBA and PD-LMBA modes. . . . .	80
Figure 4.4: Comparison of normalized fundamental voltages of each path in H-ALMBA and PD-LMBA mode. . . . .	82
Figure 4.5: Comparison of resistances of each path in H-ALMBA and PD-LMBA mode. . . . .	85

Figure 4.6: Carrier and peaking efficiency performances: a) PD-LMBA; b) proposed H-ALMBA. . . . .	88
Figure 4.7: Efficiency performance of the proposed H-ALMBA versus $\beta$ with $\beta_{lbo} = 0.5$ and different values of $\beta_{hbo}$ . . . . .	89
Figure 4.8: Efficiency performance of the proposed H-ALMBA versus back-off level with different $\beta_{lbo}$ and $\beta_{hbo}$ . . . . .	90
Figure 4.9: Gain performance of the proposed H-ALMBA versus back-off level with different $\beta_{lbo}$ and $\beta_{hbo}$ . . . . .	91
Figure 4.10: Comparison of CA designed with continuous Class-F/ $F^{-1}$ and Class-AB: (a) schematic diagram; (b) ideal peak efficiency comparison with the same power loss. . . . .	92
Figure 4.11: OMN design of CA: (a) schematic of the designed CA-OMN with continue-mode; (b) simulated matching results of the designed CA-OMN from 1.7 to 3.0 GHz on the Smith chart with reference impedance. . . . .	94
Figure 4.12: (a) Simulation setup of the proposed H-ALMBA using realistic GaN transistors for verification and the transistor parasitic network, (b) design of TL-based wideband phase shifter for merging the BA and CA inputs. . . . .	95
Figure 4.13: Simulated optimal BA1-CA phase offset at different frequencies. . . . .	96
Figure 4.14: Reciprocal turning-on sequence of BA1 and BA2 at different frequencies and its impact on CA load modulation and efficiency profile. . . . .	97
Figure 4.15: Circuit schematic overview of designed CM-H-ALMBA. . . . .	98

Figure 4.16: Simulation results of the designed H-ALMBA at 2.25 GHz: (a) fundamental current; (b) fundamental voltage; (c) drain plane load trajectory. . . . .	101
Figure 4.17: Power-swept CW simulation results of the designed H-ALMBA with the best BA-CA phase setting at different frequencies: (a) drain efficiency; (b) PAE. . . . .	102
Figure 4.18: Fabricated H-ALMBA prototype. . . . .	103
Figure 4.19: Measured output power at various OBO levels from 1.7 to 3.0 GHz. . . . .	104
Figure 4.20: Measured DE at various OBO levels from 1.7 to 3.0 GHz. . . . .	104
Figure 4.21: Measured gain at various OBO levels from 1.7 to 3.0 GHz. . . . .	105
Figure 4.22: Measured DE and gain versus output power from 1.7 to 3.0 GHz. . . . .	106
Figure 4.23: Measured PAE versus output power from 1.7 to 3.0 GHz. . . . .	107
Figure 4.24: Measured average DE, output power and ACLR with 20-MHz 9.5-dB-PAPR LTE signal at 1.7, 2.0, 2.2, 2.4, 2.6, 2.8 and 3.0 GHz. . . . .	108
Figure 4.25: Output spectrum from modulated measurement using a 20-MHz 9.5-dB-PAPR LTE signal centered at 1.8, 2.0, 2.2, 2.4, 2.6 and 2.8 GHz. . . . .	109
Figure 5.1: The entire series of quadrature-coupler-based PAs (CA: control amplifier, DPA: Doherty PA, LMBA: load modulated balanced amplifier). . . . .	112
Figure 5.2: The circuit size comparison of the proposed wideband 3-dB slow-wave coupler and conventional branch line coupler with the same performance. . . . .	113

Figure 5.3: The even and odd mode analysis of the equivalent lumped circuit model of symmetric coupled lines. . . . .	114
Figure 5.4: Diagram of the proposed compact slow-wave coupler. (a) top view, (b) enlarged of unit cell view, (c) side view. $h_1$ : dielectric thickness between top and mid layer; $h_2$ : dielectric thickness between mid and bottom layer. . .	116
Figure 5.5: (a) S-parameters simulated results with different $h_1$ (mm), $\epsilon = 3.55$ ; (b) S-parameters simulated results with different load impedance. . . . .	117
Figure 5.6: Photograph of fabricated 3-dB slow-wave quadrature hybrid. . . . .	118
Figure 5.7: Measured S-parameters and phase error of the 3-dB slow-wave quadrature hybrid. . . . .	119

## LIST OF TABLES

Table 2.1:	State-of-the-Art of Wideband Load-Modulated Power Amplifiers . . . . .	29
Table 3.1:	State-of-the-Art of Wideband Load-Modulated Power Amplifiers . . . . .	64
Table 4.1:	State-of-the-Art of Wideband Load-Modulated Power Amplifiers . . . . .	105
Table 5.1:	Comparison with State-of-the-Art 3-dB Slow-Wave Couplers . . . . .	120



# CHAPTER 1: INTRODUCTION

This chapter first introduces what new challenges RF power amplifiers face in the 5G era. Secondly, the advantages of LMBAs in meeting the requirements of modern wireless communication systems are introduced. Finally, the great potential of PD-LMBA and its iterative models in improving efficiency and expanding bandwidth is summarized. In the end, the outline of this dissertation is listed.

## 1.1 Motivation

The rapid evolution of wireless communications in the modern world has led to ever-increasing demands on higher data rates and lower system latency in communication links. Due to the scarcity of spectrum resources, the spectrum-efficient modulation schemes, such as high-order quadrature amplitude modulation (e.g., 1024QAM) and orthogonal frequency-division multiplexing (OFDM), have been widely exploited in cellular and wireless local area network (WLAN) communications systems. Besides the benefits of those techniques, they have also led to substantial increase of peak to average power ratio (PAPR) of signals, e.g., 7-8 dB in 4G versus  $> 9.5$  dB in 5G and WLAN IEEE 802.11ax [1, 2]. Amplification of such high-PAPR signals makes power amplifiers (PAs) suffer from substantial efficiency degradation. On the other hand, due to the communications band proliferation, the wireless spectrum has been significantly expanding towards higher frequencies beyond the conventional range from 0.7–2.7 GHz in the 2G-4G era. As a result, the operational bandwidth of a single PA is desired to be as wide as possible, in order to minimize the number of PAs on a wireless platform for reducing the cost, space, and system complexity.

Enhancement of PA efficiency primarily relies on two types of techniques, i.e., supply modula-

tion (also known as envelope tracking) and load modulation. Given the bandwidth limitation and complexity in system operation of envelope tracking [3], load modulation has attracted increasing interest, and a variety of load-modulation architectures have been proposed and employed in realistic systems, including Doherty PA (DPA) [4, 5, 6], out-phasing PA [7, 8, 9, 10], and varactor-based dynamic load modulation [11, 12, 13, 14, 15]. However, conventional load-modulation techniques are facing difficulties in efficiently transmitting the high-PAPR signals and in extending to wider bandwidth. For example, the standard DPA only offers 6 dB of back-off power range, while the bandwidth is strongly limited by the quarter-wave inverter embedded in its circuit schematic. Despite recent advances in terms of wideband asymmetrical DPAs [16, 17, 18], distributed DPAs [19, 20], and multi-way DPAs [21, 22], to maintain maximized efficiency over extended power back-off range and meanwhile over broadened frequency span still remains a major challenge. Therefore, to enable energy efficient and wideband communications for future generations, there is an urgent demand to discover a new type of load-modulation PA fundamentally breaking the efficiency-bandwidth compromise.

Recently, a new PA architecture, load modulated balanced amplifier (LMBA) has been demonstrated, exhibiting an effective method for performing load modulation over wide bandwidth [23, 24, 25, 26, 27, 28]. By injecting an external signal into the isolation port of the output quadrature coupler, the load impedances of BA devices can be controlled with the variation of this signal's amplitude and phase, leading to the load modulation behavior and enhanced back-off efficiency. Moreover, by introducing a CA generating the control signal and by merging its input with BA, the single-input (or RF-input) LMBA is formed [24, 29]. The LMBA can be further incorporated with Doherty-like combination of BA (carrier) and CA (peaking), leading to Doherty-like load modulation behavior [30]. However, it is noted that the power back-off range is not fully expanded beyond the 6-dB range for the existing LMBA designs [28, 25], while the back-off efficiency optimization relies on concurrent amplitude and phase controls [31, 25, 28]. Such a control scheme requires

dynamic phase tuning that could increase the system-level complexity.

## 1.2 Dissertation Outline

This dissertation explores the advantages of using PD-LMBA and its iterative architecture to achieve large back-off range, high efficiency, high bandwidth power amplifiers. Chapter 2 presents the initial model of PD-LMBA. Chapter 3 shows asymmetric LMBA as a solution to PD-LMBA over-driving issue, and improve the linearity. Chapter 4 introduces the H-ALMBA that sequentially turns on three sub-PAs to maximize the average efficiency. This chapter also discusses the way to use continue-mode Class F to further improve fallback efficiency. In Chapter 5, the realization of an ultra-compact broadband quadrature coupler using slow-wave techniques to enable LMBA integration is presented. Finally, a summary is given in Chapter 6.

## **CHAPTER 2: PSEUDO-DOHERTY LOAD-MODULATED BALANCED AMPLIFIER**

This chapter is based in part on the previously published article listed below. I have permission from my co-authors and publishers to use the work listed below in my dissertation. [“Pseudo-Doherty load-modulated balanced amplifier with wide band- width and extended power back-off range,” IEEE Trans. Microw. Theory Techn., vol. 68, no. 7, pp. 3172–3183, Jul. 2020.].

### **2.1 Introduction**

The rapid evolution of wireless communications in the modern world has led to ever-increasing demands on higher data rates and lower system latency in communication links. Due to the scarcity of spectrum resources, the spectrum-efficient modulation schemes, such as high-order quadrature amplitude modulation (e.g., 1024QAM) and orthogonal frequency-division multiplexing (OFDM), have been widely exploited in cellular and wireless local area network (WLAN) communications systems. Besides the benefits of those techniques, they have also led to substantial increase of PAPR of signals, e.g., 7-8 dB in 4G versus  $> 9.5$  dB in 5G and WLAN IEEE 802.11ax [1, 2]. Amplification of such high-PAPR signals makes power amplifiers (PAs) suffer from substantial efficiency degradation. On the other hand, due to the communications band proliferation, the wireless spectrum has been significantly expanding towards higher frequencies beyond the conventional range from 0.7–2.7 GHz in the 2G-4G era. As a result, the operational bandwidth of a single PA is desired to be as wide as possible, in order to minimize the number of PAs on a wireless platform for reducing the cost, space, and system complexity.

Enhancement of PA efficiency primarily relies on two types of techniques, i.e., supply modula-

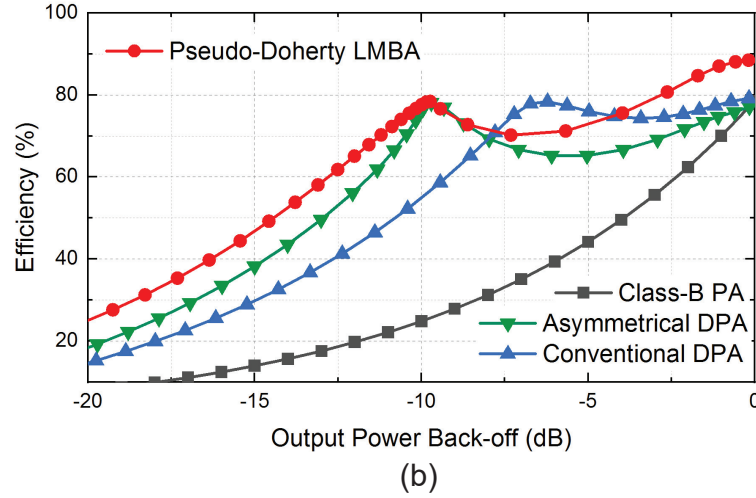
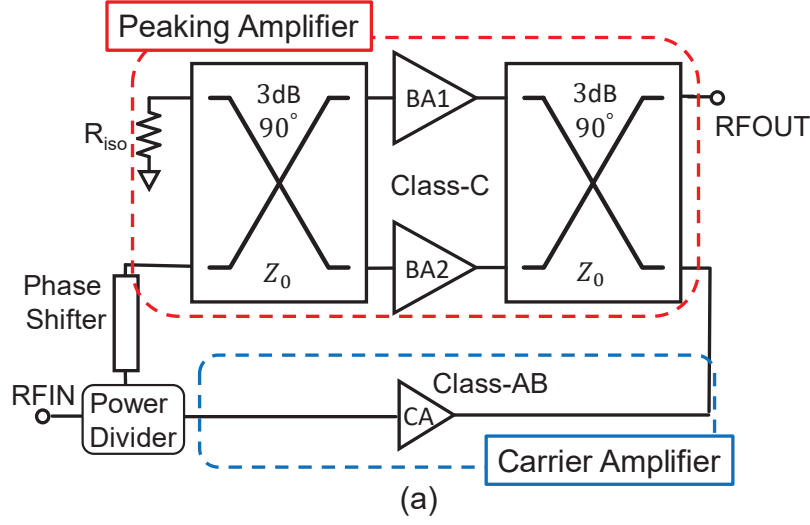


Figure 2.1: Pseudo-Doherty LMBA overview: (a) schematic representation, (b) simulated efficiency profile comparison between Class-B amplifier, conventional DPA, asymmetrical DPA, and pseudo-Doherty LMBA (simulation is based on bare-die GaN devices to emulate the ideal transistor models).

tion (also known as envelope tracking) and load modulation. Given the bandwidth limitation and complexity in system operation of envelope tracking [3], load modulation has attracted increasing interest, and a variety of load-modulation architectures have been proposed and employed in realistic systems, including DPA [4, 5, 6], out-phasing PA [7, 8, 9, 10], and varactor-based dynamic load modulation[11, 12, 13, 14, 15]. However, conventional load-modulation techniques are facing

difficulties in efficiently transmitting the high-PAPR signals and in extending to wider bandwidth. For example, the standard DPA only offers 6 dB of back-off power range, while the bandwidth is strongly limited by the quarter-wave inverter embedded in its circuit schematic. Despite recent advances in terms of wideband asymmetrical DPAs [16, 17, 18], distributed DPAs [19, 20], and multi-way DPAs [21, 22], to maintain maximized efficiency over extended power back-off and meanwhile over broadened frequency span still remains a major challenge. Therefore, to enable energy efficient and wideband communications for future generations, there is an urgent demand to discover a new type of load-modulation PA fundamentally breaking the efficiency-bandwidth compromise.

Recently, a new PA architecture, load modulated balanced amplifier (LMBA), has been demonstrated exhibiting an effective method for performing load modulation over wide bandwidth [23, 24, 25, 26, 27, 28]. By injecting an external signal into the isolation port of the output quadrature coupler, the load impedances of BA devices can be controlled with the variation of this signal's amplitude and phase, leading to the load modulation behavior and enhanced back-off efficiency. Moreover, by introducing a CA generating the control signal and by merging its input with BA, the single-input (or RF-input) LMBA is formed [24, 29]. The LMBA can be further incorporated with Doherty-like combination of BA (carrier) and CA (peaking), leading to Doherty-like load modulation behavior [30]. However, it is noted that the power back-off range is not fully expanded beyond the 6-dB range for the existing LMBA designs [28, 25], while the back-off efficiency optimization relies on concurrent amplitude and phase controls [31, 25, 28]. Such a control scheme requires dynamic phase tuning that could increase the system-level complexity.

Based on the classic LMBA theory [23] and the Doherty-like RF-input LMBA method [24, 25], this paper redesigns the LMBA architecture, as shown in Fig. 2.1(a). By setting the balanced amplifier (BA) as the peaking and CA as the carrier, a unique Doherty-like LMBA mode is discovered different from any existing LMBAs and DPAs, which is named Pseudo-Doherty LMBA

(PD-LMBA). It is for the first time revealed that the operations of BA and CA in this re-defined LMBA are functionally independent and decoupled. This unprecedented load-modulation mechanism circumvents the difficulties in wideband implementation of active load modulations, e.g., Doherty or out-phasing, which are all based on coupled interaction between multiple amplifiers. Moreover, with proper settings of BA-CA power scaling ratio and phase offset, the power back-off range of PD-LMBA can be greatly extended beyond the 6 dB of conventional DPA [32, 33] without compensating the back-off efficiency like asymmetrical DPA [16, 17], as depicted in Fig. 2.1(b). Meanwhile, it is important to emphasize that at a given frequency, the optimized back-off efficiency can be achieved with only a static setting of phase offset, and the wideband phase shifting between BA and CA can be easily implemented using a transmission line. These features minimize the circuit and system complexity. Based on the established PD-LMBA theory, a prototype is physically developed and experimentally demonstrated, exhibiting state-of-the-art performance in terms of bandwidth, power back-off range, and efficiency. In order to comprehensively exhibit the PD-LMBA theory, it will be analyzed in detail in Sec. 4 with analytical derivation, which will be further validated by practical design in Sec. 4 and experimental demonstration in Sec.4. The consistency between theory, ideal-model simulation (Fig. 2.1(b)), and practical design proves that the PD-LMBA theory can be generalized to any design based on this architecture.

## 2.2 Advanced Pseudo-Doherty LMBA Theory

Based upon the recent reported LMBA theory[23], a new LMBA mode is proposed in conjunction with a novel Doherty-like cooperation of control amplifier (main) and balanced amplifier (peak-ing), which leads to an optimized load-modulation behavior if proper amplitude and phase controls are performed. With such a unique pseudo-Doherty load-modulation characteristic, this new type of LMBA is theoretically analyzed in this chapter.

### 2.2.1 Review of LMBA

The LMBA described in [23] is derived from a convectional BA architecture [34] with two amplifiers combined in 90° out-of-phase using two classical quadrature hybrids at input and output. The LMBA differs from a standard BA in circuitry that the isolation port of the output coupler is not terminated to a resistor of characteristic impedance,  $Z_0$ , while a control signal is injected therein instead. With two symmetrical balanced amplifiers (BA1 and BA2) and the control signal, the behavior of LMBA can be considered as three excitation sources driving the output quadrature coupler, and it can be analytically described using impedance matrix given by

$$\begin{bmatrix} V_1 \\ V_2 \\ V_3 \\ V_4 \end{bmatrix} = Z_0 \begin{bmatrix} 0 & 0 & +j & -j\sqrt{2} \\ 0 & 0 & -j\sqrt{2} & +j \\ +j & -j\sqrt{2} & 0 & 0 \\ -j\sqrt{2} & +j & 0 & 0 \end{bmatrix} \begin{bmatrix} I_1 \\ I_2 \\ I_3 \\ I_4 \end{bmatrix} \quad (2.1)$$

where  $I_2 = I_b$  and  $I_4 = -jI_b$  representing the input currents from BA1 and BA2, while  $I_3 = jI_c e^{j\theta}$  denoting the current from control signal source [23], as shown in Fig. 2.1 (a).

Qualitatively speaking, due to the symmetry of quadrature coupler, the injected control signal is split equally into two halves appearing at the drain of the PA of each branch, which interact with the output signals generated by these two branch PAs leading to load modulation behavior. Using the matrix operation illustrated in Eq. (4.1), the impedances of BA1 and BA2 can be calculated as

$$Z_{BA1} = Z_{BA2} = Z_0 \left( 1 + \frac{\sqrt{2}I_c e^{j\theta}}{I_b} \right). \quad (2.2)$$

where  $I_b$  is the magnitude of BA currents,  $I_c$  the magnitude of CA current, and  $\theta$  the phase of the control path [23].



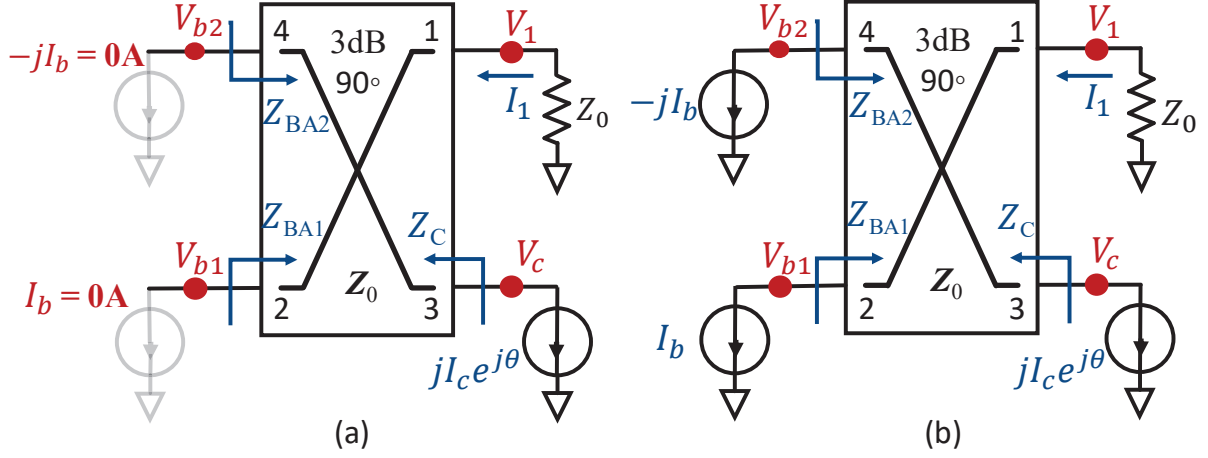


Figure 2.2: Ideal generalized schematic of the output combining network for analyzing the proposed PD-LMBA architecture: (a)  $P_{OUT} < P_{Max}/OBO$ , (b)  $P_{OUT} \geq P_{Max}/OBO$ .

While the original LMBA requires dual inputs, the single-input (or RF-input) LMBA has been proposed and demonstrated [24, 29]. The RF-input LMBA uses a CA instead of an independent control signal power (CSP). The CA shares the same RF input with the BA, and the input power is splitted to BA and CA at a given ratio through a dedicated power divider. The CA supplies control power into the isolation port of the output coupler. The load impedance of BAs is dependent on both the power (i.e., current) and phase of the control signal generated by CA. The operation of LMBA is primarily dependent on the following three aspects: a) amplitude control of CA, which can be designed with proper power dividing ratio at the RF input node and the peak power ratio between BA and CA; b) phase control of CA, which can be realized through a properly defined static phase offset,  $\theta_0$  [29], and a dynamically tunable phase  $\Delta\theta$  [31].

### 2.2.2 Pseudo-Doherty LMBA Mode

In the RF-input Doherty-like LMBA described in [30], the BA is biased to Class-AB acting as the carrier amplifier, and the CA is biased to Class-C as the peaking amplifier. This cooperation of BA

and CA exhibits a standard Doherty-like behavior with load-modulation from peak power to 6-dB back-off. In this design, the carrier-peaking combination of BA and CA is swapped targeting for extended range of output back-off (OBO), e.g., up to 10 dB, and enhanced back-off efficiency. To theoretically analyze the PD-LMBA, its operation is divided into the following three regions:

- **Low-Power Region** ( $P_{\text{OUT}} < P_{\text{Max}}/\text{OBO}$ ): When the PA is operating at low power level below the predefined target OBO power, the BA is completely turned off, i.e.,  $I_b = 0$ , as depicted in Fig. 2.2(a). In this case, the output power is only generated by the CA. According to Eq. (2.2), the impedances of BA1 and BA2 are thus equal to  $\infty$ ; a further derivation using the matrix operation in Eq. (4.1) indicates a CA impedance of  $Z_0$ :

$$\begin{aligned} Z_{\text{BA1,LP}} &= Z_{\text{BA2,LP}} = \infty; \\ Z_{\text{C,LP}} &= Z_0. \end{aligned} \tag{2.3}$$

In this region, the overall LMBA efficiency is equal to the efficiency of CA, which increases towards maximum as the CA power saturates at the target OBO power.

- **Back-off Region** ( $P_{\text{Max}}/\text{OBO} \leq P_{\text{OUT}} < P_{\text{Max}}$ ): Once the power is increased to the target OBO level, the CA should reach to its saturation, leading to  $I_c = I_{c,\text{Max}}$ . As the power further increases, the BA is turned on and  $I_b$  starts to increase from 0 towards  $I_{b,\text{Max}}$ , as illustrated by Fig. 2.2(b). Since the loading of CA remains to be  $Z_0$  as calculated using Eq. (4.1), the saturation of CA is maintained, while  $I_c$  remains its maximum value of  $I_{c,\text{Max}}$ . In this back-off region, the load modulation behavior of BA1 and BA2 as well as the CA impedance are

given by

$$\begin{aligned} Z_{\text{BA1,BO}} = Z_{\text{BA2,BO}} &= Z_0 \left( 1 + \frac{\sqrt{2} I_{c,\text{Max}} e^{j\theta}}{I_b} \right); \\ Z_{\text{C,BO}} &= Z_0. \end{aligned} \quad (2.4)$$

In this region, the CA remains saturated with the highest efficiency, while BA's efficiency can also be significantly boosted through load modulation. As a result, an enhanced back-off efficiency of the overall LMBA can be achieved.

- **Saturation Region** ( $P_{\text{OUT}} = P_{\text{Max}}$ ): As the power increases to the saturation of BA, the CA and BA are saturated simultaneously. In this condition, the saturation load impedance of BA1, BA2, and CA are as follows:

$$\begin{aligned} Z_{\text{BA1,SAT}} = Z_{\text{BA2,SAT}} &= Z_0 \left( 1 + \frac{\sqrt{2} I_{c,\text{Max}} e^{j\theta}}{I_{b,\text{Max}}} \right); \\ Z_{\text{C,SAT}} &= Z_0. \end{aligned} \quad (2.5)$$

The ratio of  $I_{c,\text{Max}}/I_{b,\text{Max}}$  is dependent on the OBO range, and this ratio becomes smaller as OBO increases. At this saturation region, the entire LMBA achieves the maximum efficiency.

It is important to note that the loading of CA is constantly  $Z_0$  across all three regions. In comparison with Doherty PA, this unique feature eliminates the necessity of impedance inverter connected to the main amplifier, fundamentally breaking the bandwidth limitation imposed on Doherty PA. Meanwhile, unlike the main amplifier in Doherty PA, the load impedance of CA is not affected by the off-state impedance of peaking amplifier (i.e., BA), leading to significantly reduced complexity for wideband design [35, 36]. Compared to the sequential amplifier with no load modulation that compromises PA efficiency at  $P_{\text{Max}}$  [18, 37, 38], PD-LMBA realizes the BA load modulation

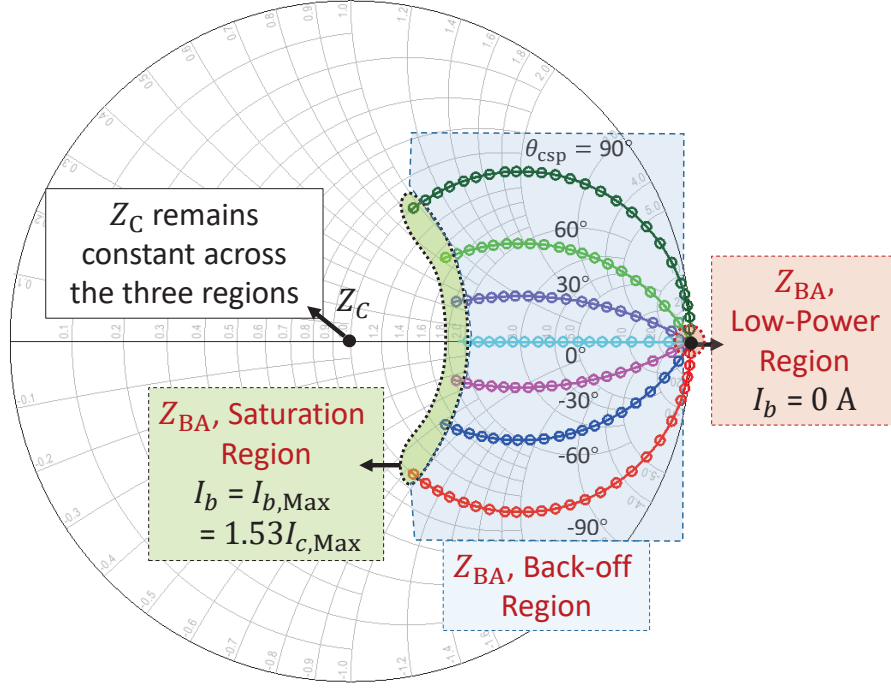


Figure 2.3: Dynamic BA and CA load impedances using the ideal generalized model (OBO = 10 dB).

through a special combination of BA and CA, which maintains a high efficiency throughout  $P_{\text{Max}}$  and the target OBO. The overall operation of PD-LMBA primarily relies on the amplitude and phase control of the main balanced amplifier through the control amplifier, which is discussed in detail in the following subsections.

### 2.2.3 Amplitude Control of PD-LMBA

As indicated by Eq. (2.4), the amplitude control of PD-LMBA is mainly determined by the term of  $I_{C,\text{Max}}/I_b$ . In terms of the PD-LMBA operation, the BA needs to be turned on at the pre-determined back-off power, where the CA reaches to its saturation simultaneously. Using the ideal model in

Fig. 2.2, the current scaling ratio between CA and BA is determined by the target OBO range:

$$\begin{aligned} \frac{1}{2}I_{c,\text{Max}}^2 \times Z_0 &= \frac{\frac{1}{2}I_{c,\text{Max}}^2 \times Z_0 + 2 \times (\frac{1}{2}I_{b,\text{Max}}^2 \times R_{\text{BA1,SAT}})}{\text{OBO}}; \\ I_{b,\text{Max}} &= \frac{\sqrt{2 \times \text{OBO}} - \sqrt{2}}{2} I_{c,\text{Max}}. \end{aligned} \quad (2.6)$$

In the above Eq. (3.20),  $R_{\text{BA1,SAT}}$  is the real part of  $Z_{\text{BA1,SAT}}$ . Practically, this BA-CA current scaling ratio can be transformed to the scaling ratio of transistor sizes of BA and CA. After determination of  $I_{c,\text{Max}}/I_{b,\text{Max}}$  according to a specific OBO (e.g.,  $I_{c,\text{Max}}/I_{b,\text{Max}} = 1/1.53$  for 10 dB of OBO), the amplitude control of the load modulation is governed by the turn-on point of BA, which mainly depends on two factors: 1) the gate bias voltage of the BA  $V_{\text{GS,BA}}$ , 2) the power dividing ratio between BA and CA. Both of these two factors will be considered together in the practical design.

#### 2.2.4 Phase Control of PD-LMBA

As indicated by Eqs. (2.3)-(2.10), the balanced amplifier is equivalent to the peaking amplifier in Doherty PA topology, in terms of the boundary points (e.g.,  $\infty$  and  $Z_0$ ) of the corresponding load modulation trajectory. Meanwhile, the trajectory connecting these two boundary points is solely determined by the phase of the CSP, i.e.,  $\theta = \theta_{\text{csp}}$ , given the fixed  $I_{c,\text{Max}}/I_{b,\text{Max}}$  ratio determined using Eqs. (3.20) with a specific target OBO. Fig. 2.3 shows load trajectory of BA with a variation of  $\theta_{\text{csp}}$  for OBO of 10 dB. Unlike the asymmetrical Doherty PAs [39, 16, 40, 17], the load modulation of BA, as the peaking amplifier of PD-LMBA, can be maintained along the real axis by setting  $\theta_{\text{csp}}$  to  $0^\circ$ . It is important to emphasize that this constantly resistive load trajectory is the optimal solution as explained by the classical Class-B loadline theory [38]. Such a load-modulation behavior ideally ensures a maximized back-off efficiency of the PD-LMBA, which can be considered the major advantage over asymmetrical Doherty PA for extension of dynamic power range.

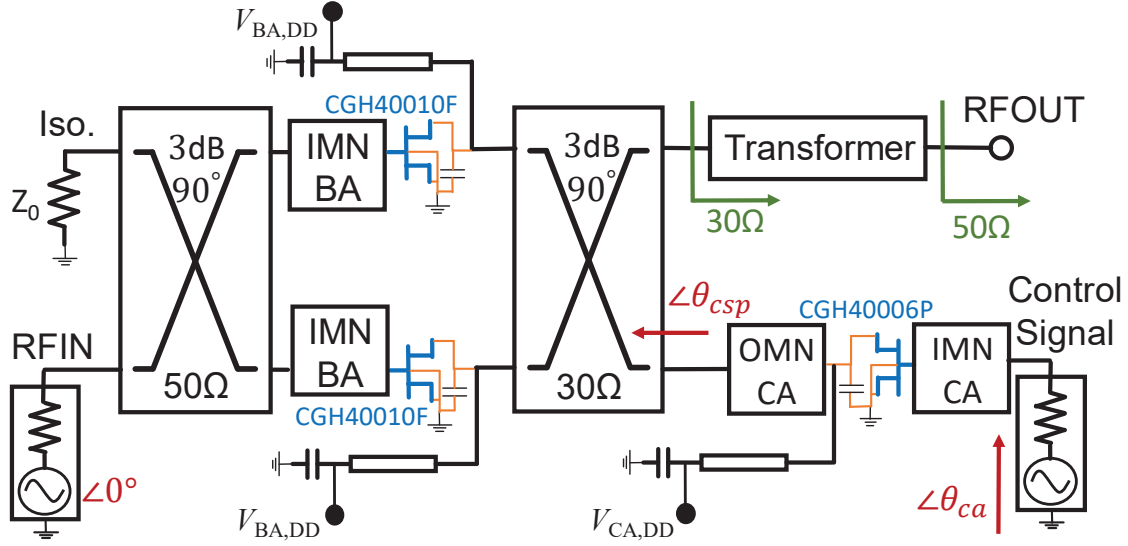


Figure 2.4: Simulation setup of the proposed PD-LMBA using realistic GaN transistors for analysis and verification.

It is also surmised that there is no need to dynamically change the phase of CA as a function of power, which has been necessary in other reported LMBAs [23, 41, 42]. This unique characteristic is highly desired for RF-input LMBA designs, in which the dynamic phase control is difficult as compared to the dual-input LMBA design.

In summary, the PD-LMBA architecture proposed in this paper primarily has four advantages over the other reported LMBAs and other load-modulation techniques: 1) The power asymmetry between carrier and peaking amplifiers can be easily realized for achieving extended power back-off range, since the BA with two PAs combined is naturally stronger in power generation than the single-branch of CA; 2) As the carrier amplifier, CA is loaded with a constant impedance ideally not affected by the off-state impedances of BA1 and BA2, which significantly simplifies the complexity of broadband design without having to control the load trajectory of the carrier amplifier over a wide frequency range; 3) The cooperation of BA and CA in PD-LMBA ensures an

optimized load modulation trajectory of the BA, leading to the maximized efficiency over the entire extended power back-off range; 4) At any given in-band frequency, the optimal load modulation behavior can be achieved only by setting a static phase offset between BA and CA, thus minimizing the circuit and system complexity.

### 2.3 Practical Design of PD-LMBA for Optimized Efficiency over Extended Power Back-off Range

The PD-LMBA theory presented in Sec. 4 is based on ideal circuit components where the transistors are modeled as ideal current sources, while the effect of realistic components (e.g., parasitics of transistors) need to be carefully considered for implementation of the theory. This section focuses on the design of PD-LMBA using realistic circuit components, aiming at achieving the highest possible efficiency over extended dynamic power range (10 dB as targeted in this design).

Following the PD-LMBA theory and ideal schematic (Fig. 2.2), a practical circuit of PD-LMBA is established using realistic GaN transistors, as the schematic illustrated in Fig. 2.4. Similar to the matching scheme presented in [42], the BA matching is realized through a combination of non-50- $\Omega$  quadrature coupler and bias line. This direct connection of transistor and coupler simplifies the load-modulation control of the realistic BAs [42] without being affected by excessive output matching networks. To better explain the PD-LMBA design in terms of amplitude control and phase control, the design starts with separated inputs of BA and CA, while these two independent sources will be replaced by a unified RF-input together with a power divider in the actual prototype development.

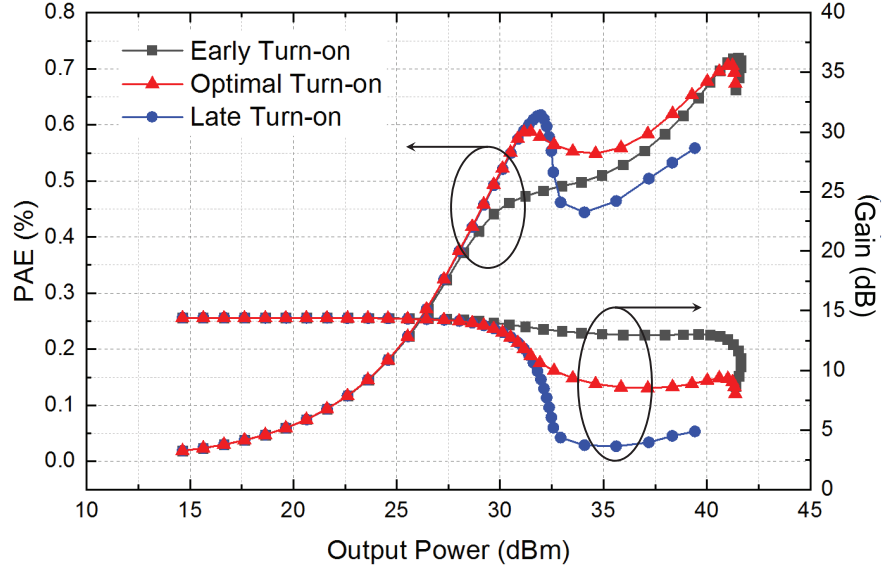


Figure 2.5: Simulation results of PAE and gain verses output power at 2.3 GHz under different  $V_{BA,GS}$  bias setting.

### 2.3.1 Amplitude Control for Extended Power Back-off Range

Based on the PD-LMBA operation described in Sec. 4, the amplitude control consists of two essential parts: 1) determination of current/power scaling ratio between BA and CA, 2) saturation of CA (in Class-AB) and turn-on of BA (in Class-C) simultaneously at the target power back-off.

The maximum saturated power of CA is determined by the target OBO range and the overall maximum output power:

$$P_{CA,SAT} = \frac{P_{Total,SAT}}{OBO}. \quad (2.7)$$

$P_{Total,SAT}$  denotes the total maximum power generated by the entire LMBA, which combines the saturation power from BA and CA:

$$P_{Total,SAT} = P_{BA,SAT} + P_{CA,SAT}. \quad (2.8)$$



In this practical design with GaN transistors, the actual  $P_{CA,SAT}$  can be realized through proper selection of CA device size (6-W GaN transistor, Wolfspeed CGH40006P) and reduced drain bias voltage [31] for extended OBO range of 10 dB. The maximum power of BA can be determined as

$$P_{BA,SAT} = (OBO - 1)P_{CA,SAT}. \quad (2.9)$$

With the large target OBO, the high BA power can be achieved by using larger-sized devices (10-W GaN transistor, Wolfspeed CGH40010F) together with full drain bias voltage and by combining the power of BA1 and BA2.

For the two variables governing the turn-on of BA, i.e., BA gate bias voltage and the input power dividing ratio, it is practically found that the effect of  $V_{GS,BA}$  plays a dominant role. By setting the power dividing ratio between BA and CA to 1 : 1 (a ratio used in many reported RF-input LMBAs [24, 29]), the turn-on point of BA can be controlled solely through properly choosing the depth of Class-C bias. Fig. 2.5 shows the effect of BA turn-on point on the LMBA's efficiency versus power behavior. The highest power-added efficiency over the entire power back-off range can be achieved only through optimal turn-on setting of BA.

### *2.3.2 Phase Control for Maximized Back-off Efficiency*

As discussed in Sec. 4 and illustrated in Fig. 2.3, there is an optimal phase setting of CA that leads to the optimal load modulation trajectory and maximized efficiency. With the on-chip and package parasitics of realistic transistors, the optimal load trajectory of GaN devices in BA at the package plane must deviate from the ideal purely-resistive load trajectory. Thus, a non-0° of control phase can be utilized to compensate this effect. In order to find the optimal control phase, an ideal phase-swept RF source with constant control signal power ( $CSP = 33$  dBm) is

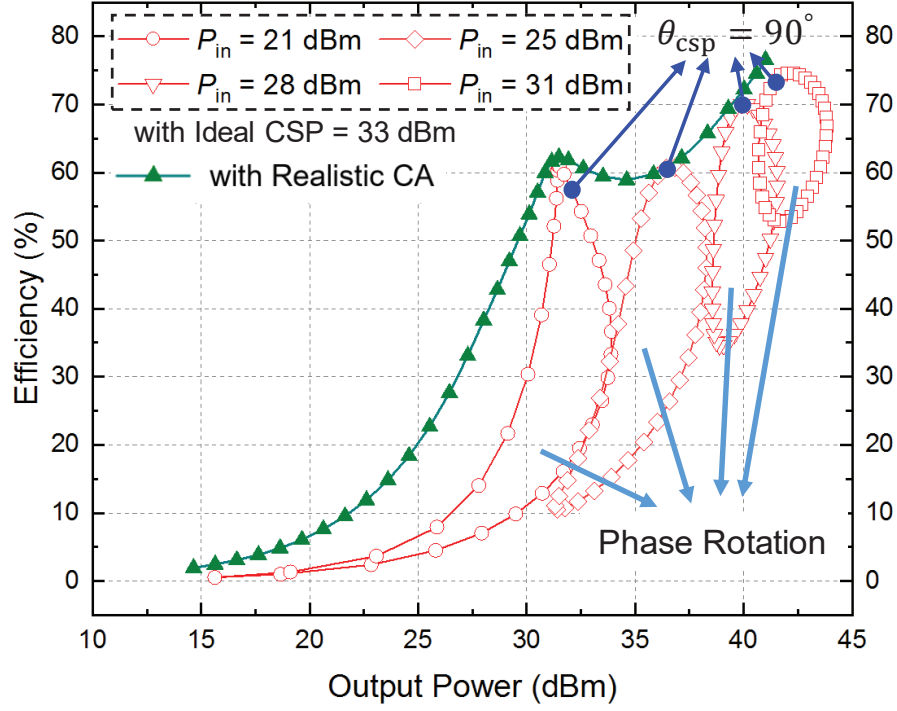


Figure 2.6: Determination of the optimal phase offset based on simulated large-signal performance at 2.3 GHz: using ideal CSP (= 33 dBm) with various phase settings versus using optimized control amplifier ( $\theta_{ca} = -10^\circ$ ).

fed into the isolation port replacing the actual CA. Assuming 70% of CSP efficiency, the overall LMBA efficiency is extracted with different BA input power under 2-W of CSP through  $360^\circ$  phase rotation ( $10^\circ$  of step size), as shown by the red curve in Fig. 2.6. It is important to point out that the highest efficiency points over the entire power back-off range correspond to a nearly constant control phase of  $\theta_{csp} = 90^\circ$ , in comparison with the large variation of efficiency-optimal phase as presented in [23, 42]. The simulation results well verify the proposed PD-LMBA theory. Such an efficiency optimization with only static phase offset is not only applicable to the particular circuitry in Fig. 2.4, but it can also be expanded to all possible PD-LMBA circuit topologies.

With the realistic GaN-based CA connecting to the isolation port of the output quadrature coupler,

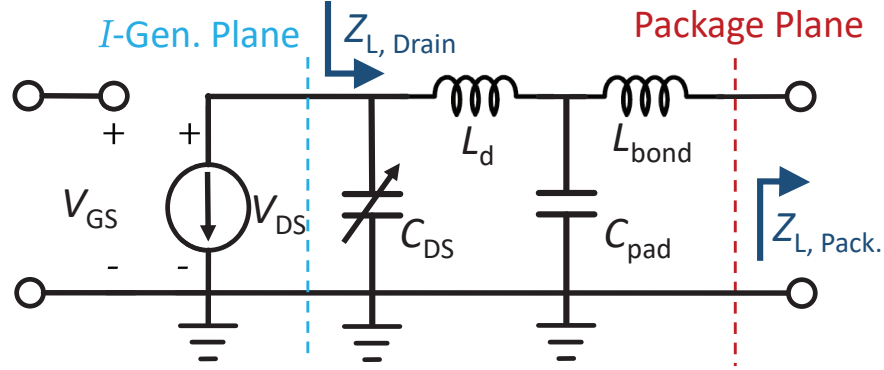


Figure 2.7: Equivalent-circuit model of CGH40010 showing the parasitics.

the interface plane of phase control is moved from the isolation port to the input of CA, as depicted in Fig. 2.4. By sweeping the input signal phase of CA, an optimal phase of  $\theta_{ca} = -10^\circ$  is obtained that leads to maximized overall LMBA efficiency along the entire OBO range, as indicated by the green curve in Fig. 2.6. The efficiency performance PD-LMBA design with realistic CA well matches the maximum efficiency achieved with ideal CSP. To fully verify the theory, the transistor parasitic network of BA is modeled (Fig. 2.7) and de-embedded to access the intrinsic drain load modulation trajectory at the current generator plane, as shown in the inset Smith chart of Fig. 2.8. The intrinsic BA loadline tracks the resistive path from  $P_{Max}$  to 10-dB OBO, which well validates the theory. As the power level further decreases below 10-dB back-off, the BAs turns off and  $Z_{BA}$  approaches to high impedance region at the edge of Smith chart (see Fig. 2.8), while the power is primarily generated by CA only at this range.

## 2.4 Wideband RF-Input PD-LMBA Design

Based on the PD-LMBA theory and practical design presented in Secs. 4 and 4, it is interesting to note that the operations of BA and CA in the PD-LMBA are nearly independent, because the CA's

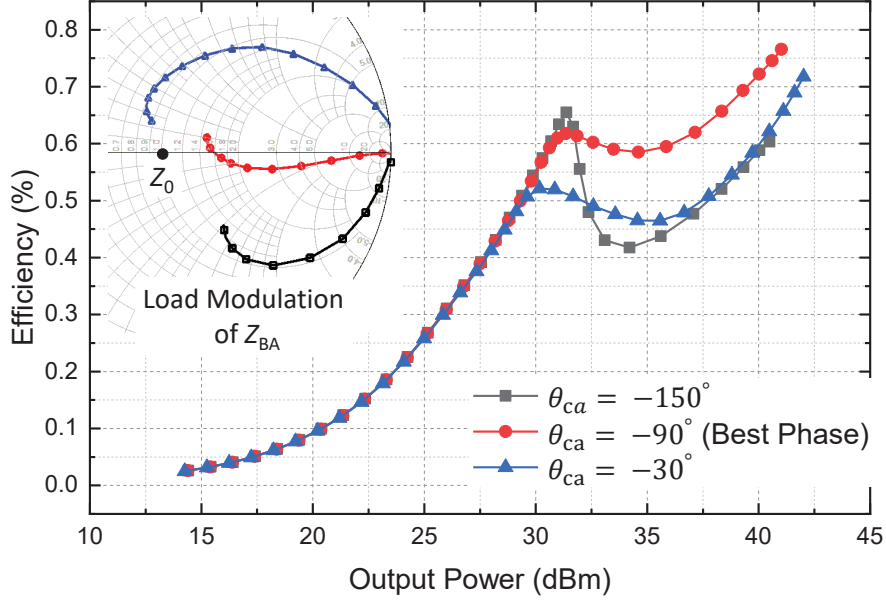


Figure 2.8: Simulated efficiency profile at 2.3 GHz under different  $\theta_{ca}$  setting.

load impedance constantly remains  $Z_0$  and the BA's load modulation is mainly due to the variation of its own current ( $I_{c,Max}/I_b$  term in Eq. (2.4)). Given the fact that the individual BA and CA can both be expanded to wideband designs, the PD-LMBA exhibits promising wideband potential. Thus, the primary challenge for wideband PD-LMBA design shifts to the wideband phase control of CA to result in optimal load-modulation behavior of BA. Following the preliminary circuit schematic shown in Fig. 2.4, the wideband RF-input PD-LMBA design is performed by broadening the bandwidth of all the building blocks and by unifying the inputs of BA and CA to a single input with proper phase offset. In the prototype demonstration, the target bandwidth is from 1.5 – 2.7 GHz covering a majority of cellular communications bands.

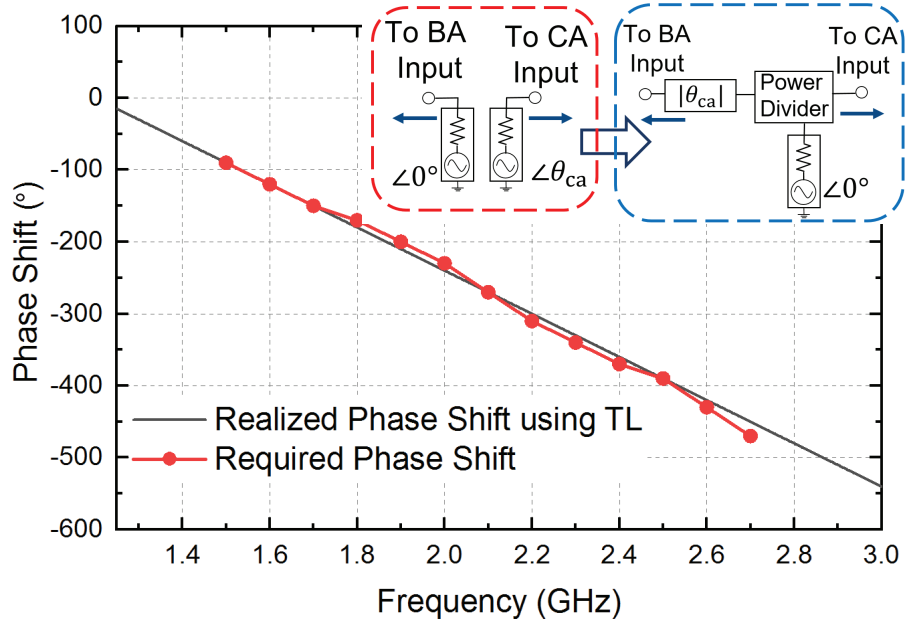


Figure 2.9: Simulated optimal BA-CA phase offset at different frequencies and design of TL-based wideband phase shifter for merging the BA and CA inputs.

#### 2.4.1 Wideband BA Design

The balanced amplifier comprises two identical PAs coupled in  $90^\circ$  out-of-phase through input and output quadrature couplers. The input coupler is built using a commercial device [43] with a wide operational bandwidth from 1-3 GHz. The output coupler is implemented using three-section branch-line hybrid structure, which offers sufficient bandwidth covering the design target [44] and is co-designed with the PAs. The two balanced PAs are implemented with 10-W GaN transistors supplied by Wolfspeed [45] (CGH40010F).

The PA output matching is performed using the non-50- $\Omega$  output coupler together with the bias line. From the load-pull simulation, the optimal load admittance ( $Y_L = G_L + jB_L$ ) of the GaN transistor presents a nearly constant real part over the target frequency range, while the imaginary part increases (becoming less inductive) with frequency. Such a frequency response of optimal

loadline is mainly due to the parasitics of the packaged GaN transistor, which has been observed in many wideband GaN PA designs [46, 47, 48]. Therefore, the characteristic impedance of the branch-line hybrid coupler,  $Z_1$ , is properly selected to provide the constant conductance ( $G_L = 1/Z_1$ ) over the target bandwidth, and the bias line as a shunt inductor is utilized to provide the susceptance with desired frequency response ( $jB_L = -j/(\omega L)$ ). It is also noted that the BA's impedance in PD-LMBA at  $P_{BA,SAT}$  is different from the ideal BA with the contribution of CA, as indicated by Eq. (2.10). Therefore, the finalized value of  $Z_1 (= 30 \Omega)$  and the bias-line length are determined through co-simulation with CA. A wideband 3 : 5 transformer follows branch-line hybrid coupler to match the impedance to the 50- $\Omega$  terminal.

The input matching is designed and implemented using a multistage low-pass network based on transmission lines (TL) to cover the target bandwidth from 1.5 to 2.7 GHz. The design of such a matching circuit follows the well-established methodology presented in [46]. This paper uses a four-section TL-based lowpass networks to realize the input matching, with each stage consisting of a series  $L$  (high-impedance TL) and shunt  $C$  (low-impedance open-ended stubs). The final lengths and widths of the TLs are tuned in order to absorb the parasitics of the RF and dc block as well as the device packaging.

#### 2.4.2 Wideband CA Design

According to the amplitude control scheme described in Secs. 4 and 4, the saturated power of CA determines the dynamic range once the BA power is fixed. To achieve the target OBO of 10 dB,  $P_{CA,SAT}$  should be around 9.5-dB below  $P_{BA,SAT}$ . To realize this low output power, the CA is implemented with a 6-W GaN transistor (Wolfspeed CGH40006P), and it is biased in Class-AB mode with partial  $V_{DD}$ . As the CA's maximum efficiency at  $P_{CA,SAT}$  determines the overall LMBA efficiency at the target OBO point, the design of CA as a single PA is aimed at achieving

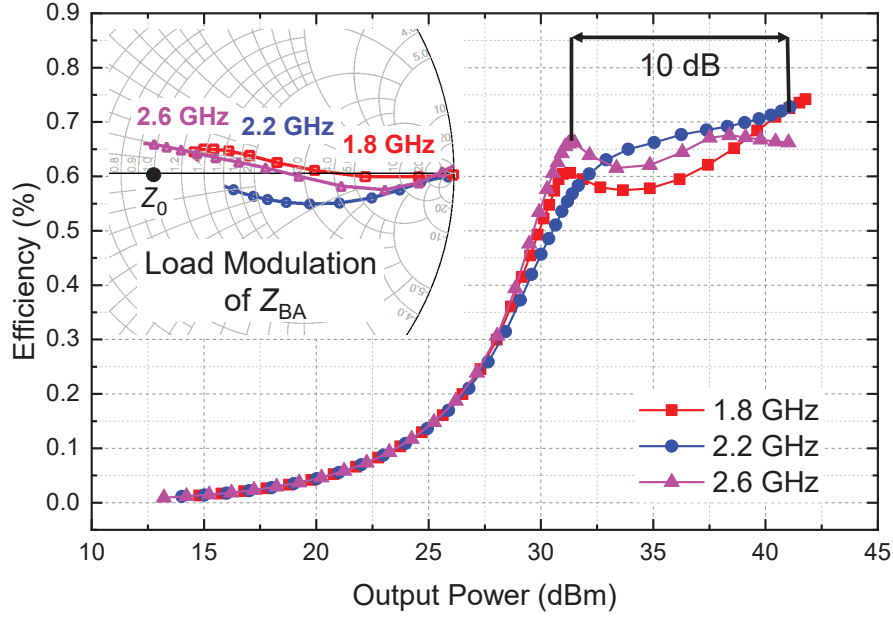


Figure 2.10: Power-swept CW simulation results of the PD-LMBA for best phase tuning setting at different frequencies.

the highest possible efficiency. The output matching network design is performed to offer optimal loading impedance at both fundamental frequency and harmonics over the target bandwidth. Since the CA is directly connected to the non-50- $\Omega$  coupler, the design of output matching is based on the coupler characteristic impedance,  $Z_1$ .

For the input matching network design, we follow the same methodology in BA's input design, and a three-section lowpass network based on transmission lines is designed to provide wideband input matching for the GaN transistor.

#### 2.4.3 Wideband BA-CA Phase Offset Design

Upon the completion of wideband BA and CA designs, the load modulation of BA is primarily governed by the relative phase between BA and CA. At a particular frequency, there is an optimal

BA-CA phase offset that leads to the maximized back-off efficiency, as depicted in Fig. 2.8. Using the dual-input (with equal amplitude) schematic in Fig. 2.4, the optimal phase offset is determined for each frequency point along the target bandwidth (0.1-GHz step), which is presented as the red dots in Fig. 2.9. It is noted that the optimal phase offset is almost linearly proportional to frequency with a negative slope. This frequency behavior can be easily implemented using a  $50\text{-}\Omega$  transmission line in connection with an in-phase input source, thus realizing a wideband phase shifter and offering accurate wideband phase control. Given the negative value of relative phase between CA and BA, this offset transmission line in CA path has a negative length, which can be physically implemented by placing a symmetrical TL with positive length in the BA path. With such a TL phase shifter, the dual inputs can be simply replaced by a single input with a standard wideband Wilkinson divider.

In the reported RF-input wideband LMBA designs [29], *LC*-based bandpass filter has been utilized to implement the BA-CA phase shifter for wideband phase control. However, the frequency response of the phase is very sensitive to the value of *LC* components. Given the unavoidable manufacturing variation in reality, it is difficult to accurately control all the component values in actual experiments, thus leading to a discrepancy between simulation and measurement. This sensitivity could also cause yield issue for massive production. The transmission-line-based phase shifter well solves this problem and leads to minimized complexity for implementation.

The input power of the CA will continue to increase after reaching saturation at 10-dB OBO due to the RF-input, resulting in over-driving of the CA. It should be noted that the proposed architecture is mainly to maximize efficiency. The linearity is concerned as CA is over driven, and the over driving of main amplifier has been utilized in another load modulation architecture, i.e., DEPA, as presented in [20]. However, it has been demonstrated in [20] that such a behavior does not affect digital linearization performance.



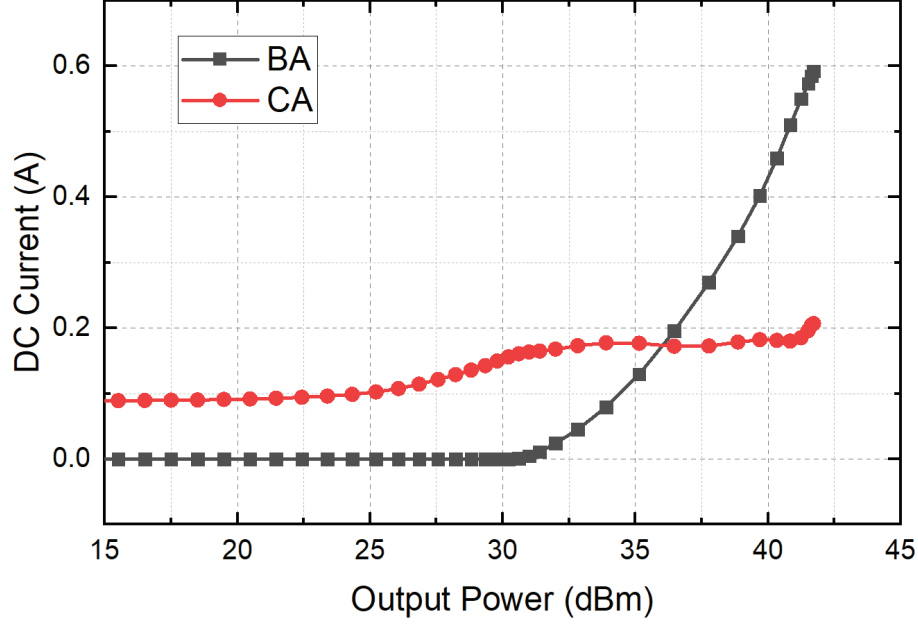
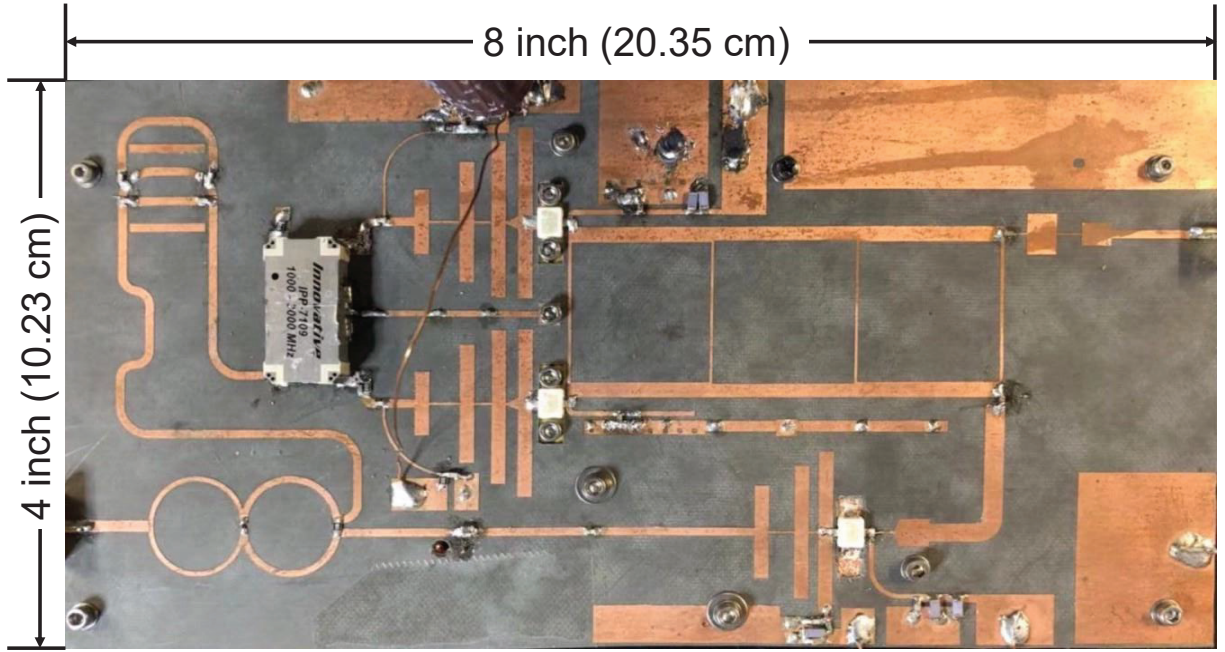


Figure 2.11: Simulated drain DC current versus output power of BA (two BAs in total) and CA at 2.3 GHz.

#### 2.4.4 Overall Schematic and Simulation Results

Through proper amplitude and phase control described in the above two sections, the extended power back-off range and the optimal load-modulation trajectory can be achieved at different frequencies, as shown in Fig. 2.10. When the power falls below the target OBO, the output impedance of the BA transistor ( $Z_{BA}$ ) is close to the high impedance region on the Smith chart edge. This means that the BA starts to turn off, while the power is purely generated by the CA. This Doherty-like behavior is achieved by properly setting the gate bias voltages of BA and CA below and above the transistor threshold, respectively. The DC current of BA and CA are extracted from the CW simulation to verify this PD-LMBA operation, as shown in Fig. 2.11. The turn-on point of BA is around 10 dB power back-off, where the CA approaches its saturation. As the power increases beyond 10-dB OBO, a strong peaking effect of BA current is observed in parallel with a almost





20-mil Thick Rogers Duroid-5880;  $\epsilon_r$ :2.2

Figure 2.13: Fabricated pseudo-Doherty LMBA prototype.

for reducing the circuit footprint size), all the other individual building blocks, e.g., BA, CA, and output coupler, are not over designed in terms of bandwidth. The phase offset line is added after optimizing the overall PD-LMBA using the dual-input model shown in Fig. 2.4. In practical PD-LMBA development, it should be optimized within the target bandwidth, and, ideally, the individual building blocks shall not be over-designed.

## 2.5 Implementation and Experimental Results

The designed broadband PD-LMBA prototype is fabricated on a 20-mil thick Rogers Duroid-5880 PCB board with a dielectric constant of 2.2, and is mounted on a copper substrate for handling and measurement, as shown in Fig. 2.13. The PCB footprint size is 4 inch  $\times$  8 inch. The prototype is

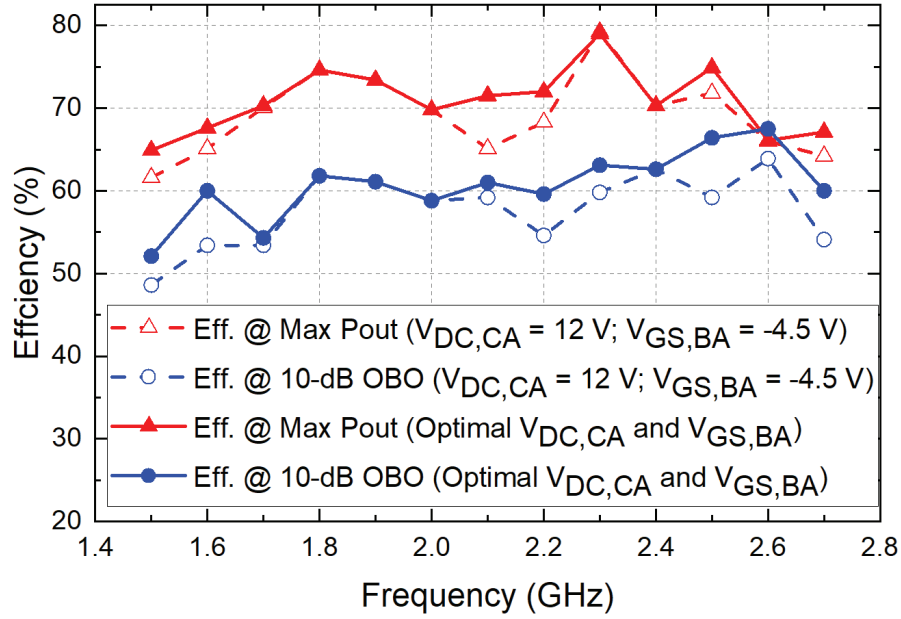


Figure 2.14: Simulated power efficiency comparison between consistent  $V_{GS,BA}$ ,  $V_{DS,CA}$ , and optimal  $V_{GS,BA}$  (-5 to -4 V),  $V_{DS,CA}$  (10 to 14 V) at  $P_{max}$  and 10-dB OBO levels from 1.5 to 2.7 GHz.

experimentally evaluated with both continuous-wave (CW) and modulated stimulation signals. In the measurement, the BA is biased in Class-C with 28 V of  $V_{DS,BA}$ . The gate bias voltage  $V_{GS,BA}$  is set between -5 V and -4 V to obtain the best power-added efficiency (PAE) in the test, which varies with different frequencies. The CA is biased in Class-AB with  $V_{GS,CA}$  around -2.8 V and  $V_{DS,CA}$  around 12 V (tuning range from 10 to 14 V ensuring CA saturation at 10-dB OBO). Due to the reduced CA bias voltage and the high breakdown voltage of GaN transistor, the over driving of CA does not affect the circuit reliability. In experiment, the developed PD-LMBA can be well sustainable over prolonged high-power operation. In addition, if the PD-LMBA can be implemented on chip, the over-driving effect can be mitigated through analog control.

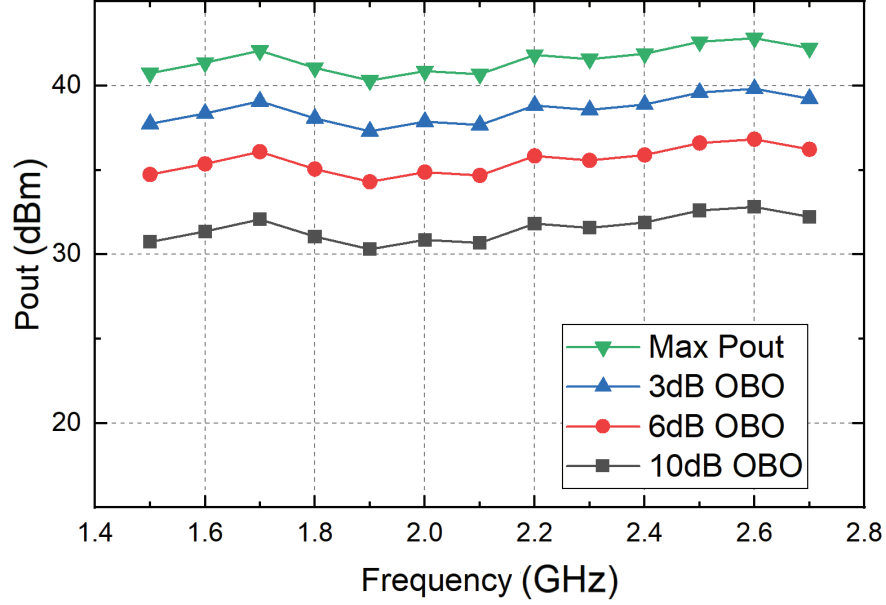


Figure 2.15: Measured output power at various OBO levels from 1.5 to 2.7 GHz.

Table 2.1: State-of-the-Art of Wideband Load-Modulated Power Amplifiers

Ref. / Year	Architecture	Freq. (GHz)	FBW (%)	$P_{\text{Max}}$ (dBm)	DE @ $P_{\text{Max}}$ (%)	DE @ HBO (%)	DE @ LBO (%)
[49] 2018	3-Way DPA	0.6-0.9	40	46.1-46.9	51.1-78	51.9-66.2@6 dB	42-64@9.5 dB*
[21] 2018	3-Way DPA	2.0-2.6	26	43.6-45.4	53-76	45-55@6 dB	41-48@8 dB
[22] 2019	3-Way DPA	1.6-2.6	48	45.5-46	53-66	52-66@6 dB	50-53@9.5 dB
[40] 2016	DPA	1.6-2.2	31.6	46-47	60-71	50-55@6 dB*	51-55@10 dB
[50] 2018	DPA	1.5-3.8	86.8	42.3-43.4	42-63	33-55@6 dB	22-40@10 dB*
[20] 2019	DEPA	2.55-3.8	40	48.8-49.8	54-67	42-53@6 dB*	47-60@8 dB
[41] 2017	Dual-Input LMBA	4.5-7.5	50	39	47-77*	28-60@6 dB*	40-72@10 dB* <sup>‡</sup>
[42] 2018	Dual-Input LMBA	1.7-2.5	38	48-48.9	48-58*	43-53@6 dB*	33-45@10 dB* <sup>†</sup>
[24] 2017	RF-Input LMBA	0.7-0.85	19	42	57-70	34-48@6 dB	30-35@10 dB* <sup>†</sup>
[29] 2017	RF-Input LMBA	1.8-3.8	71	44	46-70	33-59@6 dB	20-25@10 dB* <sup>†</sup>
This Work	PD-LMBA	1.5-2.7	57	43	58-72	47-61@6 dB	47-58@10 dB

\* Graphically estimated, <sup>†</sup> PAE, <sup>‡</sup> with reduced  $V_{\text{DD}}$ .

### 2.5.1 Continuous-Wave Measurement

The prototype is measured under the excitation of a single-tone CW signal from 1.5 to 2.7 GHz at different OBO levels. Fig. 2.15 shows the maximum output power constantly above 41 dBm over

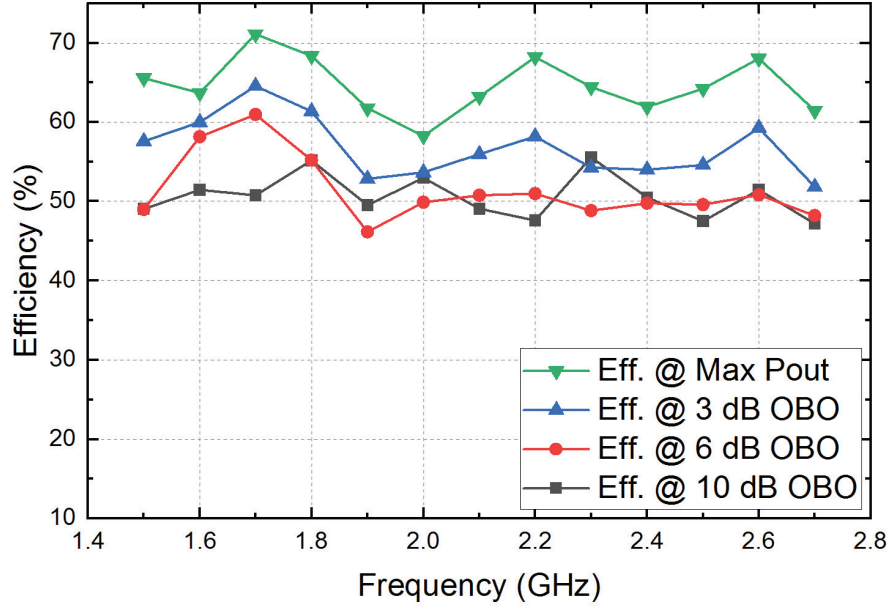


Figure 2.16: Measured power efficiency at various OBO levels from 1.5 to 2.7 GHz.

the entire bandwidth. In Fig. 2.16, the efficiency at maximum power has a local maxim of 72% at 1.7 GHz, and it remains higher than 58% throughout entire frequency range. The efficiencies at 6-dB OBO and 10-dB OBO are in the range of 48 – 61% and 47 – 58%, respectively. The efficiencies here are defined as the ratio between the output power and the total DC power applied to all three amplifiers (i.e., BA1, BA2 and CA), as shown below

$$\text{Efficiency} = \frac{P_{\text{out}}}{P_{\text{DC,BA1}} + P_{\text{DC,BA2}} + P_{\text{DC,CA}}}. \quad (2.10)$$

It can be seen from Fig. 2.17 that the gain is maintained around 8 dB. It should be noted that the primary purpose of this paper is to demonstrate the proposed concept, and the presented prototype is a first-pass design. Realistically, the gain degradation at band edge and gain fluctuation over frequency can be mitigated with more design iterations. Moreover, the PD-LMBA prototype is measured with a power-swept stimulus, and the measured efficiency and gain profiles are plotted

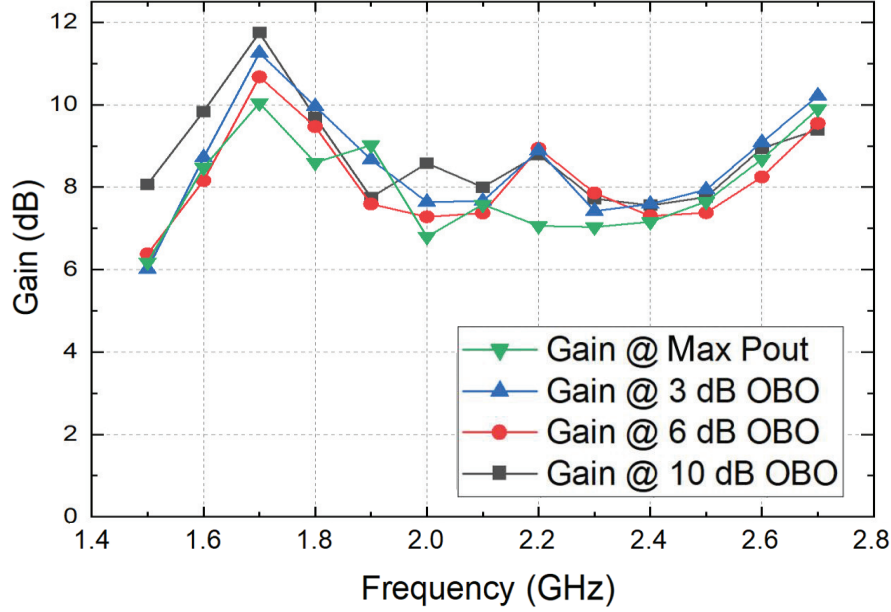


Figure 2.17: Measured gain at various OBO levels from 1.5 to 2.7 GHz.

in Fig. 2.18. The shape of the efficiency versus output power curve in Fig. 2.18 shows a distinct Doherty-like behavior of the PA, which is demonstrated over 10-dB power back-off range at almost every single sample frequency point from 1.5 – 2.7 GHz. These measurement results well validate the proposed PD-LMBA concept and demonstrate the advantage of this new technology in PA efficiency enhancement over wide bandwidth. The results also indicate that the PD-LMBA is relieved from the original LMBA's [23] reliance on dynamic phase adjustment at a single frequency.

Table I presents a comparison between this design and other recently published active-load-modulation PAs with similar frequency range, output power level and technology. Even though there is certain discrepancy between the measurement (Fig. 2.18) and simulation (Fig. 2.10), where the measured efficiency drops in the upper power regime at some frequencies, the measured efficiencies (at both  $P_{\text{Max}}$  and various back-off levels) over a broad bandwidth still compare favorably to the state-of-the-art.

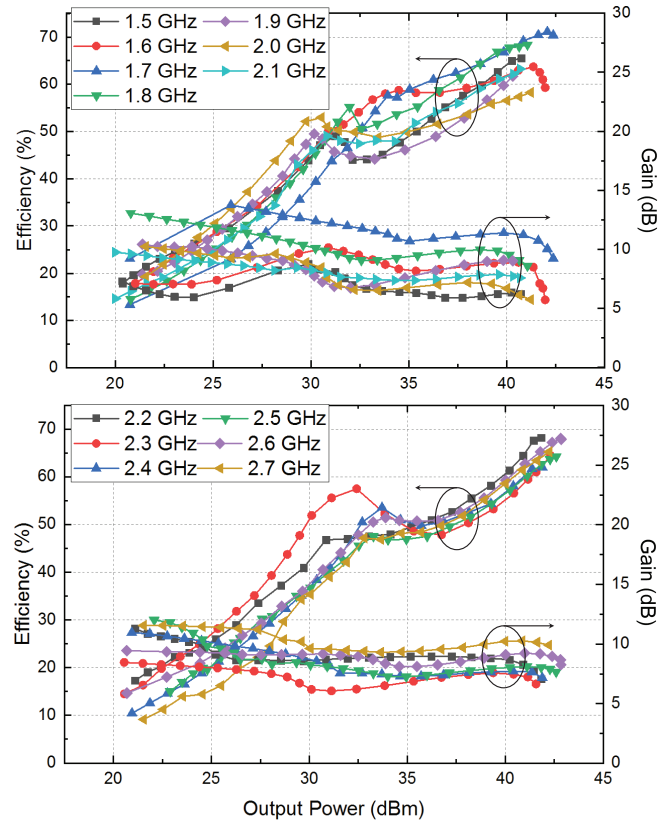


Figure 2.18: Power-swept measurement of efficiency and gain from 1.5 to 2.7 GHz.

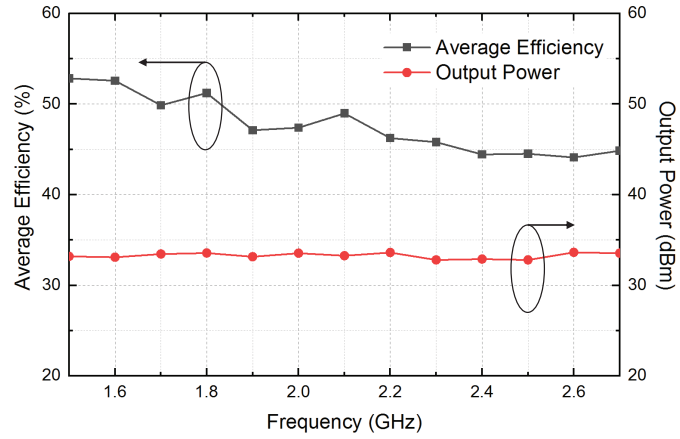


Figure 2.19: Measured output power and average efficiency with 9.5-dB-PAPR LTE signal from 1.5 to 2.7 GHz.



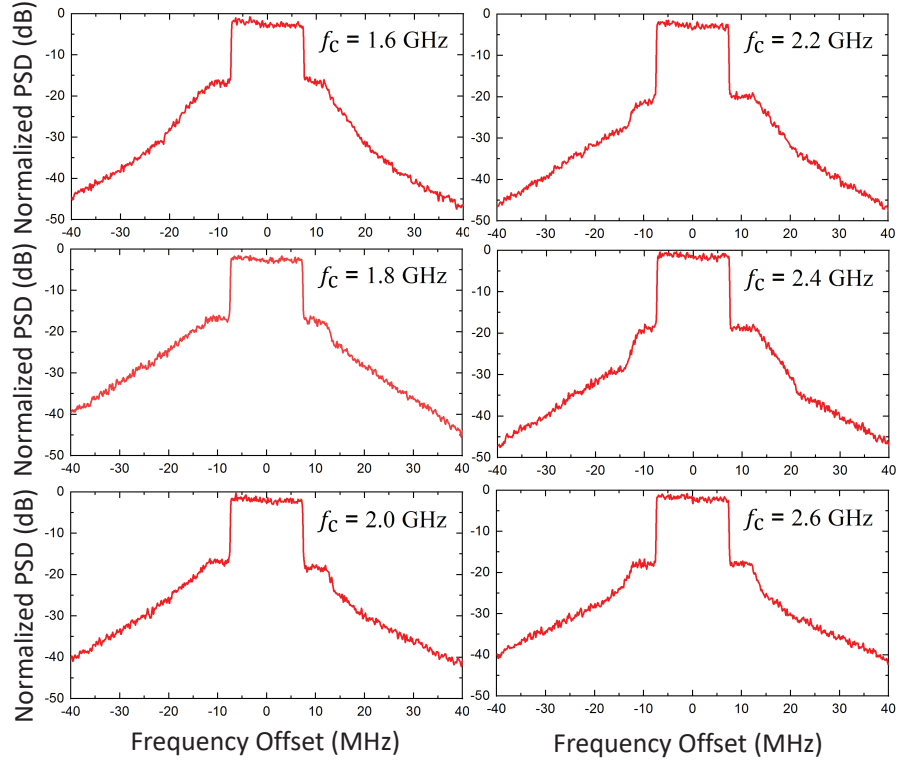


Figure 2.20: Output spectrum from modulated measurement using a 10-MHz 9.5-dB-PAPR LTE signal centered at 1.6, 1.8, 2.0, 2.2, 2.4 and 2.6 GHz.

### 2.5.2 Modulated Measurement

To validate the operation of the designed PD-LMBA in realistic communications, a 10-MHz LTE signal with a PAPR of 9.5 dB was employed as the stimulation. The modulated-signal is generated and analyzed by a Keysight PXIe vector transceiver (VXT M9421). The generated LTE signal is further boosted by a pre-amplifier (ZHL-5W-422+) to a sufficient level for driving the PD-LMBA. The measurement results at an average output power around 33.5 dBm are presented in Fig. 2.19. The PD-LMBA achieves a high average efficiency of 47 – 58% over the target frequency band. The measured output power spectral density (PSD) are shown in Fig. 2.20. The best-case ACLR of 25.8 dB is measured without any digital predistortion.

## 2.6 Conclusion

This paper introduces a new type of LMBA with pseudo-Doherty load-modulation behavior. Based on a special combination of control amplifier (carrier) and balanced amplifier (peaking), this PD-LMBA architecture, for the first time, results in decoupled co-operation of carrier and peaking amplifiers, thus fundamentally eliminating the bandwidth limitation imposed on classic active load modulation techniques. With proper phase and amplitude controls, an optimal load-modulation behavior can be achieved for PD-LMBA leading to maximized efficiency over extended power back-off range. More importantly, the efficiency optimization can be achieved with only a static setting of phase offset at a given frequency, which greatly simplifies the complexity for phase control. The measurement results using continuous wave and modulated stimulus signals perfectly validate the proposed PD-LMBA theory and experimentally presents a breakthrough on the broadband load-modulated PA in terms of efficiency, back-off range, and bandwidth. Thus, the proposed design method can be considered as a new design paradigm for active load modulation.

## **CHAPTER 3: ASYMMETRICAL LOAD MODULATED BALANCED AMPLIFIER**

This chapter is based in part on the previously published article listed below. I have permission from my co-authors and publishers to use the work listed below in my dissertation. [“Asymmetrical load modulated balanced amplifier with continuum of modulation ratio and dual-octave bandwidth,” IEEE Trans. Microw. Theory Techn., vol. 69, no. 1, pp. 682–696, Jan. 2021.].

### **3.1 Introduction**

The formation of the fifth generation (5G) wireless communication ecosystem have resulted in ever-growing demands for higher data rates. Due to the scarcity of spectrum resources, low-latency and high-capacity wireless connectivity requires vast enhancement of spectral efficiency realized using advanced modulation schemes, such as 1024 Quadrature Amplitude Modulation (QAM) and orthogonal frequency division multiplexing (OFDM). However, those complexly modulated radio waves have a high PAPR, leading to substantially reduced efficiency of traditional power amplifiers (PAs). On the other hand, the proliferation of communication bands has been largely expanding the wireless spectrum towards higher frequencies. This ever-increasing number of allocated frequency bands is strongly calling for bandwidth extension technologies of PAs. In the current and next-generation radio systems, the operational bandwidth of a single PA is desired to be as wide as possible, in order to minimize the number of PAs on a wireless platform for reducing the cost, space, and system complexity. These emerging requirements have brought up unprecedented challenges for the realization of PAs.

In order to improve the PA efficiency for amplification of high-PAPR signals, there are currently

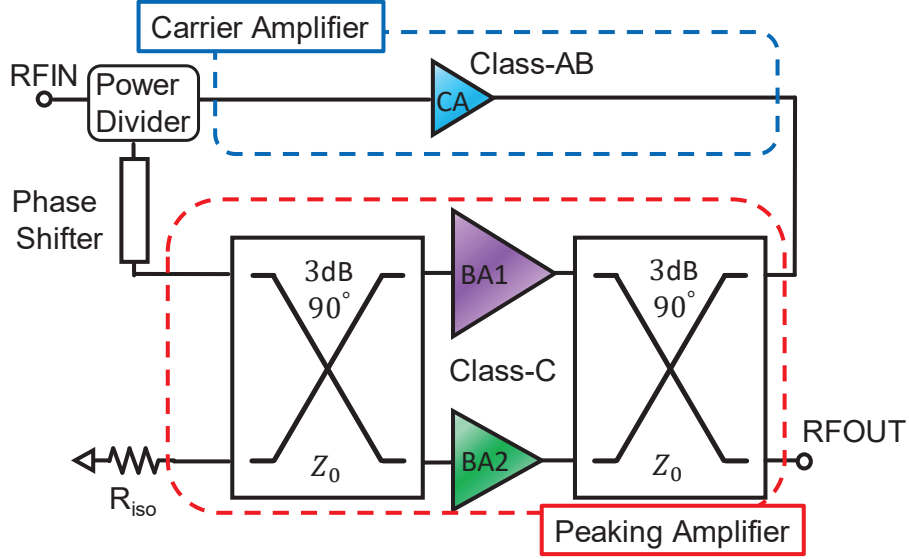


Figure 3.1: Overview of pseudo-Doherty asymmetrical LMBA.

two main technical solutions, envelope tracking (ET) and load modulation. Due to the fact that ET suffers from the complexity of system implementation, limited dynamic range, and undesirable modulation-bandwidth up-scalability [3, 51], load modulation technique exhibits promising potential for accommodating the fast-evolving communication standards, e.g. 5G and Wi-Fi 6. Until now, a variety of load modulation architectures have been proposed, developed, and implemented in practical systems, including DPA [4, 5, 6], out-phasing PA [7, 8, 9, 10], and varactor-based dynamic load modulation [11, 12, 13, 14, 15]. Among various load modulation techniques, DPA has already been widely deployed in cellular base stations as a representative implementation of load modulation [52, 53]. However, towards the applications in the emerging wireless systems, DPA faces two major challenges as follows. First, the limited output power back-off (OBO) range is not sufficient to support the large PAPR of the latest modulation schemes ( $> 10$  dB); Second, the RF bandwidth is strongly limited by the quarter-wave inverter embedded in the DPA circuitry. Despite recent advances in broadband DPAs [20, 49, 40, 54], maintaining consistently optimal load-modulation behavior and efficient DPA performance over a wide RF bandwidth still remains

a major challenge.

The recently reported load modulated balanced amplifier (LMBA) [23, 24, 25, 26, 27, 28] has been demonstrated as an effective method to perform load modulation over a wide RF bandwidth. The load impedance of the BA device can be controlled by the amplitude and phase variations of a control signal injected into the isolated port of the output quadrature coupler, leading to enhanced back-off efficiency. By implementing an external CA to drive the isolation port, an RF-input LMBA can be constructed [24, 29]. The authors of this paper has further developed the generic LMBA theory in a new topology [31, 55], which is named PD-LMBA. It reveals that the Doherty-like biasing of BA (peaking) and CA (carrier) combined with proper amplitude and phase controls can result in optimal BA load modulation behavior over extended OBO range. Moreover, such an operation can be seamlessly extended over a unlimited frequency span as long as proper BA-CA phase offset is maintained. This type of Doherty-like biasing of LMBA has also been reported as sequential LMBA (SLMBA) in [56]. However, there are also some unresolved issues with PD-LMBA. Primarily, the CA reaches saturation at the predetermined OBO level where the BA starts to turn on, but the CA impedance remains constant as the input power continues to increase. This indicates that the CA is constantly subject to over-driving during the BA load modulation, which could cause strong non-linearity and reliability issues of CA.

Expanding the horizon of LMBA, this paper presents a new theory of asymmetrical load-modulated balanced amplifier (ALMBA). It is discovered that, by setting asymmetric current/power scaling of BA1 and BA2, a continuum of CA load-modulation ratio can be achieved, i.e., between carrier LM of DPA and no LM of CA in generic LMBA. Meanwhile, the load modulation behaviors of BA1 and BA2 in PD-ALMBA can be controlled independently. As a result, in pseudo-Doherty operation of ALMBA as shown in Fig. 3.1, the current and power of CA can further increase after reaching the first efficiency peak at the target OBO level, which strongly mitigates the CA over-driving as in PD-LMBA [31, 55, 56], leading to the enhanced linearity and reliability of the entire

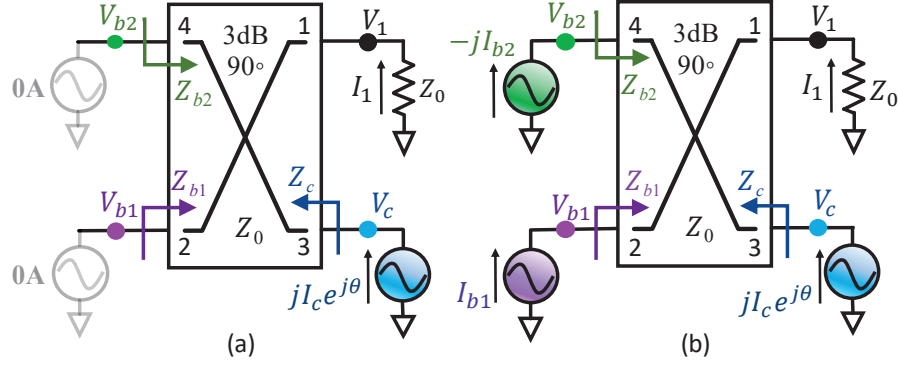


Figure 3.2: Ideal generalized schematic of the output combining network for analyzing the proposed PD-ALMBA architecture: (a)  $P_{\text{OUT}} < P_{\text{max}}/\text{OBO}$ , (b)  $P_{\text{OUT}} \geq P_{\text{max}}/\text{OBO}$ .

amplifier. It is critical to note that the established LMBA theory inclusively explains the generic symmetrical LMBA mode, which can be considered as a special case of this generalized theoretical framework for quadrature-coupler-based active LM architectures. The analytical derivation of the proposed theory is well verified by simulation and is experimentally validated with a developed PD-ALMBA prototype. With inherited wideband nature of PD-LMBA demonstrated in [55] and leveraging ultra-wideband commercial quadrature couplers, and the advanced PD-ALMBA mode is physically realized over nearly unlimited bandwidth (two octaves in this design) with meanwhile  $\geq 10$ -dB power back-off range. The theory and practical results presented in this paper underline that the PD-ALMBA promises an ideal solution for developing next-generation ultra-wideband and high-efficiency load-modulation PAs.

### 3.2 Asymmetrical LMBA Theory

Developed from the recently reported LMBA theory [23], a new architecture of asymmetrical LMBA is proposed in this section, and a generalized ALMBA theory framework is established.

### 3.2.1 Generalized Asymmetrical LMBA Mode

As shown in Fig. 3.1, the LMBA architecture [23] involves a BA and a CA combined with a predetermined phase offset. The behavior of LMBA can be modeled as three excitation sources driving the output quadrature coupler, and it is analytically described using impedance matrix given by

$$\begin{bmatrix} V_1 \\ V_2 \\ V_3 \\ V_4 \end{bmatrix} = Z_0 \begin{bmatrix} 0 & 0 & +j & -j\sqrt{2} \\ 0 & 0 & -j\sqrt{2} & +j \\ +j & -j\sqrt{2} & 0 & 0 \\ -j\sqrt{2} & +j & 0 & 0 \end{bmatrix} \begin{bmatrix} I_1 \\ I_2 \\ I_3 \\ I_4 \end{bmatrix} \quad (3.1)$$

where  $V_1 = -I_1 Z_0$ ,  $I_2 = I_{b1}$  and  $I_4 = -jI_{b2}$  representing the input RF currents from BA1 and BA2, while  $I_3 = jI_c e^{j\theta}$  denotes the CA current that is phase-shifted from BA1 by  $\pi/2 + \theta$  [23], as shown in Fig. 3.2. Using the matrix operation illustrated in (4.1), the impedances of BA1 and BA2 can be calculated as

$$\begin{aligned} Z_{b1} &= Z_0 \left( \frac{I_{b2}}{I_{b1}} + \frac{\sqrt{2}I_c e^{j\theta}}{I_{b1}} \right); \\ Z_{b2} &= Z_0 \left( 2 - \frac{I_{b1}}{I_{b2}} + \frac{\sqrt{2}I_c e^{j\theta}}{I_{b2}} \right). \end{aligned} \quad (3.2)$$

The load impedance seen by the CA can also be calculated from (4.1), given by

$$Z_c = Z_0 \left( 1 - \sqrt{2} \frac{I_{b1} - I_{b2}}{I_c e^{j\theta}} \right). \quad (3.3)$$

An interesting fact is observed that the ALMBA described in Eqs. (3.2) and (4.4) can be fully converged to the generic LMBA by setting  $I_{b1} = I_{b2}$ , in which BA1 and BA2 are loaded with the same impedance ( $Z_{b1} = Z_{b2}$ ). Meanwhile, the CA in symmetrical LMBA is not load modulated regardless of the changes of currents. However, if BA1 and BA2 are not identical, the LM of CA

can be achieved, while BA1 and BA2 are subject to different LM behaviors. By properly setting the phase and amplitude of all three amplifiers, their LM behaviors can be manipulated independently. This first-ever discovery leads to a generalization of the quadrature-coupler-based LM PA theory, and it fundamentally expands the design space of original LMBA.

### *3.2.2 Pseudo-Doherty Biasing and Current-Generator Modeling*

By applying Doherty-like biasing of CA and BA, a PD-LMBA is constructed with CA as the carrier amplifier and BA as the peaking amplifier. As depicted in Fig. 3.2, the essence of PD-LMBA operation is based on the following conditions:

- The BA1 and BA2 are turned off at low power region where only the CA operates, as shown in Fig. 3.2(a);
- When the CA reaches saturation ( $I_c = I_{c,\max}$ ), the BA turns on at the same time, illustrated in Fig. 3.2(b).

Comparing with other load modulation technologies, the PD-LMBA architecture has three main advantages: 1) The power scaling between carrier and peaking amplifiers can be easily realized for achieving extended power back-off range, since the BA with two PAs combined is naturally stronger in power generation than the single-branch of CA; 2) The optimal load modulation behavior of BA (purely resistive) can be achieved only with a static phase setting of CA which minimizes the complexity of phase control; 3) Under ideal phase and amplitude control, two efficiency peaks can be achieved at maximum power ( $P_{\text{MAX}}$ ) and predefined OBO with minimal efficiency degradation in between. However, the CA in PD-LMBA reaches full saturation at the target OBO level, and, thus, it is under constant over-driving from OBO to  $P_{\text{MAX}}$ , resulting in linearity degradation and potential reliability issues of the entire PD-LMBA.



In order to alleviate the CA over-driving issue, a feasible solution is to enable load modulation on CA, which is similar to the carrier amplifier in distributed efficient power amplifier (DEPA) [57, 19]. To better analyze the load-modulation characteristics of PD-ALMBA, the currents of BA1, BA2, and CA are carefully modeled [56]. As the carrier amplifier, the CA current, i.e.,  $i_{ca}$ , is defined by

$$i_{ca}(\beta) = \begin{cases} i_{ca,bo}(\beta), & 0 \leq \beta < \beta_{bo} \\ i_{ca,h}(\beta), & \beta_{bo} \leq \beta \leq 1 \end{cases} \quad (3.4)$$

where  $i_{ca,bo}$  is the CA current at power back-off where the BA1 and BA2 are turned off, and  $i_{ca,h}$  denotes the CA current in high-power region where the BA1 and BA2 are turned on.  $\beta$  is the normalized variable to describe the magnitude of the input driving level, and  $\beta_{bo}$  is the threshold between the low-power and high-power regions.  $i_{ca,bo}$  can be simply expressed as the defined current of the ideal Class-B mode:

$$i_{ca,bo}(\beta) = \begin{cases} \frac{\beta}{\beta_{bo}} \frac{I_{Max,C}}{\alpha} \cdot \cos\theta, & -\frac{\pi}{2} \leq \theta < \frac{\pi}{2} \\ 0, & \text{otherwise} \end{cases} \quad (3.5)$$

where  $I_{Max,C}$  represents the maximum current allowed to flow through the CA transistor, and  $\alpha$  stands for the ratio between the maximum CA currents of low-power region and high-power region. It is interesting to note that  $\alpha$  can also be considered as the load modulation ratio of CA. From (3.5), the DC and fundamental components of  $i_{ca,bo}$  can be obtained as

$$\begin{aligned} i_{ca,bo}[0] &= \frac{2\beta}{\pi\alpha \cdot \beta_{bo}} I_{Max,C}; \\ i_{ca,bo}[1] &= \frac{\beta}{2\alpha \cdot \beta_{bo}} I_{Max,C}. \end{aligned} \quad (3.6)$$

When the driving power increases to  $\beta_{bo}$ , the CA is saturated corresponding to the first efficiency peak at the target OBO level. For symmetrical PD-LMBA ( $\alpha = 1$ ) [31, 55],  $i_{ca,bo}$  grows to its maximum value, and this maximum CA current is maintained as the driving power continuing to increase towards the maximum input driving level ( $\beta = 1$ ). For PD-ALMBA ( $\alpha > 1$ ), the CA is only voltage saturated at  $\beta_{bo}$ , which still leads to an efficiency peak, and the CA current is increased by a factor of  $\alpha$  to the full saturation (both voltage and current) at  $\beta = 1$ . Therefore,  $i_{ca,h}$  of PD-ALMBA can be expressed as

$$i_{ca,h}(\beta) = \begin{cases} I_{Max,C} \cdot \cos \theta, & -\frac{\pi}{2} \leq \theta < \frac{\pi}{2} \\ 0, & \text{otherwise} \end{cases} \quad (3.7)$$

The fundamental component of CA current ( $I_{ca}$ ) is plotted as the blue curve in Fig. 3.3. With a variation of LM factor, i.e.,  $\alpha \in (1, 2)$ , the CA load modulation falls within a continuum between symmetrical PD-LMBA and Doherty PA.

The BAs are biased identically at Class-C mode. Assuming that  $i_{b1}$  and  $i_{b2}$  are proportional, they can be derived as

$$i_{ba1}(\beta) = \begin{cases} 0, & 0 \leq \beta < \beta_{bo} \\ i_{ba1,h}(\beta), & \beta_{bo} \leq \beta \leq 1 \end{cases} \quad (3.8)$$

$$i_{ba2}(\beta) = \sigma \cdot i_{ba1}(\beta). \quad (3.9)$$

where  $\sigma$  represents the current scaling ratio between BA1 and BA2 (e.g.,  $\sigma = 1$  for symmetrical BA). The BA1 current in high-power region can be expressed using Class-C current formula as:

$$i_{ba1,h}(\beta) = \begin{cases} \frac{\beta \cdot \cos \theta - \beta_{bo}}{1 - \beta_{bo}} I_{Max,B1}, & -\theta_b \leq \theta < \theta_b \\ 0, & \text{otherwise} \end{cases} \quad (3.10)$$

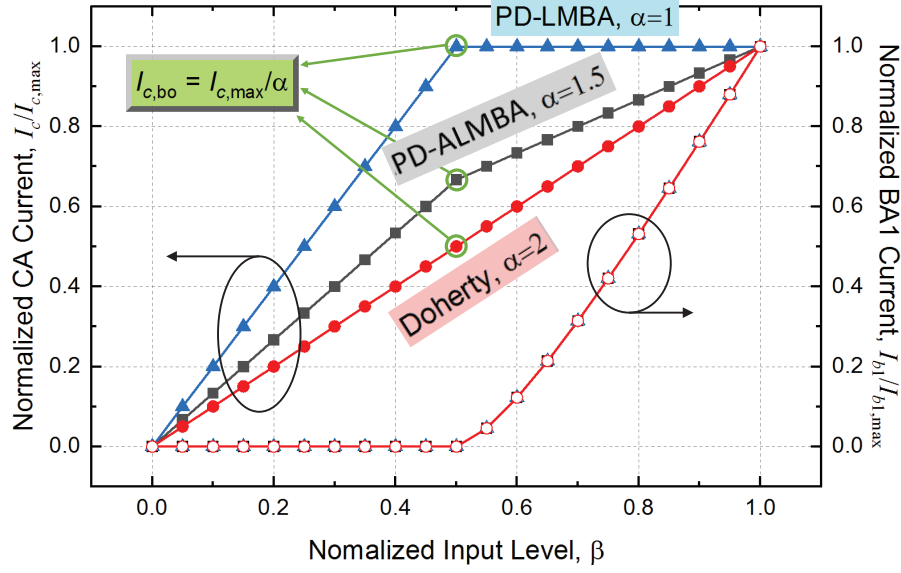


Figure 3.3: Normalized currents of  $I_c$  and  $I_{b1}$  when  $\beta_{bo} = 0.5$  for different PA modes, i.e., PD-LMBA, PD-ALMBA, and Doherty PA.

where  $(-\theta_b, +\theta_b)$  defines the turn-on phase range of BA1 and BA2. Thus,  $\theta_b$  is obtained as

$$\theta_b = \arccos(\beta_{bo}/\beta). \quad (3.11)$$

By applying Fourier Transformation, the DC and fundamental currents of BA1 can be calculated as

$$\begin{aligned} i_{ba1,h}[0] &= \frac{I_{Max,B1}}{1 - \beta_{bo}} \cdot \frac{2\beta \sin \theta_b - 2\beta_{bo} \theta_b}{\pi}, \\ i_{ba1,h}[1] &= \frac{I_{Max,B1}}{1 - \beta_{bo}} \cdot \frac{\beta(2\theta_b + \sin 2\theta_b) - 4\beta_{bo} \sin \theta_b}{2\pi}. \end{aligned} \quad (3.12)$$

The normalized current of the BA1 versus  $\beta$  is presented in Fig. 3.3. The BA current is only dependent on the driving level,  $\beta$ , regardless of CA LM factor,  $\alpha$ .

### 3.2.3 Load Modulation Analysis of PD-ALMBA

For PD-ALMBA, the CA is load modulated after the CA first reaches voltage saturation at the predefined OBO with a decreasing  $Z_c$  and an increasing  $I_c$ , thus extending the linear range of CA. Realistically, this can be achieved by enforcing asymmetry between BA's two sub-amplifiers, i.e., difference of current between BA1 and BA2, as indicated by (4.4). To theoretically analyze the PD-ALMBA, its operation is divided into the following three regions:

- **Low-Power Region** ( $P_{OUT} < P_{MAX}/OBO$ ): When operating at low power level below the predefined target OBO power, the BA1 and BA2 are completely turned off, as depicted in Fig. 3.2(a). The CA operates as a standalone Class-AB amplifier, and the output power is solely generated by CA. In this back-off region, the load modulation behaviors of BA1 and BA2 as well as the CA impedance are provided as follows

$$\begin{aligned} Z_{b1,LP} &= Z_{b2,LP} = \infty; \\ Z_{c,LP} &= Z_0. \end{aligned} \tag{3.13}$$

The currents,  $I_{b1}$ ,  $I_{b2}$ , and  $I_c$ , can be expressed as

$$\begin{aligned} I_{b1} &= I_{b2}/\sigma = 0; \\ I_c &= (I_{c,bo}/\beta_{bo}) \cdot \beta. \end{aligned} \tag{3.14}$$

Since BAs are turned off, the efficiency of overall PD-LMBA is equal to the efficiency of the CA.

- **LM Region** ( $P_{MAX}/OBO \leq P_{OUT} < P_{MAX}$ ): When the power increases to the target OBO level, the BA1 and BA2 are turned on, and the CA reaches saturation at the same time. At

$P_{\text{MAX}}/\text{OBO}$ , the CA is designed to be only voltage-saturated ( $Z_c > Z_{\text{CA,Opt}}$ ) corresponding to the first efficiency peak, while there is still headroom for further increase of CA current. In this region, BA1 and BA2 currents increase proportionally given by

$$I_{b1} = i_{\text{ba1,h}}[1], \quad I_{b2} = \sigma \cdot i_{\text{ba1,h}}[1]. \quad (3.15)$$

By substituting this dependence into Eqs. (3.2) and (4.4), the load modulation behaviors of BA1, BA2 and CA impedances are derived as

$$\begin{aligned} Z_{b1,\text{LM}} &= Z_0 \left( \sigma + \frac{\sqrt{2}I_c e^{j\theta}}{I_{b1}} \right); \\ Z_{b2,\text{LM}} &= Z_0 \left( \left( 2 - \frac{1}{\sigma} \right) + \frac{\sqrt{2}I_c e^{j\theta}}{\sigma I_{b1}} \right); \\ Z_{c,\text{LM}} &= Z_0 \left( 1 - \frac{\sqrt{2}I_{b1}(1 - \sigma)}{I_c e^{j\theta}} \right). \end{aligned} \quad (3.16)$$

The above equation clearly underlines that by setting  $\sigma < 1$  (larger BA1 sizing),  $Z_c$  can be modulated below  $Z_0$  as the power increases beyond OBO. Such a decreasing  $Z_c$  is achieved given the fact that BA1 current ( $I_{b1}$ ) rises much more sharply after turning on as compared to  $I_c$  (i.e.,  $I_{b1}/I_c$  increases with power). Meanwhile, due to the CA LM, the CA current at the predefined OBO ( $I_{c,\text{bo}}$ ) is expected to gradually increase to the full current saturation, i.e.,  $I_{c,\text{max}} = \alpha I_{c,\text{bo}}$ . Similar to the DEPA [19], this LM-induced CA current increase is assumed to be linearly dependent on the driving level,  $\beta$ , given by

$$I_c = I_{c,\text{bo}} \left( \frac{\alpha - 1}{1 - \beta_{\text{bo}}} \beta + \frac{1 - \alpha \beta_{\text{bo}}}{1 - \beta_{\text{bo}}} \right). \quad (3.17)$$

The CA current with a reduced carrier LM ratio of  $\alpha = 1.5$  is plotted in Fig. 3.3. Compared to DPA with full LM ratio of  $\alpha = 2$ , the CA current of PD-ALMBA increases with different slopes in different regions.

- **Saturation Region** ( $P_{\text{OUT}} = P_{\text{MAX}}$ ): When the output power reaches the maximum, CA and BA are fully saturated at the same time. The currents of all amplifiers reach to their maximum value, which can be expressed as

$$\begin{aligned} I_{b1} &= I_{b1,\text{max}}, \quad I_{b2} = \sigma \cdot I_{b1,\text{max}}; \\ I_c &= I_{c,\text{max}} = \alpha \cdot I_{c,\text{bo}}. \end{aligned} \quad (3.18)$$

In this saturated region,  $I_c$  will expand to  $\alpha \cdot I_{c,\text{max}}$  due to CA-LM. Since CA bias voltage remains constant,  $Z_c$  will decrease from  $Z_0$  to  $Z_0/\alpha$ . The load impedances of BA1, BA2, and CA are given by

$$\begin{aligned} Z_{b1,\text{SAT}} &= Z_0 \left( \sigma + \frac{\sqrt{2} I_{c,\text{max}} e^{j\theta}}{I_{b1,\text{max}}} \right); \\ Z_{b2,\text{SAT}} &= Z_0 \left( \left( 2 - \frac{1}{\sigma} \right) + \frac{\sqrt{2} I_{c,\text{max}} e^{j\theta}}{\sigma I_{b1,\text{max}}} \right); \\ Z_{c,\text{SAT}} &= Z_0 \left( 1 - \frac{\sqrt{2} I_{b1,\text{max}} (1 - \sigma)}{I_{c,\text{max}} e^{j\theta}} \right) = \frac{Z_0}{\alpha}. \end{aligned} \quad (3.19)$$

It is interesting to note that the carrier LM of PD-ALMBA can be set as a continuum between PD-LMBA ( $\alpha = 1$ ) and DPA ( $\alpha = 2$ ), depending on the target need for over-driving reduction of CA and the overall PD-ALMBA performance. Based on the above theoretical analysis, the amplitude and phase control between three amplifiers, i.e., BA1, BA2, and CA, govern their load modulation behaviors and the general operation of the PD-ALMBA, which will be analyzed in detail in the following Subsec. 4.

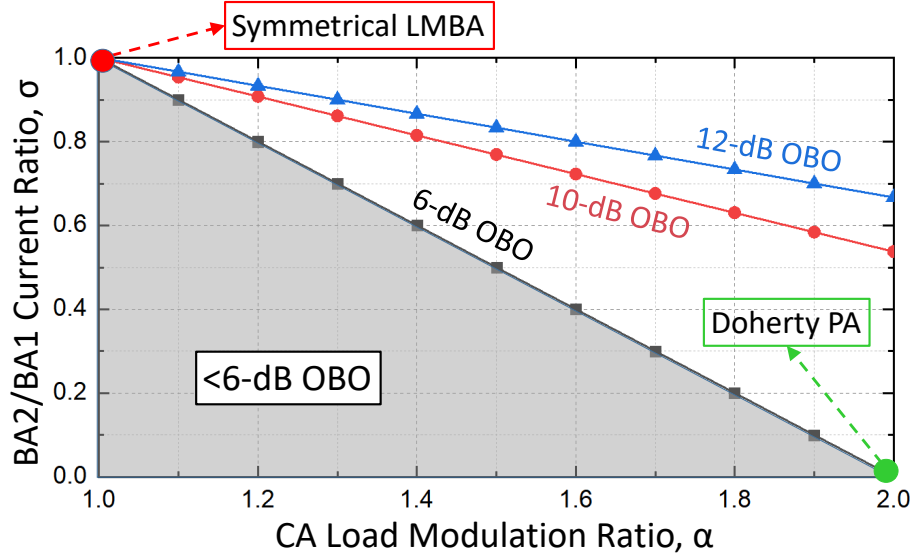


Figure 3.4: The dependence between  $\sigma$  and  $\alpha$  various given target OBO.

#### 3.2.4 Amplitude and Phase Control of PD-ALMBA

Different from the generic LMBA, the amplitude control of ALMBA involves not only the BA-CA scaling ( $I_c/I_{b1}$ ) but also the BA1-BA2 scaling ( $\sigma$ ), as indicated by (4.20). In the PD-ALMBA operation, BA1 and BA2 need to be turned on at a pre-determined back-off power, where CA reaches its voltage saturation. After all amplifiers are fully saturated, the total saturation power in combination of BA1, BA2, and CA should be scaled proportionally, i.e.,  $\text{OBO}_{\text{dB}}$  dB higher than the back-off level. Based on the ideal model in Fig. 3.2, the power scaling ratio between BA1, BA2, and CA can be determined by

$$\begin{aligned} \frac{1}{2} \text{OBO} \cdot \left( \frac{I_{c,\max}}{\alpha} \right)^2 \cdot Z_0 &= \frac{1}{2} I_{c,\max}^2 \cdot \frac{Z_0}{\alpha} + \frac{1}{2} I_{b1,\max}^2 \cdot R_{b1,\text{sat}} \\ &+ \frac{1}{2} I_{b2,\max}^2 \cdot R_{b2,\text{sat}}. \end{aligned} \quad (3.20)$$

The dependence between  $\sigma$  and  $\alpha$  under different target OBO ranges can be derived with a combination of Eqs. (3.19), (3.18), and (3.20), and the results are graphically presented in Fig. 3.4. As an interesting phenomenon observed in Fig. 3.4,  $I_{b2} = 0$  is required to result in 6 dB of OBO and 2 of LM ratio, indicating the fact that the PD-ALMBA is converged to a standard DPA with the quadrature coupler functioning as an ideal Doherty combiner [58]. The upper right half region of Fig. 3.4 marks the extended OBO range ( $> 6$  dB) that can be utilized in practical designs for amplification of high-PAPR signals.

In addition to amplitude control, it is necessary to ensure that the phase difference between the current generators is properly set to result in optimal load modulation trajectories of each amplifier. As described in (4.20), by setting  $\theta = 0$ , a purely resistive load modulation of  $Z_{b1}$ ,  $Z_{b2}$ ,  $Z_c$  can be achieved, which represents the optimal LM behavior according to the load-line theory [38]. Fig. 3.5 shows the analytically calculated LM trajectories of BA1, BA2 and CA for variations of phase offset ( $\theta$ ) and CA LM ratio ( $\alpha$ ) under a constant OBO of 10 dB. All the LM traces can be maintained on the real axis of Smith chart for  $\theta = 0$ . In realistic design with matching networks and parasitics of transistors, the optimal BA-CA phase offset will be determined through exhaustive sweeping in the actual circuit schematic.

In summary, this section articulates a unified theory of quadrature-coupler-based amplifier with active load modulation of three different driving sources. The equations derived in this section prove that the asymmetry between BA1 and BA2 not only maintains the validity of LMBA architecture in Fig. 3.2 but also leads to a continuum LM ratio of CA. Moreover, the LM of BA1, BA2 and CA can be performed individually in this PD-ALMBA topology, which is able to inherit the wideband and high-efficiency characteristics of symmetrical PD-LMBA. Meanwhile, the reduced CA over-driving leads to promising potential of improved linearity and reliability.



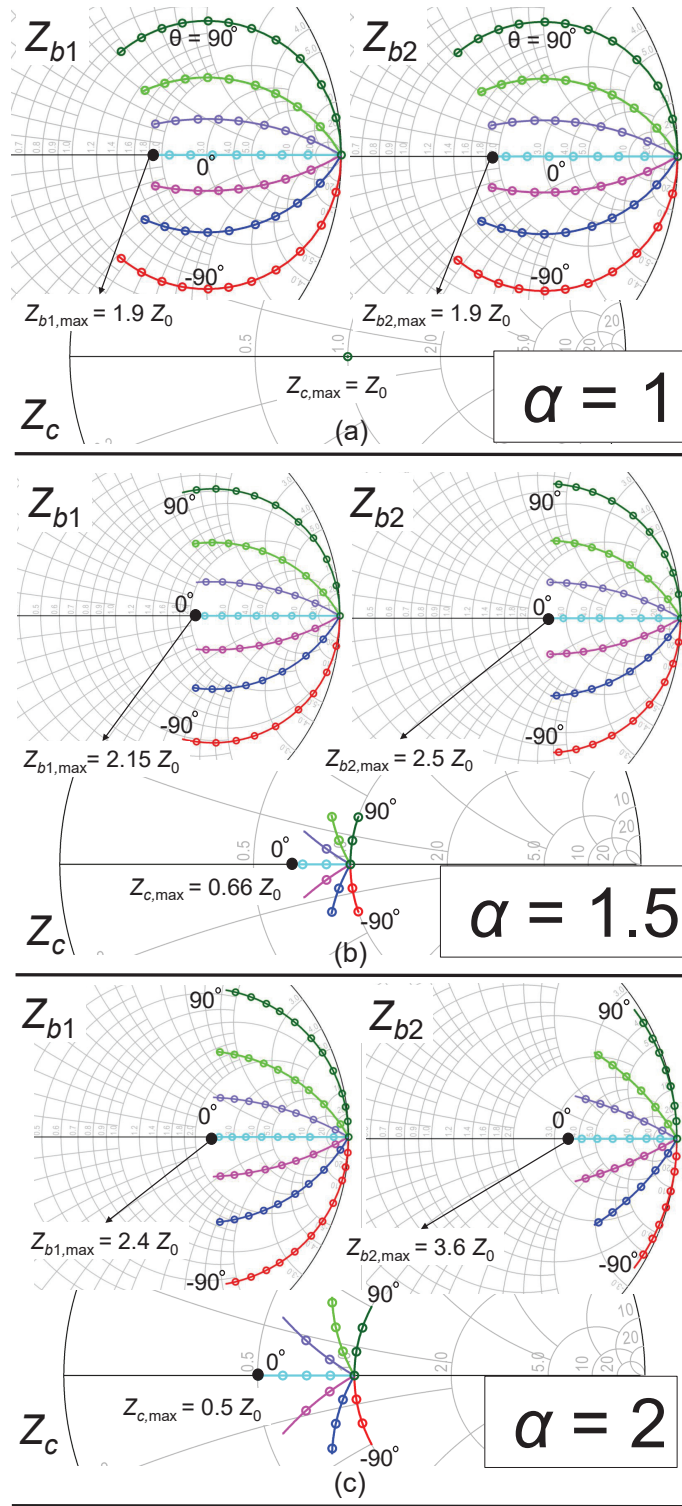


Figure 3.5: The continuum of BA1, BA2 and CA load modulations using the ideal generalized model for  $OBO = 10$  dB and various CA-LM ratio,  $\alpha$ .

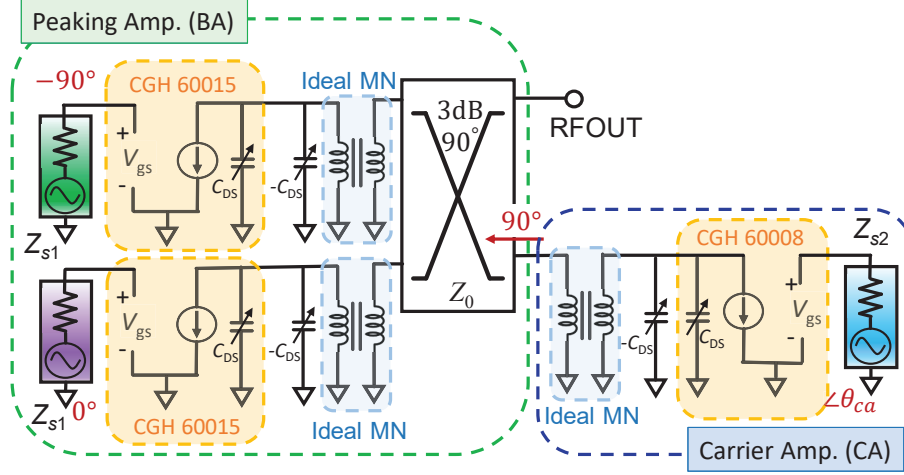


Figure 3.6: Emulated model setup of the proposed PD-ALMBA with bare-die GaN transistors.

### 3.3 Verification using Emulated Ideal PD-ALMBA Model

In order to verify the PD-ALMBA theory proposed in Sec. 4, an ideal PD-ALMBA is emulated using bare-die GaN transistors and ideal quadrature coupler. The bare-die devices have minimized parasitics, which can closely mimic the behaviors of the ideal current generators in Fig. 3.2.

#### 3.3.1 Emulation of Ideal PD-ALMBA Model

Two different types of bare die transistors are used to establish the emulated ideal PD-ALMBA, as shown in Fig. 3.6. Specifically, BA1 and BA2 are built with CGH60015 model from Wolfspeed. The intrinsic parasitic capacitance of the transistors ( $C_{DS}$ ) is de-embedded using a dedicated negative capacitance,  $-C_{DS}$ . Therefore, the combo of transistor and  $-C_{DS}$  can emulate an ideal current source. The input impedances for BA1 and BA2 are set to  $Z_{s1}$  obtained using the source-pull. Due to the LM of CA as derived in (3.19), the impedances of BA1 and BA2 at saturation power (i.e.,  $Z_{b1,sat}$  and  $Z_{b2,sat}$ ) are different from the coupler characteristic impedance ( $Z_0 = 50 \Omega$ ). In order

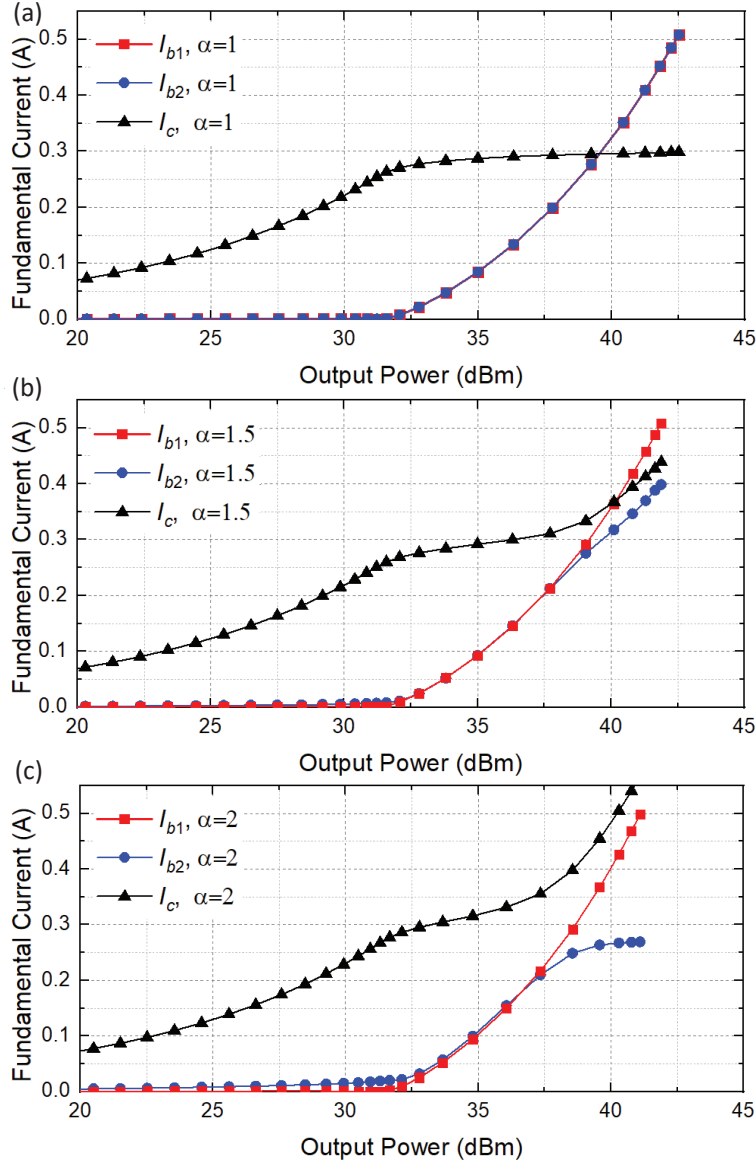


Figure 3.7: Simulated BA1, BA2 and CA currents using emulated PD-ALMBA model at 1.7 GHz for different LM ratios: a)  $\alpha = 1$ , b)  $\alpha = 1.5$ , c)  $\alpha = 2$ .

to study the continuum of LM behavior ( $\alpha$  from 1 to 2), the transformer design is based on the symmetrical case ( $\alpha = 1$ ) in which  $Z_{b1,\text{sat}}$  and  $Z_{b2,\text{sat}}$  are matched to  $R_{\text{Opt}}$  of the transistor. Then, the power asymmetry of BA1 and BA2 (i.e.,  $\sigma < 1$ ) is realized by offsetting the bias voltages of BA1 and BA2 for practically achieving  $\alpha > 1$ .

The output of control amplifier is connected to the isolation port of the coupler. Considering that the output power of CA is much less than the total output power of BA, the bare-die CGH60008 model from Wolfspeed is selected with a smaller device size. The input impedance of CA is set to  $Z_{s2}$ , which is obtained from source-pull simulation result. Due to the fact that the CA impedance is modulated from  $Z_0$  to  $Z_0/\alpha$  at the coupler interface, the same LM range is transformed to CA transistor by another ideal transformer with optimized transformation ratio based on the CA power and bias voltage. It turns out that the CA transistor with reduced  $V_{DD}$  desires  $R_{Opt,CA} \approx Z_0$ , leading to a 1 : 1 transformer for CA.

According to Fig. 3.2 and (4.18), the ideal phase offset between BA1 ( $I_{b1}$ ) and the control source power (CSP,  $jI_c e^{j\theta}$ ) is  $90^\circ$  at the coupler interface plane, such that the resistive load modulation can be achieved by setting  $\theta = 0^\circ$ . Therefore, the CA input phase ( $\theta_{CA}$ ) needs to be properly selected to ensure that a  $90^\circ$  phase offset is maintained at the coupler interface for BA1 path and CA path.

### 3.3.2 Simulation Results

Fig. 3.7 shows the simulated fundamental current of the PD-ALMBA emulated model with different  $\alpha$  values. The simulation results in Fig. 3.7(a) clearly show that when  $I_{b1}$  and  $I_{b2}$  are identical,  $\alpha$  is equal to 1, and the CA remains in the saturation region with constant  $I_c$  beyond the back-off point. However, for  $I_{b1} > I_{b2}$ ,  $\alpha$  becomes greater than 1, and  $I_c$  continues to increase after turning-on of BA, shown in Fig. 3.7(b)(c). This PD-ALMBA model is able to alleviate the over-driving problem of CA. On the other hand, an excessively large value of  $\alpha$  may also cause adverse effects for identical matching of BA1 and BA2. As observed in Fig. 3.7(c) with  $\alpha = 2$ ,  $I_{b2}$  reaches saturation earlier than BA1, which may cause over-driving of BA2. While this can be solved by designing different transformers to BA1 and BA2, it may complicate the design since different

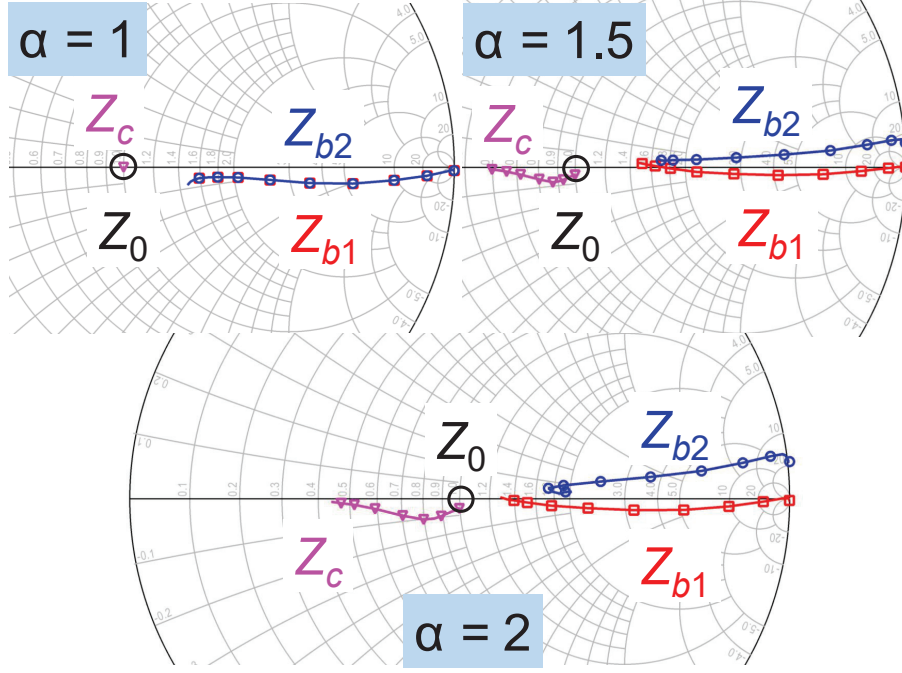


Figure 3.8: Simulated BA and CA load modulation trajectories of different  $\alpha$  at 1.7 GHz using emulation PD-ALMBA model.

matching networks can have different frequency response. Therefore, in actual circuit design in this paper,  $\alpha \approx 1.5$  is selected as the sweep spot of CA LM ratio.

Fig. 3.8 shows the emulated model load trajectory of BA1, BA2 and CA with various  $\alpha$  at 1.7 GHz. As seen from the figure, when  $\alpha = 1$ ,  $Z_c$  equal to  $Z_0$ , and the maximum values of  $Z_{b1}$  and  $Z_{b2}$  are equal; when  $\alpha$  is greater than 1,  $Z_c$  is modulated along a resistive load trajectory in which the impedance decreases from  $Z_0$  to  $Z_0/\alpha$ , while  $Z_{b2,Sat}$  is greater than  $Z_{b1,Sat}$ . The simulation results are consistent with the theoretical derivation in Sec. 4, solidly proving the proposed ALMBA/PD-ALMBA theory. Fig. 3.9 shows the simulated efficiency of different emulation models with different  $\alpha$  at 1.7 GHz. The results show that the increase of LM ratio ( $\alpha$ ) does not affect the overall output efficiency and gain on the basis of reducing CA over-driving.

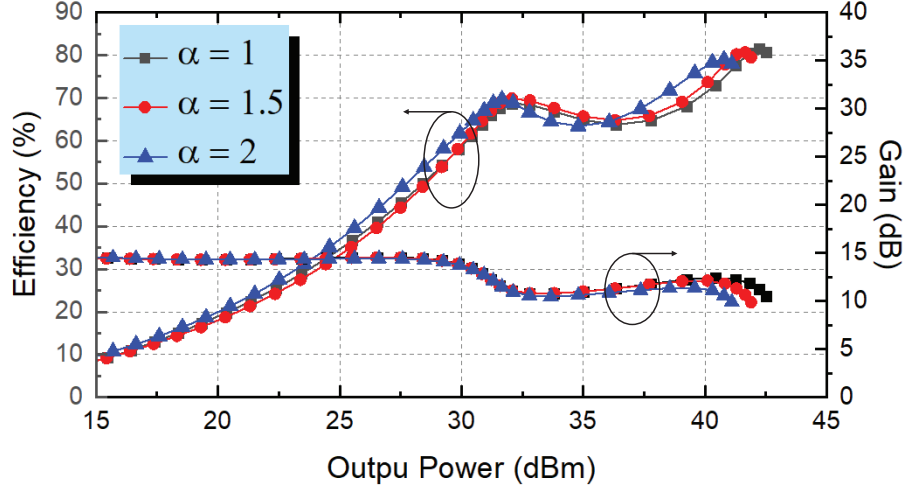


Figure 3.9: Simulated power-swept efficiency of different  $\alpha$  at 1.7 GHz.

### 3.4 Practical Design of Ultra-Wideband PD-ALMBA

Based on the PD-ALMBA theory and emulation presented in Secs. 4 and 3, the LM ratio of CA,  $\alpha$ , is directly related to the asymmetry of BA1 and BA2,  $\sigma$ , and the target OBO range. Considering the sweet spot of PD-ALMBA operation, a reduced CA LM ratio of  $\alpha = 1.5$  is targeted in the practical design [20]. To accommodate the high PAPR of emerging 4G and 5G signals, the target OBO is set to 10-dB. Two 10-W commercial GaN HEMTs (Wolfsped CGH40010F) are used as the active devices for both BA1 and BA2, which are combined through two commercial quadrature couplers (IPP-2281IT from Innovative Power Products). To achieve the target CA modulation, the BA2 power is down-scaled from BA1 by reducing the BA2 supply voltage, which is finally determined through circuit simulation. Due to the fact that the CA power is much lower as compared to BA, the physical circuit of CA is constructed using a 6-W GaN transistor (Wolfsped CGH40006P), while the CA power is practically controlled with reduced  $V_{DD,CA}$  in the actual circuit. The overall realized circuit schematic is shown in Fig. 3.10(a). The target frequency range is 0.55 to 2.2 GHz, covering a majority of cellular communications bands.

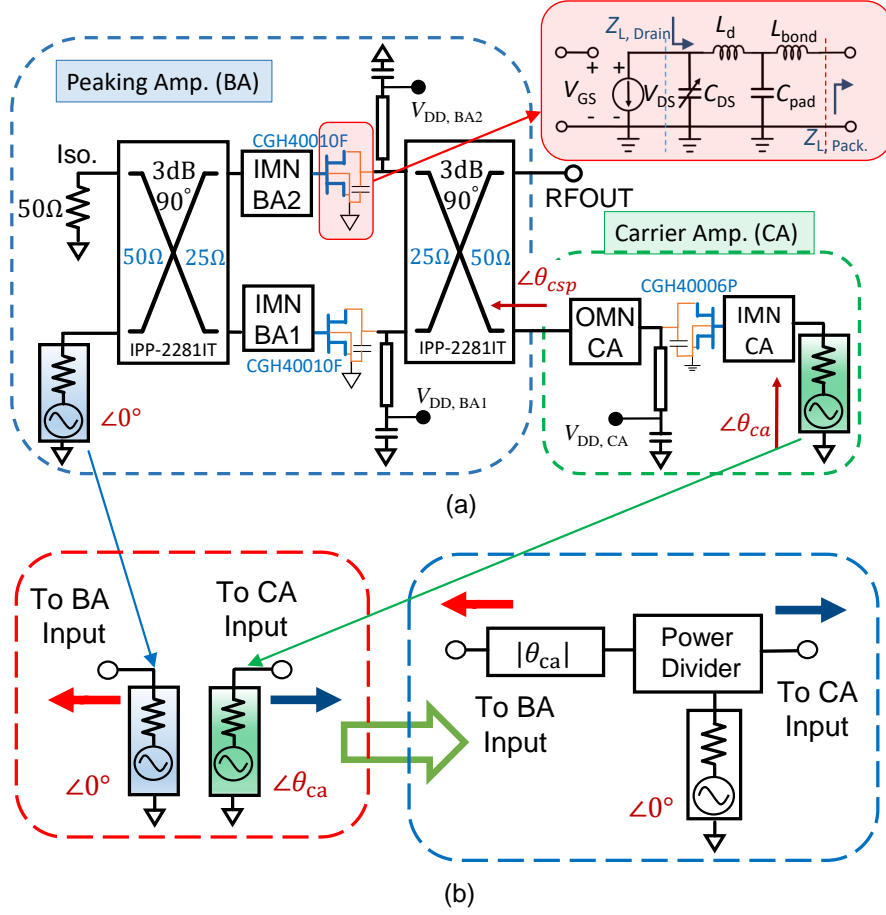


Figure 3.10: (a) Simulation setup of the proposed PD-ALMBA using realistic GaN transistors de-embedded with parasitic networks; (b) Design of TL-based wideband phase shifter for merging the BA and CA inputs.

#### 3.4.1 Design of Asymmetrical Balanced Amplifier

Using similar approach as presented in [31, 55, 59], the wideband matching for the transistor is primarily realized with a wideband non-50- $\Omega$  quadrature coupler and a bias line. As the schematic shown in Fig. 3.10, this circuit implementation of BA eliminates the complex wideband output matching network, resulting in minimized dispersion effect and simplified load-modulation control.

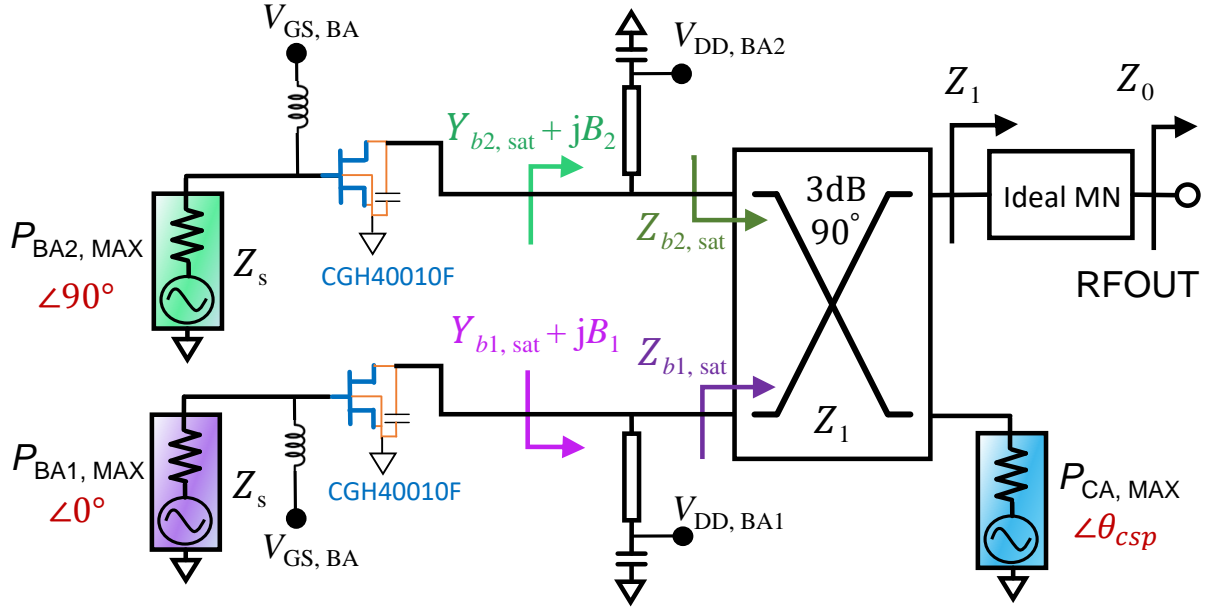


Figure 3.11: BA matching design at maximum power.

A fact is noted that the packaged GaN transistor (e.g., CGH40010F) desires a nearly constant real part of load admittance ( $Y_L = G_L + jB_L$ ) over wide frequency range extracted from the load-pull simulation, also seen in [46, 47, 48]. According to the expressions of  $Z_{b1, sat}$  and  $Z_{b2, sat}$  in (3.19), BA1 and BA2 see different impedances at the quadrature coupler plane with the contribution of CA. Therefore, to determine the characteristic impedance of the quadrature coupler,  $Z_1$ , co-simulation with CA is needed, which is modeled as an ideal source (CSP) with maximum CA power  $P_{CA, MAX}$  ( $= \alpha P_{MAX}/OBO$  as for estimation) at a proper phase.  $Z_1$  is optimized such that  $Y_{b1, sat}$  and  $Y_{b2, sat}$  are both close to  $G_{L, Opt}$ . Since BA1 generates the highest power, the optimization of  $Y_{b1, sat}$  is given higher priority. The bias-line parameters (i.e., length and width) are utilized to provide dedicated values of  $B_L$  for BA1 and BA2 over the target frequency range. The detailed design procedure is described in Fig. 3.11. The circuit simulation results show that  $Z_1$  of 20 – 30  $\Omega$  is the optimal value for covering the target frequency range. Therefore, a wideband impedance-transformer (2 : 1) coupler (IPP-2281IT, commercially available from Innovative Power Product) is utilized to provide



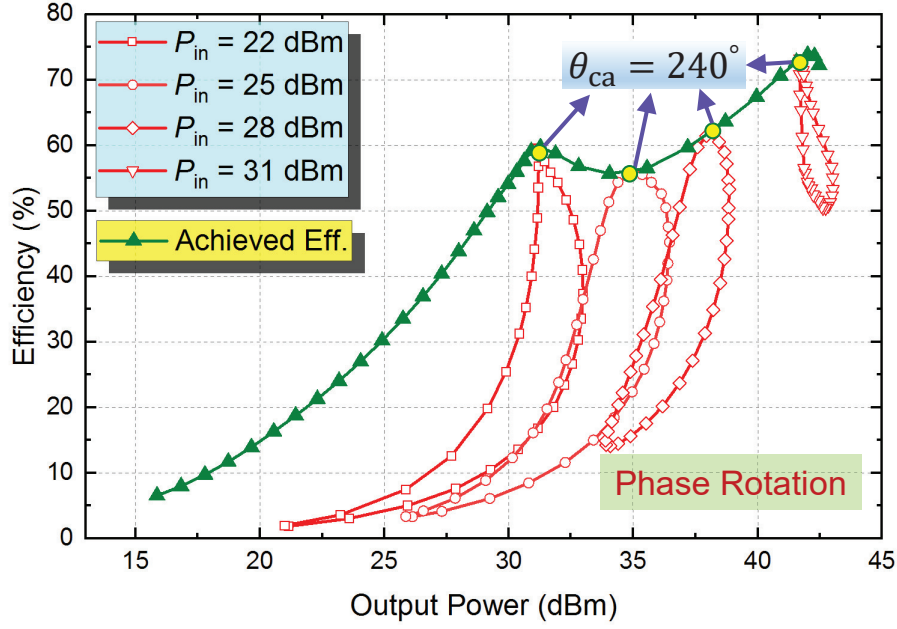


Figure 3.12: Determination of the optimal BA-CA phase offset based on dual-input circuit schematic in Fig. 3.6 at 1.0 GHz through phase-swept input stimulus of CA.

the desired BA matching.

The same transformer coupler is used for the input quadrature division of BA, leading to an eased transformation ratio of input matching, i.e., from  $25 \Omega$  to the designated source impedance  $Z_s$ . The physical matching circuit is realized using the multi-stage lowpass matching network and design method introduced in [46]. Since this design has two octave bandwidths, half of the frequencies have second harmonics in band; therefore, we did not specifically design for harmonic termination but rely on saturation-mode for harmonic shaping [5]. On the other hand, BA1 and BA2 in Class-C mode are already more efficient than CA in Class-AB, so the harmonic matching is not necessary for BAs.

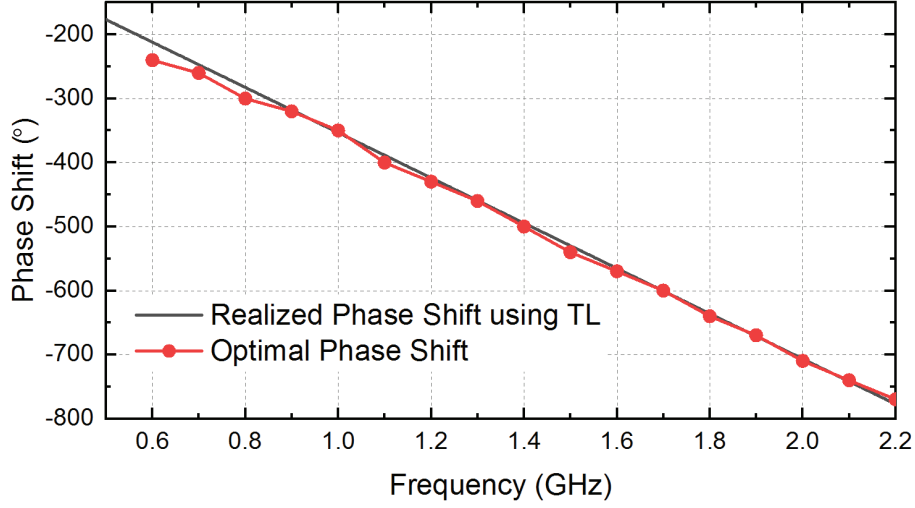


Figure 3.13: Simulated optimal BA1-CA phase offset at different frequencies.

### 3.4.2 Design of Control Amplifier

According to the amplitude control scheme described in Secs. 4 and 3, the OBO power of CA determines the dynamic range once the BA design is fixed. Given a specific OBO, the saturation power of CA can be determined by

$$\text{OBO} \times \frac{P_{\text{CA},\text{MAX}}}{\alpha} = P_{\text{BA1},\text{MAX}} + P_{\text{BA2},\text{MAX}} + P_{\text{CA},\text{MAX}} \quad (3.21)$$

To achieve the target OBO of 10 dB,  $P_{\text{CA},\text{MAX}}$  should be around 7.5-dB below  $P_{\text{BA1},\text{MAX}} + P_{\text{BA2},\text{MAX}}$ . To realize this low output power, the CA is implemented with a 6-W GaN transistor (Wolfspeed CGH40006P), and it is biased in Class-AB mode with partial  $V_{\text{DD}}$ .

Since the CA is connected to the isolation port of the transformer coupler, the CA design is based on the 50- $\Omega$  reference impedance. With the target LM ratio of  $\alpha$  set to 1.5,  $Z_c$  (at the coupler plane) should be modulated from 50 to 33  $\Omega$  as the power increases from 10-dB OBO to maximum, shown in Fig. 3.5(b). The LM ratio of CA ( $\alpha$ ) is determined by the asymmetry of BA1 and

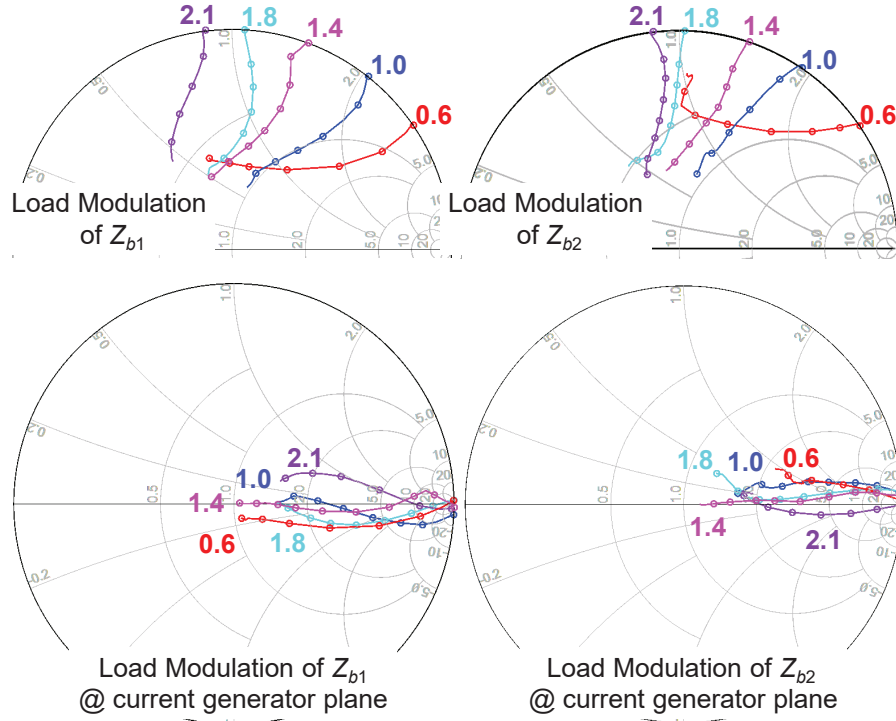


Figure 3.14: Load modulation of  $Z_{b1}$  and  $Z_{b2}$  across the entire bandwidth for  $\alpha = 1.5$ .

BA2, which is practically realized using the combination of 1) fluctuation of quadrature coupler's transmission/coupling coefficients over frequency that is inevitable for wideband couplers, and 2) reduction of BA2 bias voltage. Thus, output matching of CA is required to transform this LM behavior from the coupler plane to the transistor package plane and eventually to the intrinsic drain plane. In the actual design of this paper, a three-section transmission line matching network is designed, and the CA matching is eventually optimized through co-simulation with the designed BA.

The input matching network design of CA followed the same methodology as wideband input design of BA1 and BA2, and a three-section lowpass network based on transmission lines is designed to provide wideband input matching for the selected GaN transistor. Considering the complexity

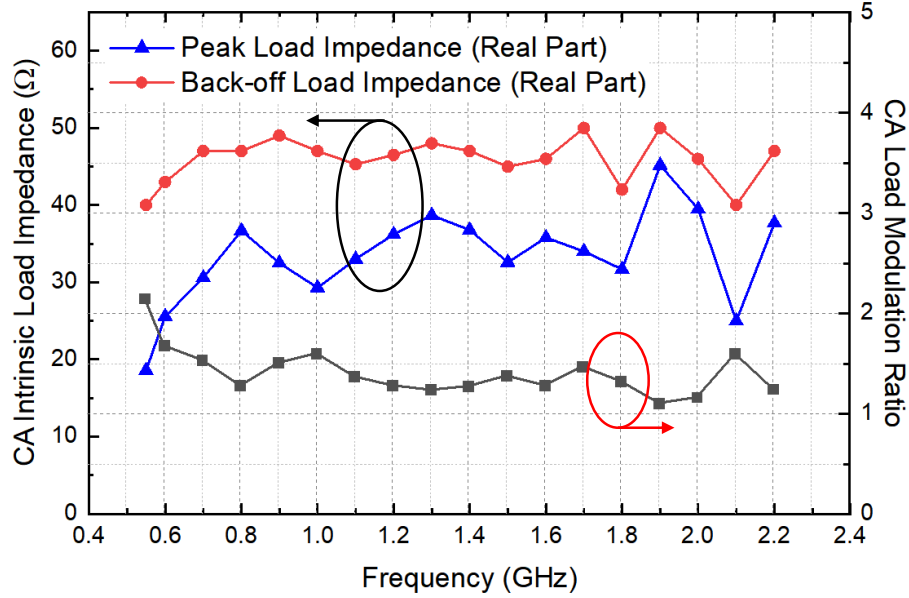


Figure 3.15: Simulated CA load-modulation behavior across the entire frequency band.

of the design and the dual-octave bandwidth, the harmonic control circuitry is not particularly included in this work. However, if certain harmonic matching is involved in CA design, it can potentially further improve the PD-ALMBA OBO efficiency.

### 3.4.3 BA-CA Phase Offset Design Over Ultra-Wide Bandwidth

After finishing the design of BA1, BA2 and CA, the load modulation of all three amplifiers is mainly determined by the relative phase between BA1 and CA, as described in (4.20). In order to ensure the resistive load modulation of BA1, BA2, and CA for maximized back-off efficiency, the BA1-CA phase offset is required to be  $\theta = 0^\circ$  (equivalent to  $\theta_{\text{CSP}} = 90^\circ$ ) at the coupler plane. With the practical BA and CA incorporated with the coupler, the phase offset optimization is moved to the inputs of BA and CA, which can be determined using the dual-input (with equal amplitude [29]) schematic shown in Fig. 3.12. It is worth noting that the optimal phase shift between BA and



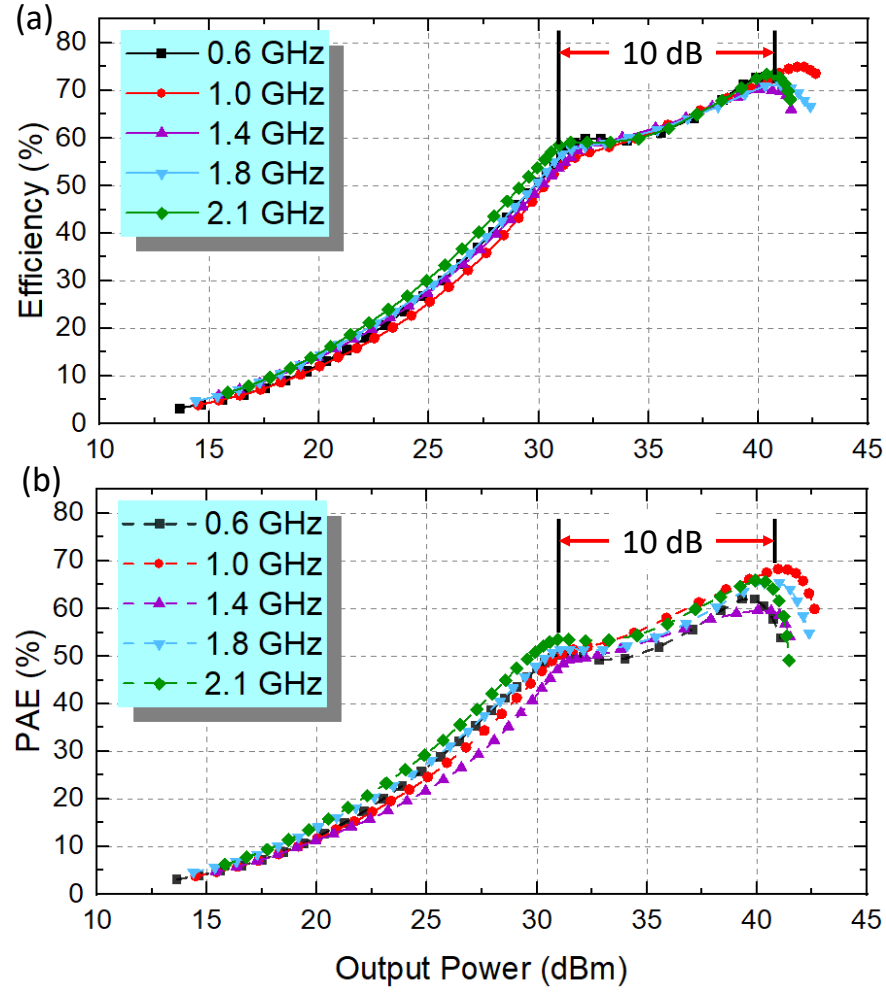
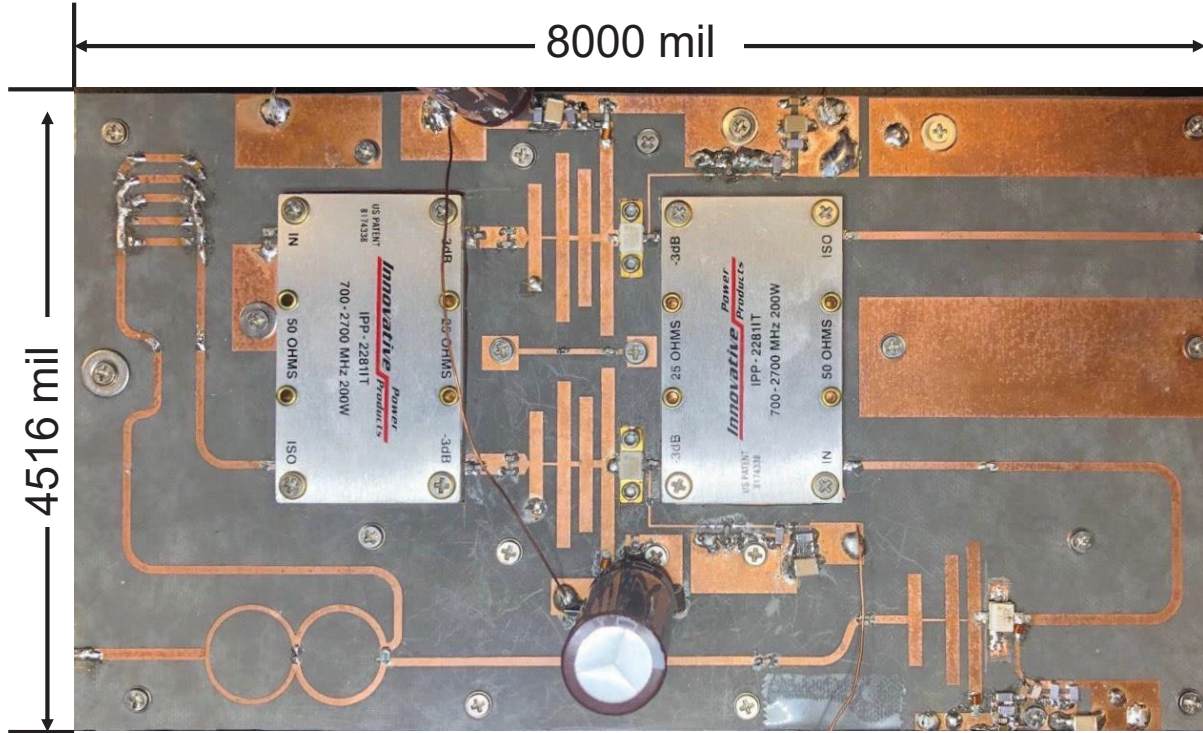


Figure 3.17: Power-swept CW simulation results of the designed PD-ALMBA with the best BA-CA phase setting at different frequencies: (a) drain efficiency, (b) PAE.

at the intrinsic drain plane are shown in Fig. 3.15, indicating that the target LM ratio of 1.5 can be achieved across the target band. The CA-LM trajectory travels nearly on the real axis with very small fluctuations, as shown in Fig. 3.8, so the imaginary part changes of CA are ignored.



20-mil Thick Rogers Duroid-5880;  $\epsilon$ : 2.2

Figure 3.18: Fabricated PD-ALMBA prototype.

#### 3.4.4 Overall Schematic and Simulation Results

The finalized circuit schematic of overview is shown in Fig. 3.16, all actual circuit-element values are exhibited next to the schematic. The gate bias voltages of BA1 and BA2 are properly set such that they turn on around 10 dB power back-off, where the CA load modulation is performed concurrently.

Through the design of the wideband BA1, BA2, CA and phase shifter described in above sections, the overall efficiency and PAE of the PD-ALMBA are simulated with swept input power, as shown in Fig. 3.17. It is clearly seen that a high efficiency is achieved at the peak power, and the back-off efficiency is significantly enhanced down to 10-dB OBO. This Doherty-like efficiency and PAE

profile can be well maintained over extended frequency range.

Table 3.1: State-of-the-Art of Wideband Load-Modulated Power Amplifiers

Ref. / Year	Architecture	Freq. (GHz)	FBW (%)	$P_{\text{Max}}$ (dBm)	DE @ $P_{\text{Max}}$ (%)	DE @ HBO (%)	DE @ LBO (%)
[49] 2018	3-Way DPA	0.6-0.9	40	46.1-46.9	51.1-78	51.9-66.2@6 dB	42-64@9.5 dB*
[21] 2018	3-Way DPA	2.0-2.6	26	43.6-45.4	53-76	45-55@6 dB	41-48@8 dB
[22] 2019	3-Way DPA	1.6-2.6	48	45.5-46	53-66	52-66@6 dB	50-53@9.5 dB
[40] 2016	DPA	1.6-2.2	31.6	46-47	60-71	50-55@6 dB*	51-55@10 dB
[50] 2018	DPA	1.5-3.8	86.8	42.3-43.4	42-63	33-55@6 dB	22-40@10 dB*
[20] 2019	DEPA	2.55-3.8	40	48.8-49.8	54-67	42-53@6 dB*	47-60@8 dB
[41] 2017	Dual-Input LMBA	4.5-7.5	50	39	47-77*	28-60@6 dB*	40-72@10 dB* <sup>‡</sup>
[42] 2018	Dual-Input LMBA	1.7-2.5	38	48-48.9	48-58*	43-53@6 dB*	33-45@10 dB* <sup>†</sup>
[24] 2017	RF-Input LMBA	0.7-0.85	19	42	57-70	34-48@6 dB	30-35@10 dB* <sup>†</sup>
[29] 2017	RF-Input LMBA	1.8-3.8	71	44	46-70	33-59@6 dB	20-25@10 dB* <sup>†</sup>
[54] 2020	Dual-Mode DPA * <sup>¶</sup>	1.52-4.68	102	41.5	54-71	42-57@6 dB	37-50@10 dB* <sup>†</sup>
[55] 2020	PD-LMBA	1.5-2.7	57	43	58-72	47-61@6 dB	47-58@10 dB
This Work	PD-ALMBA	0.55-2.2	120	41-43	49-82	40-60@6 dB	39-64@10 dB

\* Graphically estimated, <sup>†</sup> PAE, <sup>‡</sup> with reduced  $V_{\text{DD}}$ , <sup>¶</sup> with reciprocal gate bias.

### 3.5 Implementation and Experimental Results

The PD-ALMBA is implemented on a 20-mil thick Rogers Duroid-5880 PCB board with a dielectric constant of 2.2. A photograph of the fabricated PD-ALMBA is shown in Fig. 3.18. The size of the entire circuit is 4.5 inch  $\times$  8 inch. The fabricated PD-ALMBA is measured using both continuous-wave (CW) and modulated LTE signals. In this implemented circuit, CA is biased in Class-AB with a  $V_{\text{DD,CA}}$  around 11 V. BA1 and BA2 are biased in Class-C with 32-V  $V_{\text{DD,BA1}}$  and 24-V  $V_{\text{DD,BA2}}$ , respectively. Fine tuning of  $V_{\text{GS,BA1}}$  and  $V_{\text{GS,BA2}}$  between  $-5$  V and  $-4$  V are performed at different frequencies to optimize the best power-added efficiency (PAE). Fig. 3.19 shows drain DC currents versus output power from CW measurement for BA1, BA2 and CA, where a comparison is experimentally presented between symmetrical and asymmetrical cases. It can be clearly seen from Fig. 3.19(b) that the current of CA continuously increasing after the turning-on of BA for ALMBA. These results exhibit a solid validation of the propose ALMBA theory and well agree with the simulated fundamental currents using emulation model in Fig. 3.7.



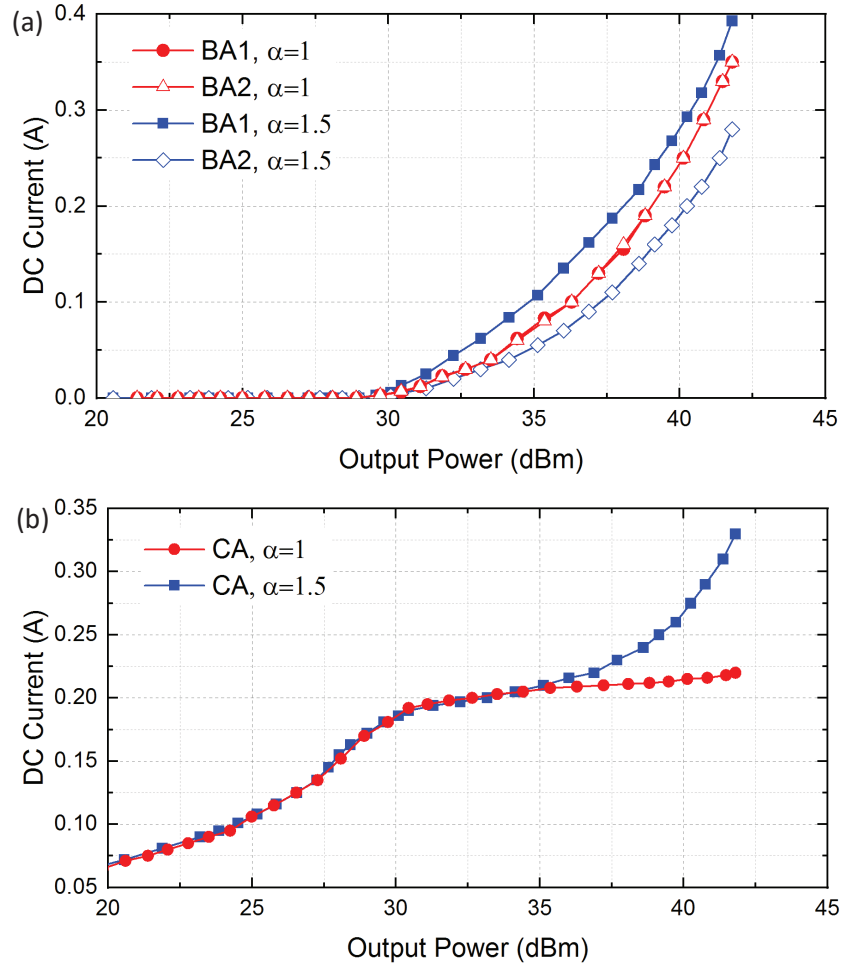


Figure 3.19: Measured drain DC current versus output power of BA1, BA2 and CA at 1.4 GHz, when  $\alpha$  is set to 1 and 1.5, respectively.

### 3.5.1 Continuous-Wave Measurement

The fabricated PD-ALMBA is measured under the excitation of a single-tone CW signal from 0.55 to 2.2 GHz with a large variation of power levels. The CW signal is generated by a vector signal generator, and then boosted by a broadband linear driver amplifier to a sufficiently high level for driving the device under test (DUT). The output power is measured using spectrum analyzer and power sensor. A peak output power of 41 – 43 dBm is measured across the entire bandwidth,

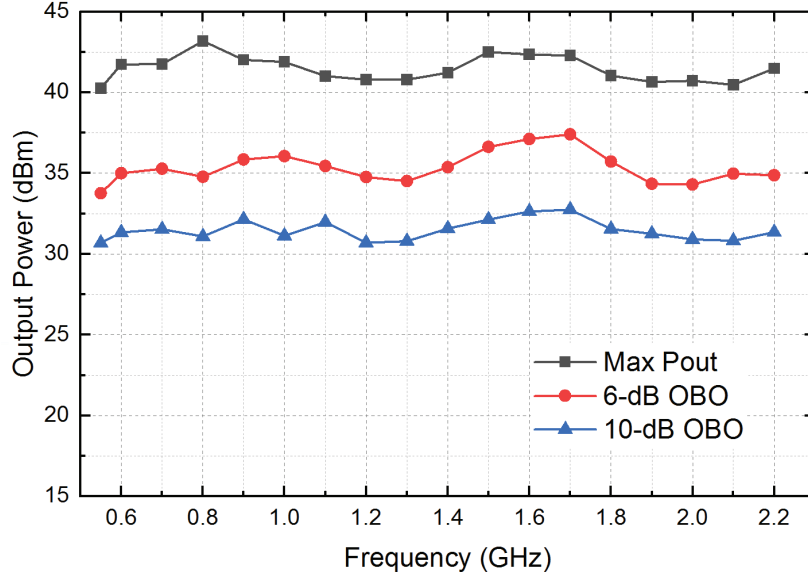


Figure 3.20: Measured output power at various OBO levels from 0.55 to 2.2 GHz.

as shown in Fig. 3.20. In Fig. 3.21, 82% of drain efficiency and 79% of PAE at peak power is measured at 0.7 GHz. The drain efficiency remains higher than 49% and PAE remains higher than 39% throughout entire frequency range. As shown in Fig. 3.21(a), the drain efficiencies at 10-dB and 6-dB OBOs are in the range of 39 – 64% and 40 – 60%, respectively. It can be seen from Fig. 3.22 that the gain is maintained around 8 – 15 dB. Moreover, the PD-ALMBA prototype is measured with a power-swept stimulus at 1-dB step, and the measured efficiency and gain profiles are plotted in Fig. 3.23. A Doherty-like behavior could be clearly observed from the shape of the efficiency versus output power curves at almost every single sample frequency point from 0.55 – 2.2 GHz, while the efficiency is effectively boosted down to 10-dB back-off power, as shown in Fig. 3.23. These measurement results validate the proposed PD-ALMBA concept and demonstrate the advantage of this new technology in PA efficiency enhancement over ultra-wide bandwidth.

Table 5.1 presents a comparison between this design and other recently published active-load-

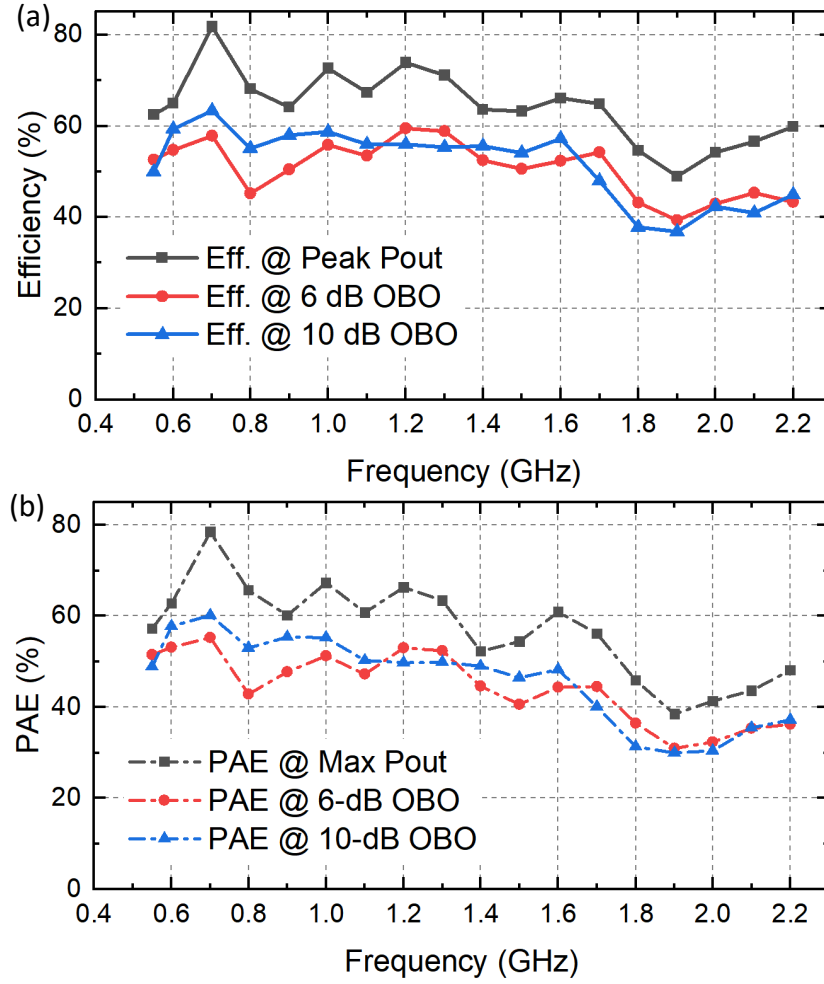


Figure 3.21: (a) Measured drain efficiency at various OBO levels from 0.55 to 2.2 GHz. (b) Measured PAE at various OBO levels from 0.55 to 2.2 GHz.

modulation PAs with similar frequency range, output power level and technology. As a single-input LMBA architecture, this work significantly advances the state-of-the-art by demonstrating the widest RF bandwidth of two octaves together with efficient PA performance across extended OBO range of  $\geq 10$ dB.

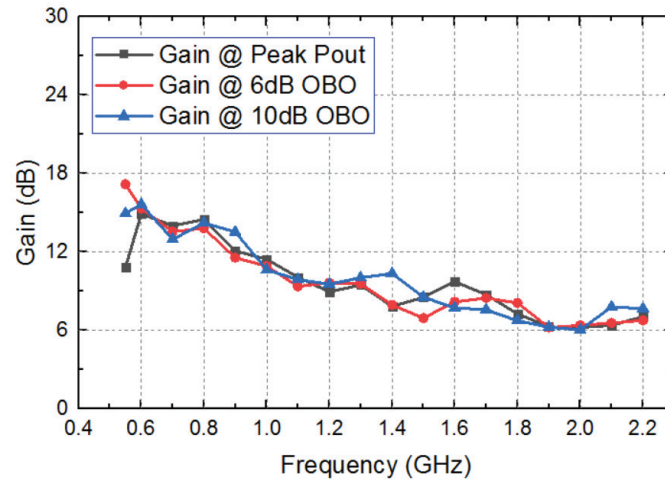


Figure 3.22: Measured gain at various OBO levels from 0.55 to 2.2 GHz.

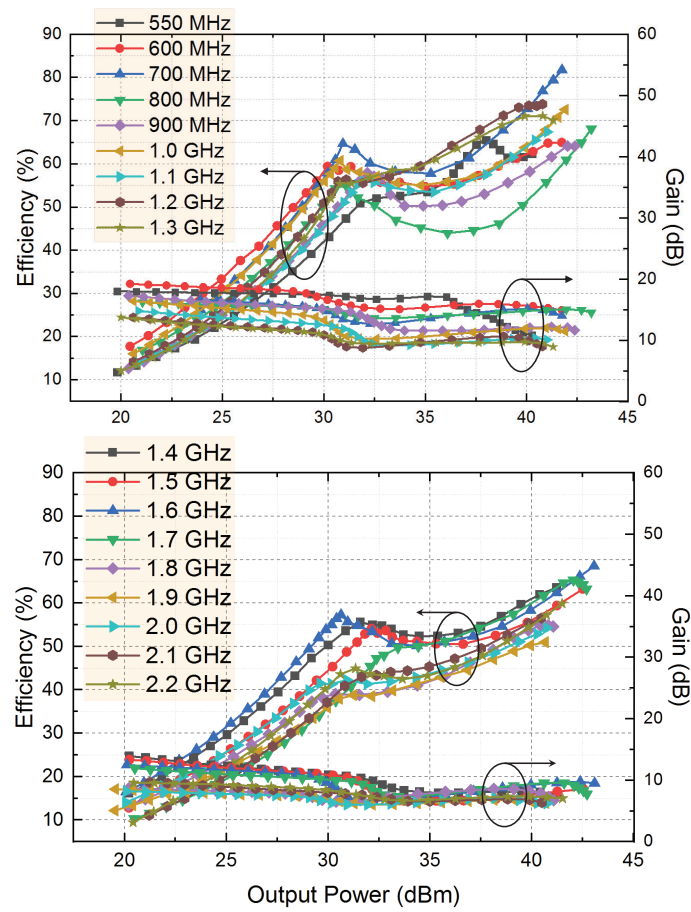


Figure 3.23: Power-swept measurement of efficiency and gain from 0.55 to 2.2 GHz.

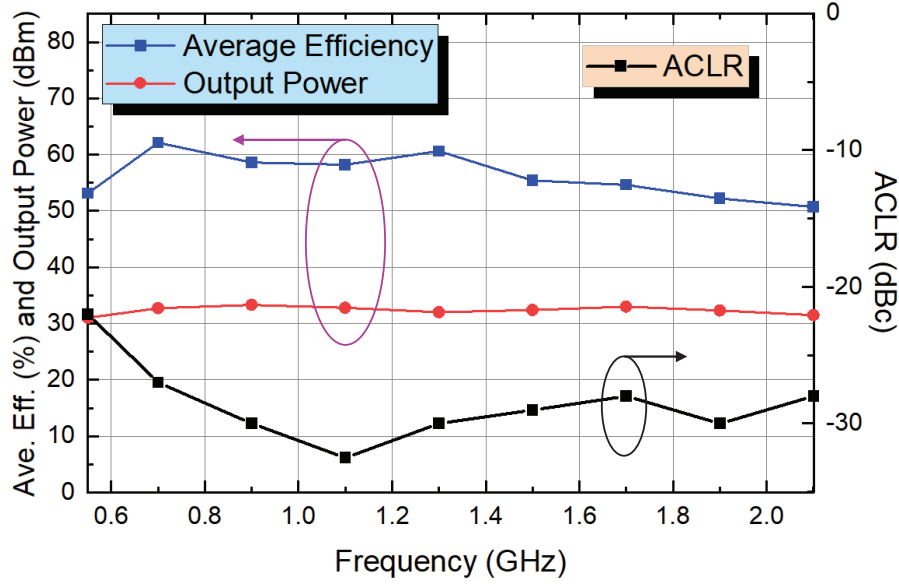


Figure 3.24: Measured average drain efficiency, output power and ACLR with 20-MHz 10.5-dB-PAPR LTE signal at 0.55, 0.7, 0.9, 1.1, 1.3, 1.5, 1.7, 1.9 and 2.1 GHz.

### 3.5.2 Modulated Measurement

To evaluate the capability of the proposed PD-ALMBA under modulated signal stimulation in realistic communications, a 20-MHz LTE signal with a PAPR of 10 dB is employed as the input. The modulated-signal is generated and analyzed by a Keysight PXIe vector transceiver (VXT M9421). The generated LTE signal is further boosted by a linear pre-amplifier (ZHL-5W-422+) to a sufficient level for driving the developed prototype. The measurement results at an average output power around 33 dBm are presented in Fig. 3.24. The PD-ALMBA achieves a high average efficiency of 51% – 62% over the target frequency band. The measured output PSD are shown in Fig. 3.25. The ACLR of most measured frequencies are higher than 28 dB without any digital predistortion. This linearity performance is considerably improved across the entire band in comparison with the ACLR results of PD-LMBA in [55]. In the actual measurement, the drain and gate bias voltages of BA1 and BA2 can be adjusted separately to further optimize the PD-ALMBA lin-

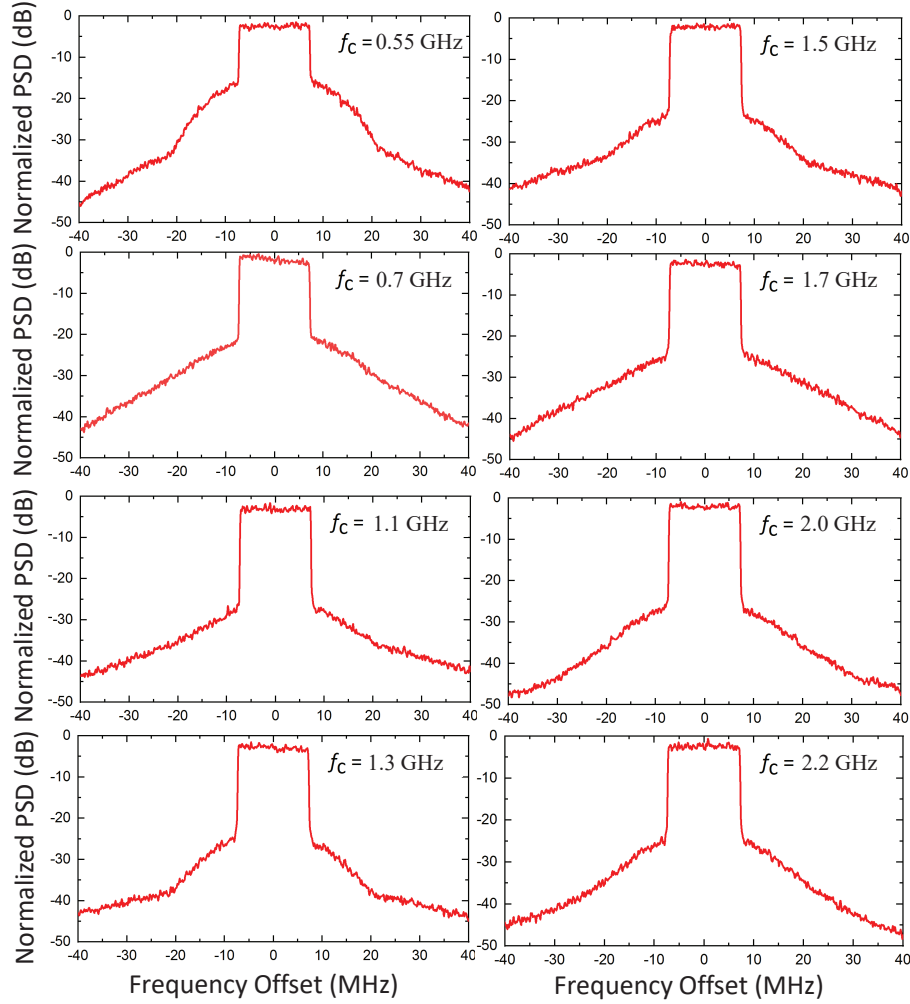


Figure 3.25: Output spectrum from modulated measurement using a 20-MHz 10.5-dB-PAPR LTE signal centered at 0.55, 0.7, 1.1, 1.3, 1.5, 1.7, 2.0 and 2.2 GHz.

earity. Fig. 3.26 shows the comparison of the modulated measurement between PD-LMBA (same prototype with symmetrical bias for BA1 and BA2) and PD-ALMBA (asymmetrical bias) using a dual-carrier LTE-Advanced (LTE-A) signal with 40-MHz bandwidth and 10.5-dB PAPR. The linearity is substantially enhanced with up to 10-dB reduction of ACLR at two sample frequencies at 1 GHz and 1.7 GHz, respectively. Overall, the linearity enhancement of PD-ALMBA as compared to PD-LMBA mainly attributes to the reduced CA over-driving and the cooperation with asymmetrical BA1 and BA2.

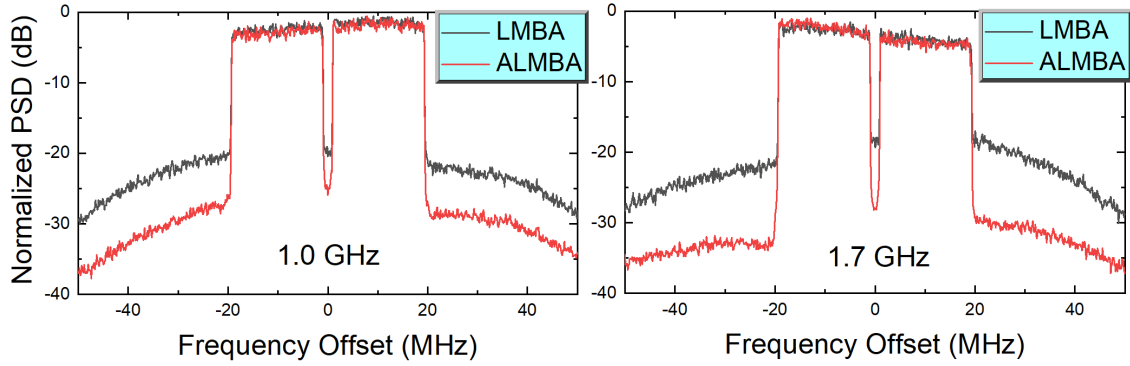


Figure 3.26: Output spectrum comparison between PD-LMBA and ALMBA from modulated measurement using a 40-MHz 10.5-dB-PAPR dual-carrier LTE-A signal centered at 1.0 and 1.7 GHz.

### 3.6 Conclusion

A new load-modulation platform of ALMBA is presented in this paper together with the design methodology and implementation. A unified theory of quadrature-coupler based load modulation PA is unveiled through rigorous analysis and derivation. This new ALMBA theory significantly expands the design space and implementation horizon of conventional LMBA. It is for the first time proved that the control amplifier can be designed with arbitrary LM ratio by properly setting the asymmetry of BA's two sub-amplifiers, BA1 and BA2. Based on Doherty-like biasing of the asymmetric BA1 & BA2 (peaking) and the control amplifier (carrier) with appropriate amplitude and phase controls, the optimal LM performances of three amplifiers can be achieved independently over extended power back-off range and ultra-wide RF bandwidth. Moreover, the LM of CA can effectively alleviate the over-driving issue imposed on the symmetric PD-LMBA, thus improving the overall reliability and linearity. The proposed theory and design methodology have been experimentally validated through hardware prototyping, demonstrating the capability of efficiently amplifying a signal with 10-dB PAPR over a 120% fractional bandwidth, which inherits the wideband and high-efficiency characteristics of symmetrical PD-LMBA. This design has significantly advanced the state-of-the-art. Meanwhile, the reduced CA over-driving leads to about

10-dB ACLR reduction over entire bandwidth, which greatly improves the PD-ALMBA linearity and reliability. This proposed PD-ALMBA provides a promising solution for next-generation multi-band wireless transmitters.



## **CHAPTER 4: CONTINUOUS-MODE HYBRID ASYMMETRICAL LOAD-MODULATED BALANCED AMPLIFIER**

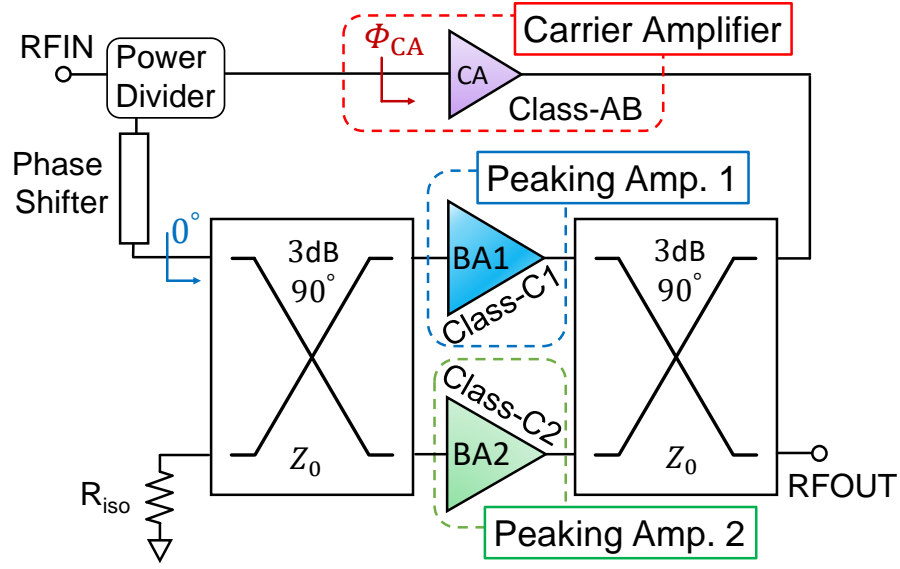
This chapter is based in part on the previously published article listed below. I have permission from my co-authors and publishers to use the work listed below in my dissertation. [“Continuous-Mode Hybrid Asymmetrical Load-Modulated Balanced Amplifier With Three-Way Modulation and Multi-Band Reconfigurability,” in *IEEE Transactions on Circuits and Systems I: Regular Papers*, vol. 69, no. 3, pp. 1077-1090, March 2022, doi: 10.1109/TCSI.2021.3129166.].

### **4.1 Introduction**

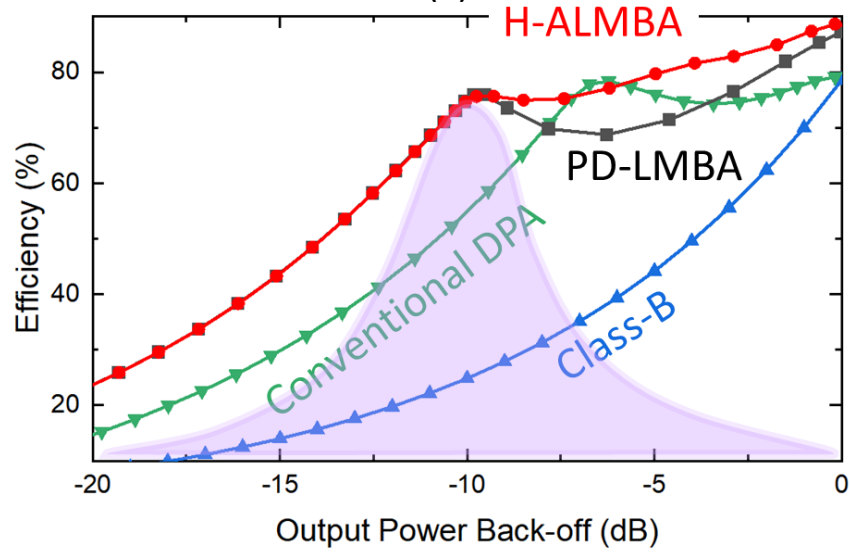
WITH the rapid development of wireless ecosystem and advent of numerous emerging applications, the communications systems are demanded for supporting ever-growing data rates and user capacity. As a result, efficient use of spectrum resources has been a major priority for wireless network, which has triggered the wideband and complexly modulated communication signals with increasingly higher PAPR. This, however, causes a dramatic degradation of average efficiency of PA, since it has to operate in significant power back-off most of the time. On the other hand, due to the rapid 4G/5G band proliferation, more and more spectrum fragments are being incorporated into wireless communications. In order to accommodate the ever-increasing number of allocated frequency bands, the RF bandwidth of power amplifiers and transmitters need to be as wideband as possible for accommodating multi-band communications without suffering from non-affordable hardware complexity, size, and cost. Therefore, developing broadband power amplifiers with enhanced back-off efficiency and high average efficiency has become an important proposition of this era.

Load modulation (LM) is one of the most compelling PA efficiency enhancement technologies. As a representative practical example, DPA has been widely employed in contemporary wireless communication infrastructures such as base stations due to its simplified topology and capability of effectively boosting back-off efficiency. However, the conventional DPA only offers a 6-dB OBO range, and the bandwidth is strongly limited by the quarter-wave inverters embedded in its generic circuit schematic. The extension of DPA bandwidth and OBO range has been intensively studied recently with substantial progresses, such as broadband asymmetric DPAs and multi-way DPAs [60, 61, 17, 21, 22, 35, 62, 58, 63, 64, 65]. Nevertheless, it is still very challenging to incorporate wideband matching techniques and high-efficiency PA modes (e.g., continuous Class-F/ $F^{-1}$  [66, 47]) into the Doherty design and meanwhile accurately control the load modulation, which prevents DPA from achieving the highest possible efficiency over a wide bandwidth. Another representative load-modulation PA, reverse-load-modulated dual branch (RMDB) PA [67, 68], has been proposed and demonstrated in recent years. However, RMDB PA is mostly used in MMIC implementation, and its peak and back-off efficiency still have certain gaps compared to DPA.

Recently, load modulated balanced amplifier (LMBA) has been proposed as a new high efficiency LM PA architecture [23, 41, 24, 25, 26, 27, 28, 69, 70, 71, 72]. It consists of a quadrature BA and a CA with properly correlated amplitude and phase. This LMBA can be further designed with a Doherty type of biasing scheme with BA as carrier and CA as peaking, or vice versa. As presented in [31, 55], we for the first time discovered that by setting the CA as carrier and BA as the peaking, a Doherty-like efficiency enhancement can be achieved with extended dynamic range and nearly unlimited bandwidth. This new mode is named PD-LMBA in [55, 59] or sequential LMBA in [56]. However, it is important to point out that the PD-LMBA as well as many of the variants of LMBA are technically a two-way modulation. With the increasing dynamic range of active load modulation, an undesired efficiency drop in the middle of the back-off levels becomes inevitable.[25, 56, 28, 73] To address this issue, this paper proposes a new high-order



(a)



(b)

Figure 4.1: H-ALMBA overview: (a) schematic and (b) simulated efficiency profile comparison between Class-B amplifier, conventional DPA, PD-LMBA, and H-ALMBA (simulation is based on bare-die GaN devices to emulate the ideal transistor models).

load-modulation platform based on the generic principle of asymmetrical LMBA (ALMBA) [69], and this new architecture is named hybrid ALMBA (H-ALMBA) [70]. The thresholds of the two transistors in the balanced amplifier are separated in this architecture, so that BA1 and BA2 are turned on sequentially, which can achieve three efficiency peaks throughout a larger OBO range. Meanwhile, the efficiency at the intermediate OBO level could be significantly enhanced. Compared with the three-way DPA with a general difficulty for wideband design, H-ALMBA perfectly inherits the wideband nature of PD-LMBA, since the same phase control condition is maintained.

Based upon the preliminary study in [70], the comprehensive theoretical derivation and analysis of H-ALMBA mode are presented in this paper for the first time. Moreover, we discovered that the continuous-mode matching with wideband harmonic tuning can be incorporated into the carrier amplifier (CA) design, and therefore, a high efficiency close to the theoretical limit of practical semiconductor devices can be achieved across the entire dynamic range with the cooperation of two peaking amplifiers (BA1 and BA2). Furthermore, a reciprocal biasing scheme with exchangeable turning-on sequence of peaking devices is proposed and adopted to maintain the optimal three-way load modulation behavior over the entire frequency range. The proposed theory, architecture, and design methodology are well validated with a practical prototype developed using GaN transistors and a wideband three-section branch-line quadrature hybrid as the output combiner.

## 4.2 Hybrid Asymmetrical LMBA Theory

The concept of H-ALMBA is developed from the recently reported LMBA [23, 55, 69], and it consists of three PAs, including a CA biased in Class-AB mode, BA1 in Class-C mode, and BA2 in deep Class-C mode, as shown in Fig. 4.1(a). All PAs are connected to a 3-dB quadrature coupler with a port impedance of  $Z_0$ . The CA functions as the carrier amplifier, while BA1 and BA2 turn on sequentially at different OBO levels. When BA1 is turned on at low-back-off (LBO) level with

BA2 remained off, CA and BA1 form a DPA-like PA. When BA2 is turned on at high-back-off (HBO) level, three PAs cooperate like the LMBA but with BA1 and BA2 asymmetrical [69]. The load modulation of three amplifiers are different at different back-off ranges, which is similar to a three-way DPA. Therefore, multiple efficiency peaks can be formed across the extended dynamic power range, as plotted in red curve of Fig. 4.1(b), leading to a higher average efficiency when amplifying high-PAPR signals.

#### 4.2.1 Generic Quadrature-Coupled Load Modulation

In the analytical modeling of H-ALMBA, all PAs are regarded as ideal voltage-controlled current sources, and they are coupled to the three ports of a 3-dB quadrature hybrid with the forth port connected to a load, as shown in Fig. 4.2. The voltages and currents of all four ports are dependent through the Z-matrix of quadrature coupler, expressed as

$$\begin{bmatrix} V_1 \\ V_2 \\ V_3 \\ V_4 \end{bmatrix} = Z_0 \begin{bmatrix} 0 & 0 & +j & -j\sqrt{2} \\ 0 & 0 & -j\sqrt{2} & +j \\ +j & -j\sqrt{2} & 0 & 0 \\ -j\sqrt{2} & +j & 0 & 0 \end{bmatrix} \begin{bmatrix} I_1 \\ I_2 \\ I_3 \\ I_4 \end{bmatrix} \quad (4.1)$$

where  $V_1 = -I_1 Z_0$ ,  $I_2 = I_{b1}$  and  $I_4 = -jI_{b2}$  representing the input RF currents from BA1 and BA2, while  $I_3 = jI_c e^{j\phi}$  denotes the CA current that is phase-shifted from BA1 by  $\pi/2 + \phi$  [23]. Using the matrix operation in (4.1), the impedances of BA1, BA2 and CA can be calculated as

$$Z_{b1} = Z_0 \left( \frac{I_{b2}}{I_{b1}} + \frac{\sqrt{2}I_c e^{j\phi}}{I_{b1}} \right); \quad (4.2)$$

$$Z_{b2} = Z_0 \left( 2 - \frac{I_{b1}}{I_{b2}} + \frac{\sqrt{2}I_c e^{j\phi}}{I_{b2}} \right); \quad (4.3)$$

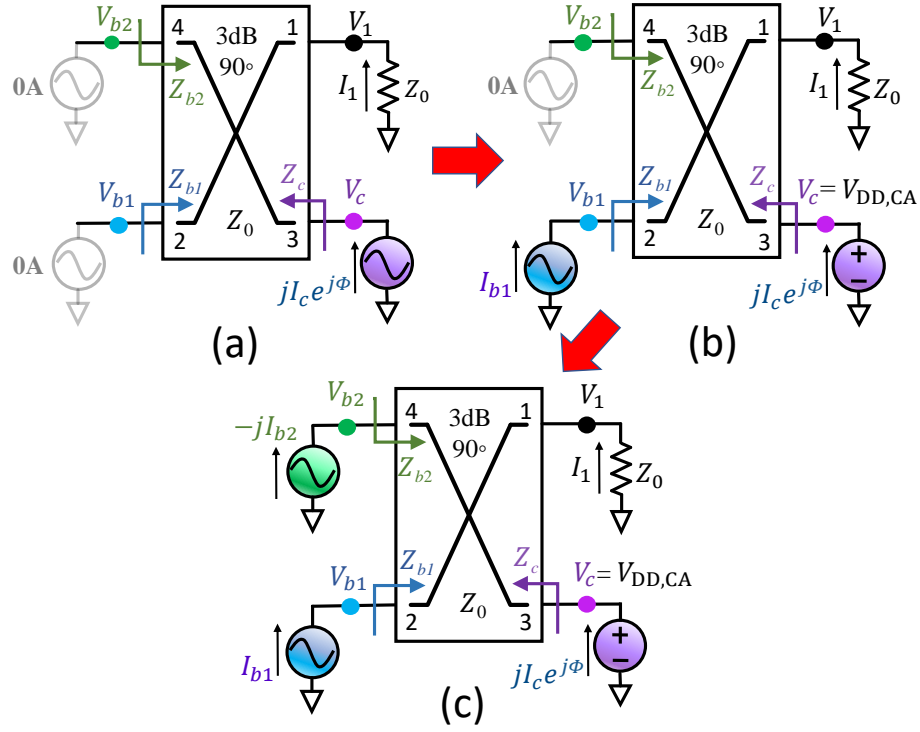


Figure 4.2: Generalized schematic of quadrature-coupled three-way load modulation (H-ALMBA): (a) low-power region (CA only), (b) Doherty region (CA+BA1), (c) ALMBA region (CA+BA1+BA2).

$$Z_c = Z_0 \left( 1 - \sqrt{2} \frac{I_{b1} - I_{b2}}{I_c e^{j\Phi}} \right). \quad (4.4)$$

Eqs. (4.2)-(4.4) indicate the generic quadrature-coupled load-modulation behavior[69, 70], which inclusively explains the original LMBA [23] and all its variants, e.g., [41, 30, 55, 56, 72]. Note that the load modulation of  $Z_{b1}$  and  $Z_{b2}$  can be controlled by the change of  $I_c$  amplitude and phase. At the same time, the load of carrier amplifier,  $Z_c$ , is determined by the difference between  $I_{b1}$  and  $I_{b2}$ . For standard ALMBA [69], the asymmetry between  $I_{b1}$  and  $I_{b2}$  is realized using different supply voltages ( $V_{DD,BA1}$ ,  $V_{DD,BA2}$ ), in order to control the load modulation of CA. In contrast, H-ALMBA leverages different turn-on thresholds of BA1 and BA2 ( $V_{GS,BA1}$ ,  $V_{GS,BA2}$ ), which can not only adjust  $I_{b1}$  and  $I_{b2}$  at different OBO levels but also form a three-way load modulation.

#### 4.2.2 Modeling of Carrier and Peaking Generators

With different gate-bias settings of CA, BA1 and BA2, the dynamic operation of H-ALMBA can be divided into **Low-Power** (CA only), **Doherty** (CA+BA1), and **ALMBA** (CA+BA1+BA2) regions, illustrated in Figs. 4.2(a)-(c), respectively. To analyze the detailed load-modulation characteristics of H-ALMBA, the currents of all three amplifiers are carefully modeled [56].

As the carrier amplifier, the CA current,  $i_{ca}$ , is defined as

$$i_{ca}(\beta) = \begin{cases} i_{ca,lp}(\beta), & 0 \leq \beta < \beta_{lbo} \\ i_{ca,hp}(\beta), & \beta_{lbo} \leq \beta \leq 1 \end{cases} \quad (4.5)$$

where  $i_{ca,lp}$  is the CA current at low power region where the BA1 and BA2 are not turned on, and  $i_{ca,hp}$  denotes the CA current at high power region, including both Doherty and ALMBA regions.  $\beta$  is a normalized variable to describe the magnitude of the input driving level, and  $\beta_{lbo}$  is the BA1 threshold between the low-power region and DPA region.  $i_{ca,lp}$  can be simply expressed using the piece-wise linear model of standard Class-B mode:

$$i_{ca,lp}(\beta) = \begin{cases} \beta I_{Max,C} \cdot \cos\theta, & -\frac{\pi}{2} \leq \theta < \frac{\pi}{2} \\ 0, & \text{otherwise} \end{cases} \quad (4.6)$$

where  $I_{Max,C}$  represents the maximum current allowed for the power device of CA. Using (4.6), the DC and fundamental components of  $i_{ca,lp}$  can be obtained as

$$\begin{aligned} i_{ca,lp}[0] &= \frac{\beta \cdot I_{Max,C}}{\pi}; \\ i_{ca,lp}[1] &= \frac{\beta \cdot I_{Max,C}}{2}. \end{aligned} \quad (4.7)$$

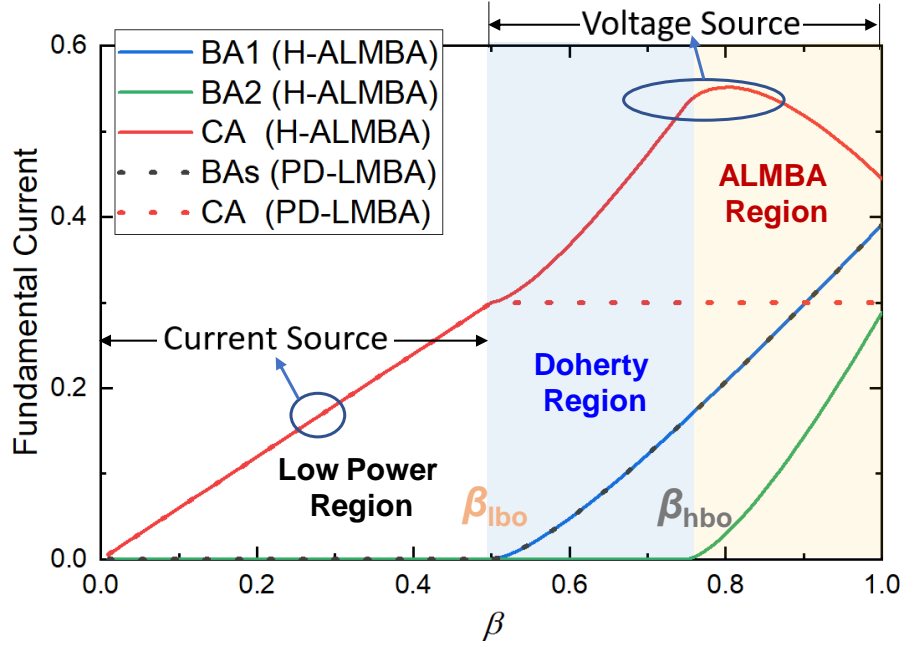


Figure 4.3: Comparison of fundamental currents (normalized to  $I_{\text{Max,C/B}}$ ) of all three amplifiers in H-ALMBA and PD-LMBA modes.

When the driving power increases to  $\beta_{lbo}$ , the CA must be saturated corresponding to the first efficiency peak at the target LBO level. For symmetrical PD-LMBA [31, 55],  $i_{ca,lp}$  grows to its maximum value, and this maximum CA current is maintained regardless of the continued increase of driving power towards the maximum input driving level, as the red dotted line plotted in Fig. 4.3. For H-ALMBA, however, only the voltage of CA is saturated at  $\beta_{lbo}$  that still leads to an efficiency peak. As  $\beta$  increases above  $\beta_{lbo}$ , the CA current continues to increase towards full saturation (both voltage and current) at  $\beta = \beta_{hbo}$ , which is the BA2 threshold between the DPA region and ALMBA region, as shown in Fig. 4.3 (red solid line). For  $\beta$  between  $\beta_{hbo}$  and 1, the CA current can be subject to a decrease because the load impedance increases as BA2 turns on, indicated by (4.4), but the contribution of CA is overwhelmed by the two peaking amplifiers in this region. Nevertheless, it should be emphasized that the CA remains voltage-saturated offering a maximal efficiency across Doherty and ALMBA regions, and thus, in the high-power region, the modeling



of CA is converted from a voltage-controlled current-source to an independent voltage source, which is no longer affected by the input voltage, as shown in Fig. 4.4. With a constant voltage saturation, the CA current can be expressed as

$$i_{ca, hp}(\beta) = \begin{cases} \frac{2V_{DD, CA}}{Z_c(\beta)} \cdot \cos \theta, & -\frac{\pi}{2} \leq \theta < \frac{\pi}{2} \\ 0, & \text{otherwise} \end{cases} \quad (4.8)$$

where  $V_{DD, CA}$  equals to the maximum fundamental voltage of CA, and  $Z_c$  is the load impedance of CA that can be calculated from (4.4). As a voltage source, the CA fundamental voltage maintains a constant value of  $V_{DD, CA}$  as the red curve shown in Fig. 4.4. It is important to note that (4.8) is implicit, since  $Z_c(\beta)$  is also dependent on the fundamental component of  $i_{ca, hp}$  as well as the currents of BA1 and BA2 in the high-power region, as indicated by (4.4). Thus, the CA current and load impedance in (4.8) will be eventually determined together with the BA1 and BA2 models. Particularly, the following boundary condition must be satisfied:

$$i_{ca, lp}(\beta_{lbo}) = i_{ca, hp}(\beta_{lbo}) \quad (4.9)$$

BA1 and BA2 are biased at Class-C mode with different thresholds. BA1 is turned on at  $\beta_{lbo}$ , while BA2 is turned on at  $\beta_{hbo}$ . The currents of BA1 and BA2 can be derived as

$$i_{ba1}(\beta) = \begin{cases} 0, & 0 \leq \beta < \beta_{lbo} \\ i_{ba1, hp}(\beta), & \beta_{lbo} \leq \beta \leq 1 \end{cases} \quad (4.10)$$

$$i_{ba2}(\beta) = \begin{cases} 0, & 0 \leq \beta < \beta_{hbo} \\ i_{ba2, hp}(\beta), & \beta_{hbo} \leq \beta \leq 1 \end{cases} \quad (4.11)$$

It should be noted that the peaking amplifier with full Class-C model is more precise and closer to

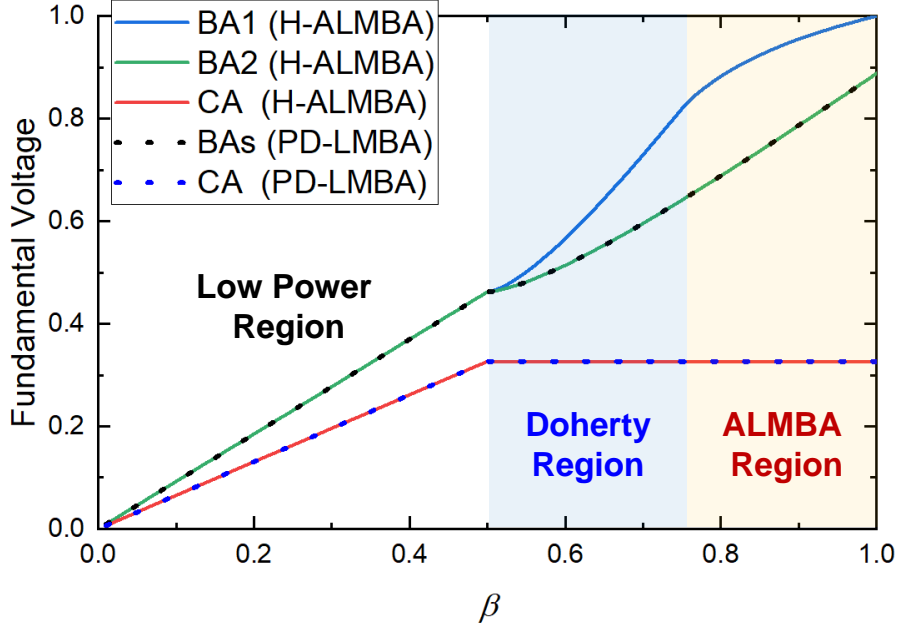


Figure 4.4: Comparison of normalized fundamental voltages of each path in H-ALMBA and PD-LMBA mode.

realistic case, and most of the published LMBA articles adopt this method, e.g., [74, 54]. Therefore, the BA1 current in Doherty and ALMBA region can be expressed using Class-C current formula as

$$i_{ba1, hp}(\beta) = \begin{cases} \frac{\beta \cdot \cos \theta - \beta_{lbo}}{1 - \beta_{lbo}} I_{Max, B}, & -\theta_b \leq \theta < \theta_b \\ 0, & \text{otherwise} \end{cases} \quad (4.12)$$

$I_{Max, B}$  represents the maximum current provided by the peaking device, which is assumed identical for BA1 and BA2. With a different turning-on threshold, the BA2 current in ALMBA region can also be expressed using Class-C current formula as

$$i_{ba2, hp}(\beta) = \begin{cases} \frac{\beta \cdot \cos \theta - \beta_{hbo}}{1 - \beta_{hbo}} I_{Max, B}, & -\theta_b \leq \theta < \theta_b \\ 0, & \text{otherwise} \end{cases} \quad (4.13)$$

where  $(-\theta_b, +\theta_b)$  defines the turn-on phase range of BA1 and BA2. Thus,  $\theta_b$  is obtained as

$$\theta_b = \arccos(\beta_{bo}/\beta). \quad (4.14)$$

By applying Fourier Transformation, the DC and fundamental currents of BA1 and BA2 can be calculated as

$$\begin{aligned} i_{ba1, hp}[0] &= \frac{I_{Max,B}}{1 - \beta_{lbo}} \cdot \frac{\beta \sin \theta_b - \beta_{lbo} \theta_b}{\pi}; \\ i_{ba1, hp}[1] &= \frac{I_{Max,B}}{1 - \beta_{lbo}} \cdot \frac{\beta(2\theta_b + \sin 2\theta_b) - 4\beta_{lbo} \sin \theta_b}{2\pi}. \end{aligned} \quad (4.15)$$

$$\begin{aligned} i_{ba2, hp}[0] &= \frac{I_{Max,B}}{1 - \beta_{hbo}} \cdot \frac{\beta \sin \theta_b - \beta_{hbo} \theta_b}{\pi}; \\ i_{ba2, hp}[1] &= \frac{I_{Max,B}}{1 - \beta_{hbo}} \cdot \frac{\beta(2\theta_b + \sin 2\theta_b) - 4\beta_{hbo} \sin \theta_b}{2\pi}. \end{aligned} \quad (4.16)$$

Fig. 4.3 shows the normalized fundamental current of the BA1 and BA2 versus  $\beta$  with  $\beta_{lbo} = 0.5$  and  $\beta_{hbo} = 0.75$ , respectively, and Fig. 4.4 depicts the corresponding voltages of BA1 and BA2. It is interesting to note that the voltage of individual BA in PD-LMBA ( $\beta_{PD-LMBA} = 0.5$ ) is the same as that of BA2 in H-ALMBA.

#### 4.2.3 Load Modulation Analysis of H-ALMBA

The detailed analysis on load-modulation behavior of H-ALMBA is performed for all three different regions:

- **Low-Power Region** ( $P_{OUT} < P_{MAX}/LBO$ ): When operating at low power level below the predefined target LBO power, the BA1 and BA2 are not turned on, as depicted in Fig. 4.2(a).

The CA operates as a standalone Class-B amplifier, and the output power is solely generated by CA. In this low-power region, there is no load modulation for all three amplifiers, and the currents are provided as following

$$\begin{aligned} I_c &= i_{ca,lp}[1]; \\ I_{b1} &= I_{b2} = 0. \end{aligned} \quad (4.17)$$

Their load impedances,  $Z_{c,LP}$ ,  $Z_{b1,LP}$ , and  $Z_{b2,LP}$ , can be expressed as

$$\begin{aligned} Z_{c,LP} &= Z_0; \\ Z_{b1,LP} &= Z_{b2,LP} = \infty. \end{aligned} \quad (4.18)$$

Since BA1 and BA2 (BAs) are not operating, the overall efficiency of H-ALMBA is equal to the efficiency of CA.

- **Doherty Region** ( $P_{MAX}/LBO \leq P_{OUT} < P_{MAX}/HBO$ ): When the output power increases to the target LBO level, BA1 is turned on, and CA reaches saturation at the same time. At  $P_{MAX}/LBO$ , CA is designed to be only voltage-saturated ( $Z_c > Z_{CA,Opt}$ ) corresponding to the first efficiency peak, while there is still headroom for further increase of CA current. In this region, BA1 and CA currents both increases, given by

$$\begin{aligned} I_c &= i_{ca,hp}[1] = V_{DD,CA}/Z_c; \\ I_{b1} &= i_{ba1,hp}[1]; \quad I_{b2} = 0. \end{aligned} \quad (4.19)$$

By substituting the above currents into (4.2)-(4.4), and when  $\phi = 0^\circ$ , the load modulation

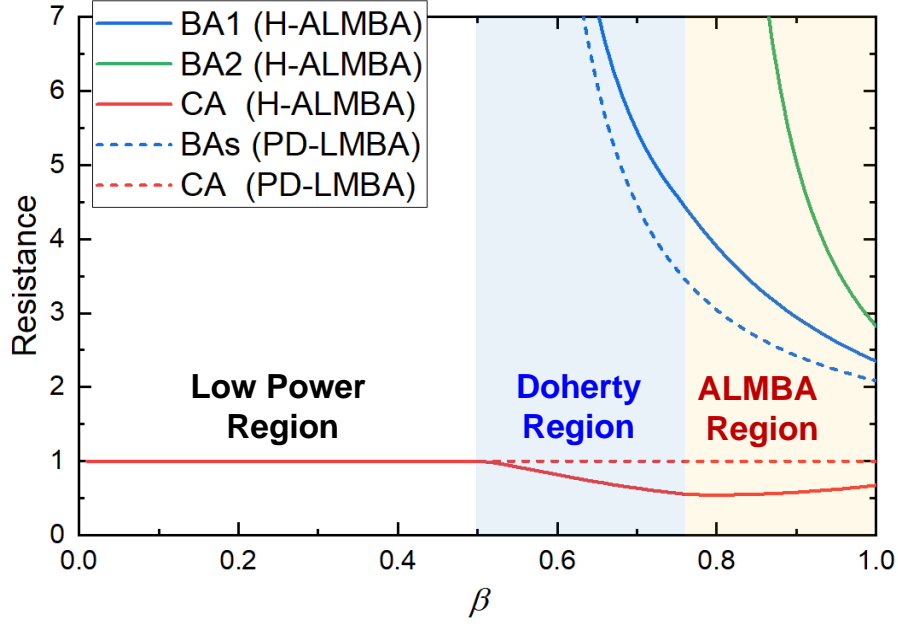


Figure 4.5: Comparison of resistances of each path in H-ALMBA and PD-LMBA mode.

behaviors of CA, BA1, and BA2 impedances are derived as

$$\begin{aligned}
 Z_{c,\text{Doherty}} &= \frac{Z_0 V_{DD,CA}}{V_{DD,CA} + \sqrt{2} I_{b1} Z_0} \big|_{\phi=0^\circ}; \\
 Z_{b1,\text{Doherty}} &= 2Z_0 + \frac{\sqrt{2} V_{DD,CA}}{I_{b1}} \big|_{\phi=0^\circ}; \\
 Z_{b2,\text{Doherty}} &= \infty.
 \end{aligned} \tag{4.20}$$

The above equation clearly shows that as the power increases to the Doherty region,  $Z_c$  can be modulated below  $Z_0$ . Since the CA voltage remains constant ( $= V_{DD,CA}$ ) at this time, the current ( $I_c$ ) and output power of CA can continue to increase.

- **ALMBA Region** ( $P_{\text{MAX}}/\text{HBO} \leq P_{\text{OUT}} < P_{\text{MAX}}$ ): When the driving power reaches  $\beta_{\text{hbo}}$ , BA2 is turned on, and the PA load modulation follows the ALMBA mode. Therefore, the

currents of all three amplifiers can be expressed as

$$\begin{aligned} I_c &= i_{ca, hp}[1] = V_{DD, CA}/Z_c; \\ I_{b1} &= i_{ba1, hp}[1]; \quad I_{b2} = i_{ba2, hp}[1]. \end{aligned} \quad (4.21)$$

The load impedances of CA, BA1, and BA2 are can be described using (2)-(4), and when  $\phi = 0^\circ$ , the impedance equations can be further derived as:

$$\begin{aligned} Z_{c, ALMBA} &= \frac{Z_0 V_{DD, CA}}{V_{DD, CA} + \sqrt{2}(I_{b1} - I_{b2})Z_0} \Big|_{\phi=0^\circ}; \\ Z_{b1, ALMBA} &= 2Z_0 + \frac{\sqrt{2}V_{DD, CA} - Z_0 I_{b2}}{I_{b1}} \Big|_{\phi=0^\circ}; \\ Z_{b2, ALMBA} &= \frac{Z_0 I_{b1} + \sqrt{2}V_{DD, CA}}{I_{b2}} \Big|_{\phi=0^\circ}. \end{aligned} \quad (4.22)$$

It could be observed from Fig. 4.3 that the fundamental current of BA2 increases more sharply as compared to the current of BA1. Thus, when the driving level ( $\beta$ ) reaches to maximum, the BA1, BA2, and CA are all saturated respectively, and an maximum DE can be obtained.

Based on the above comprehensive load-modulation analysis, the load impedance and current of CA can be analytically determined using (4.4) and (4.8). The red curves (solid and dotted lines) in Fig. 4.5 compare the CA load modulation trajectories with  $\phi = 0^\circ$  between symmetrical PD-LMBA and H-ALMBA in different regions. Correspondingly, the overall fundamental CA current ( $I_c$ ) versus driving level is plotted as the red curve in Fig. 4.3. The load modulation behaviors of BA1 and BA2 in H-ALMBA are calculated using (4.2)-(4.3), which are plotted in Fig. 4.5 in

comparison with PD-LMBA. The normalized fundamental voltages of different amplifier branches in H-ALMBA and PD-LMBA modes are shown in Fig. 4.4.

With the derived load modulation behaviors in terms of current, voltage, and impedance, the overall efficiency responses of PD-LMBA and H-ALMBA across the entire dynamic range are obtained and plotted as solid lines in Figs. 4.6(a) and (b), respectively, which also show the efficiencies of individual BA and CA. It can be seen that, in Doherty region ( $\beta$  from 0.5 to 0.75) with BA2 turned off, the BA efficiency of H-ALMBA increases more sharply than that of PD-LMBA. Therefore, an extra peak efficiency can be formed at the end of Doherty region (HBO level), which greatly improves the overall efficiency of the entire back-off range. Note that the efficiency at peak power is higher than 78.5% because of the Class-C operation of peaking amplifiers.

#### 4.2.4 Amplitude and Phase Control of H-ALMBA

The amplitude control of H-ALMBA involves the power ratio of all three amplifiers and the turn-on points of BA1 and BA2. In this H-ALMBA operation, BA1 needs to be turned on at a pre-determined OBO level. By sweeping the turning on time of BA2,  $\beta_{\text{hbo}}$ , the optimal DE of the entire back-off region can be determined. The efficiency profiles with different  $\beta_{\text{hbo}}$  are shown in Fig. 4.7. It can be seen that the highest overall efficiency could be achieved with  $\beta_{\text{hbo}}$  between 0.7 and 0.8, which is close to half of the entire back-off region.

In addition to amplitude control, it is necessary to ensure that the phase difference between the power generators is properly set to result in optimal load modulation trajectories of each amplifier. As described in (4.20), by setting  $\phi = 0^\circ$ , a purely resistive load modulation of  $Z_{b1}$ ,  $Z_{b2}$ ,  $Z_c$  can be achieved, which represent the optimal LM behaviors according to the classical load-line theory [38]. In realistic designs with matching networks and parasitics of transistors, the optimal BA-CA phase offset will be determined through exhaustive sweeping in the actual circuit schematic.

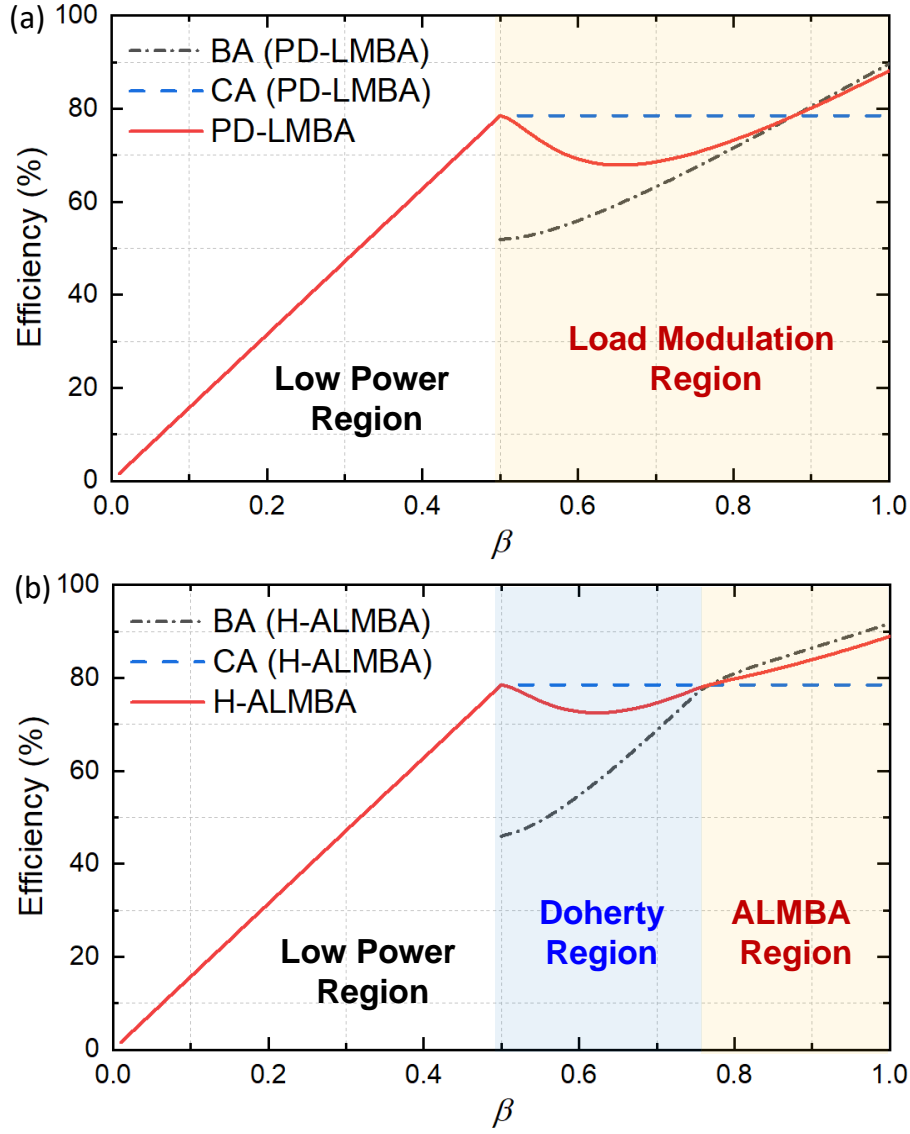


Figure 4.6: Carrier and peaking efficiency performances: a) PD-LMBA; b) proposed H-ALMBA.

Moreover, compared to other load modulation architectures, H-ALMBA is easier to achieve different OBO levels by properly selecting the turning-on points of BA1 and BA2. The value of  $\beta_{lbo}$  not only represents the turning on point of BA1, but it also affects the selection of CA drain voltage, which can be utilized to ensure a voltage saturation of CA at the target OBO. The  $\beta_{hbo}$  denotes the turning on of BA2, which can be leveraged to optimize the overall back-off efficiency for different



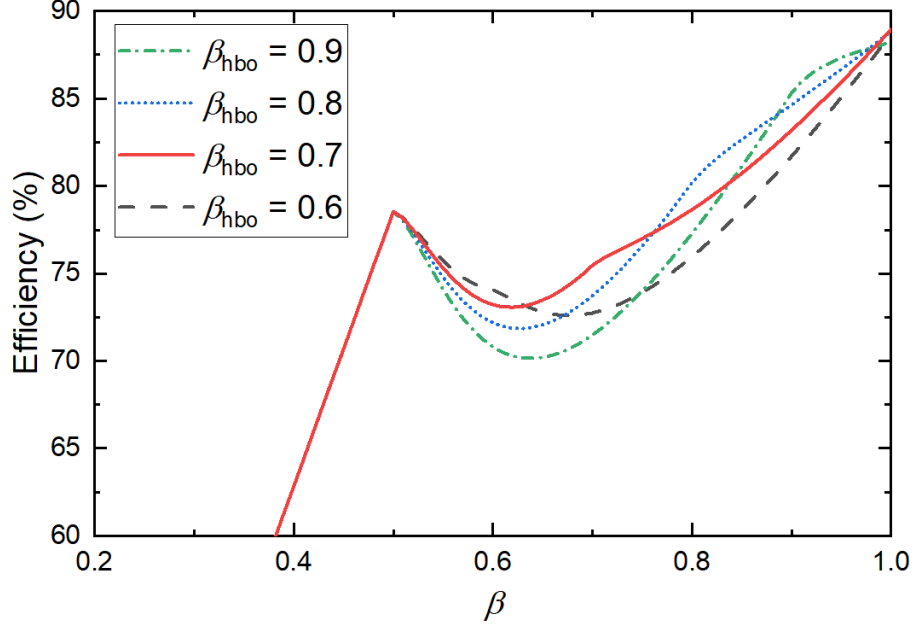


Figure 4.7: Efficiency performance of the proposed H-ALMBA versus  $\beta$  with  $\beta_{lbo} = 0.5$  and different values of  $\beta_{hbo}$ .

OBO levels. Fig. 4.8 shows the efficiency performance of the proposed H-ALMBA with different  $\beta_{lbo}$  and  $\beta_{hbo}$ . Within the range from 0.6 to 0.2 of  $\beta_{lbo}$  and corresponding  $\beta_{hbo}$  from 0.75 to 0.45, the power back-off range of H-ALMBA could be extended from 7 dB to 17 dB with the highest possible back-off efficiency. The gain (AM-AM) profiles with different  $\beta_{lbo}$  and  $\beta_{hbo}$  are shown in Fig. 4.9. It can be seen that with the increase of the OBO range, a flatter gain response can be achieved. Overall, the efficiency and gain results indicate that the H-ALMBA mode is very suitable for amplification of high-PAPR signals. It is worth noting in Fig. 4.9 that the change of  $\beta_{hbo}$  does not impact the gain response as long as  $\beta_{lbo}$  is fixed. This shows that even if the output power of CA is backed-off after BA2 is turned on (ALMBA region), it does not compromise the gain and power-added efficiency (PAE) of the overall PA.

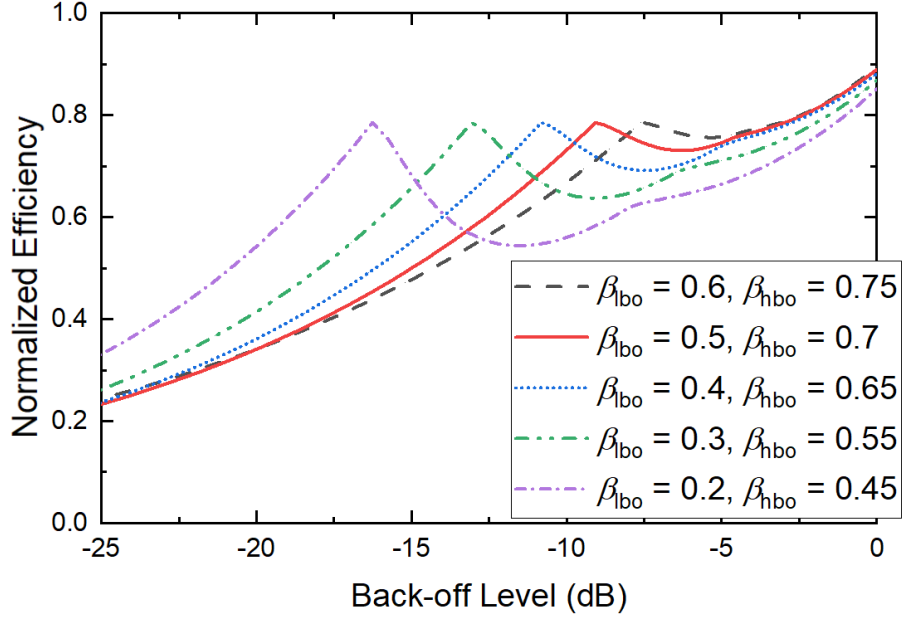


Figure 4.8: Efficiency performance of the proposed H-ALMBA versus back-off level with different  $\beta_{lbo}$  and  $\beta_{hbo}$ .

#### 4.2.5 Efficiency Enhancement of CA: Necessity and Approach

It should be noted that in the low-power region, the BA1 and BA2 are off, and all output power is generated by CA. Therefore, the impedance matching of the CA needs to ensure its wideband efficiency when operating alone, since the CA efficiency sets the first efficiency peak of the power back-off range and the average efficiency of entire PA. In the H-ALMBA architecture [69], CA is biased in Class-AB that has an efficiency naturally lower than that of the Class-B (78.5%). On the other hand, the CA output connects to the PA load through the output quadrature coupler, and the broadband output quadrature coupler itself usually has a certain internal loss. At the same time, when BA1 and BA2 are not turned on, BA1 and BA2 present off-state impedances to the corresponding ports of the output couplers, which can be regarded as two identical  $R$ - $C$  tanks with the same quality factor ( $Q$ ). The  $Q$  of  $R$ - $C$  tank determines the external power loss of quadrature

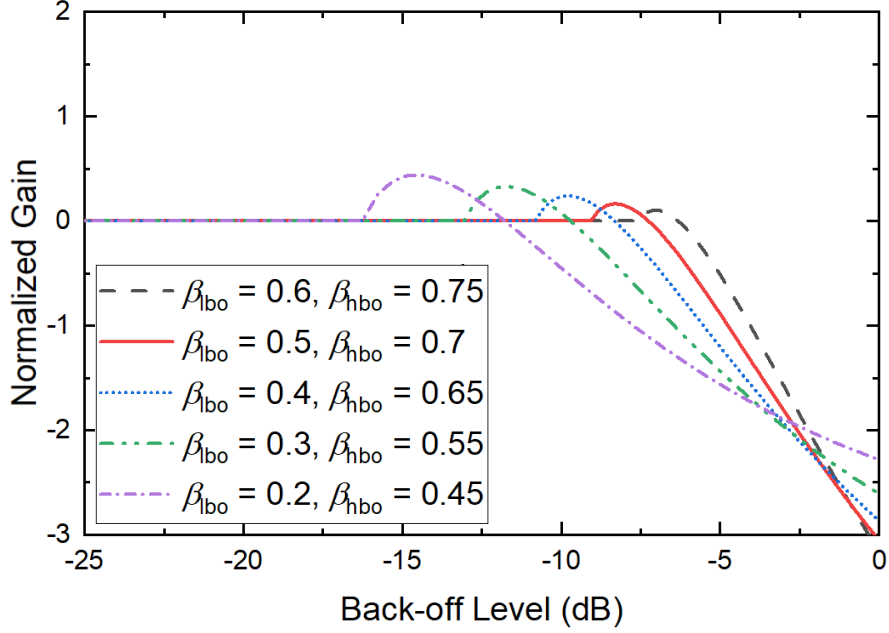


Figure 4.9: Gain performance of the proposed H-ALMBA versus back-off level with different  $\beta_{lbo}$  and  $\beta_{hbo}$ .

coupler, which is added together with the internal loss forming the total insertion loss from CA port to the output, as shown in Fig. 4.10(a). Thus, the overall efficiency of CA in Class-AB mode can be significantly degraded, as the red curve depicted in Fig. 4.10(b).

In order to maximize the peak efficiency of CA, this paper combines the high-efficiency harmonic-tuned matching (e.g., Class-F/ $F^{-1}$  or its extension, continuous Class-F/ $F^{-1}$ ) with H-ALMBA for the first time, and the output impedance matching with continuous mode (CM) is used to realize broadband CA design. Under the same insertion loss, the peak efficiency of the CA designed with continuous Class-F/ $F^{-1}$  (blue curve with circles) can be greatly improved as compared to that with Class-AB, as shown in Fig. 4.10(b) (the quadrature coupler internal loss is assumed to be 0.4 dB). Thus, upgrading CA from Class-AB to continuous Class-F/ $F^{-1}$  can greatly improve the peak efficiency of CA, thereby enhancing the overall PA back-off efficiency.

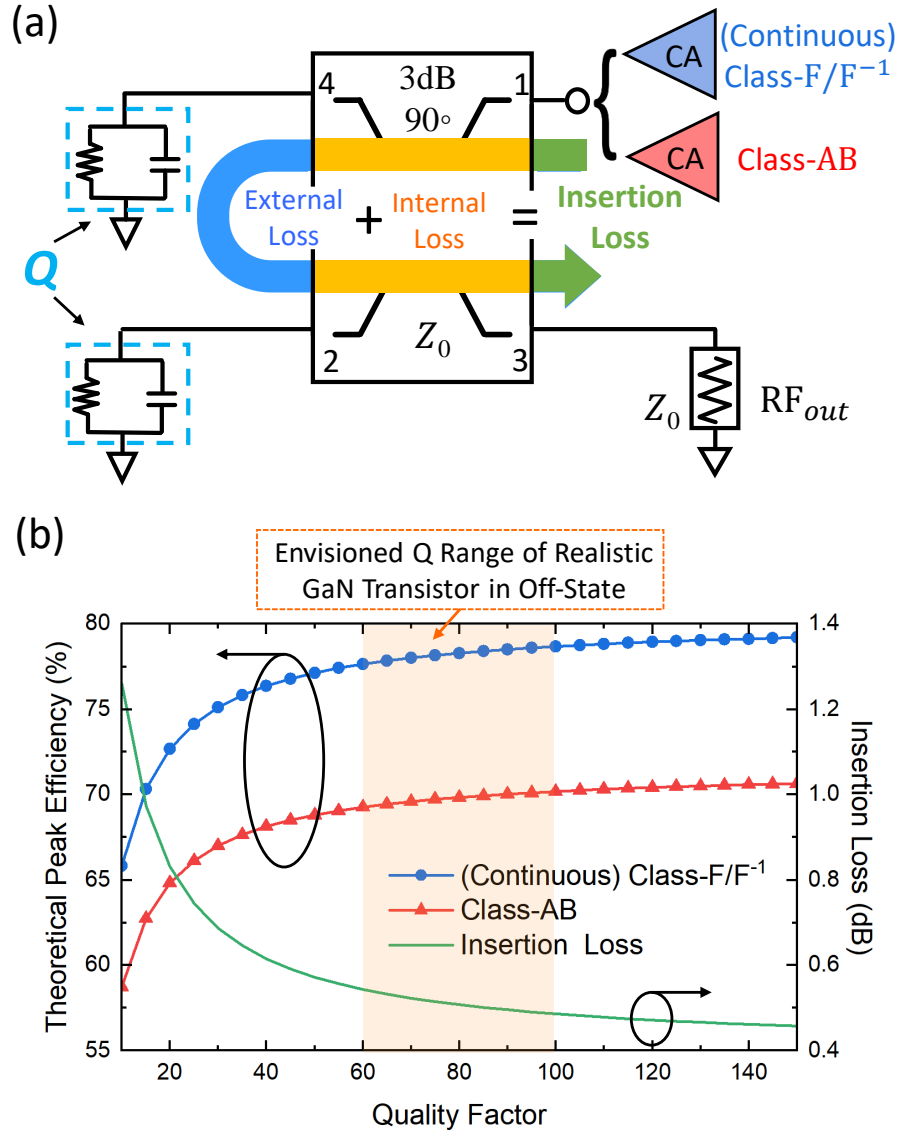


Figure 4.10: Comparison of CA designed with continuous Class-F/F<sup>-1</sup> and Class-AB: (a) schematic diagram; (b) ideal peak efficiency comparison with the same power loss.

#### 4.3 Practical Design of Ultra-Wideband Continuous-Mode H-ALMBA

In order to accommodate the high PAPR of emerging 5G and WiFi6 signals, the back-off range of the proposed H-ALMBA can be up to 17 dB according to actual needs, as shown in Fig. 4.8 and Fig. 4.9. In this design, a back-off range of 10-dB, is selected as a target OBO of this demon-

strated work. The target frequency range is from 1.7 to 3.0 GHz, which could cover most cellular communication frequency bands.

#### 4.3.1 Design of Control Amplifier in Continuous Mode

According to the amplitude control scheme described in Sec. 4, the power of CA at the first efficiency peak determines the dynamic range once the output power of BA is fixed. Given a specific OBO target, the power of CA can be expressed by

$$\text{OBO} \times P_{\text{CA,Sat1}} = P_{\text{BA1,MAX}} + P_{\text{BA2,MAX}} + P_{\text{CA,Sat2}} \quad (4.23)$$

where  $P_{\text{CA,Sat1}}$  represents the CA power at voltage saturation (first peak), and  $P_{\text{CA,Sat2}}$  denotes the final CA power at maximum overall output power. A rough calculation indicates that  $P_{\text{CA,Sat1}}$  is around 9-dB below  $P_{\text{BA1,MAX}} + P_{\text{BA2,MAX}}$ , while the accurate power dependence can be calculated by detailed analytical expressions presented in Sec. 4. To realize this low output power, the CA is implemented with a 10-W GaN transistor (Wolfspeed CG2H40010), and it is biased in Class-AB mode with around 10-V drain bias voltage  $V_{\text{DD,CA}}$ . This value may be adjusted slightly at different frequencies to ensure that the OBO range of each frequency is 10 dB. It should be noted that this article is mainly targeted to verify the proposed H-ALMBA theory. Thus, for the convenience of fabrication, the same transistors are used in both CA and BAs. Since the CA power is much lower than BAs, it is physically realized using a lower  $V_{\text{DD}}$ . In realistic H-ALMBA design in MMIC, a smaller size of transistor can be designed for CA that is biased with the same  $V_{\text{DD}}$  as BAs, in order to avoid under-utilizing the CA device.

In low-power region, the BA1 and BA2 ports of the output coupler are open, and all output power is generated by CA. Therefore, in the actual matching design of the CA, the optimal wideband

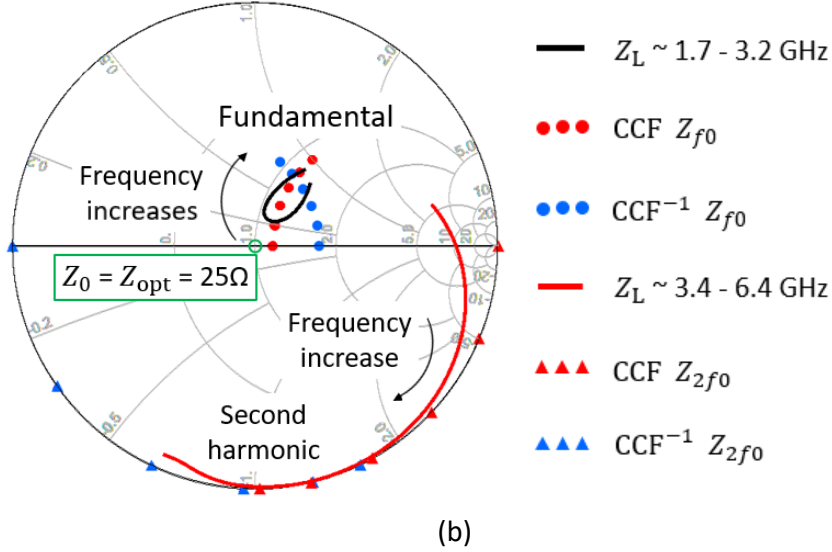
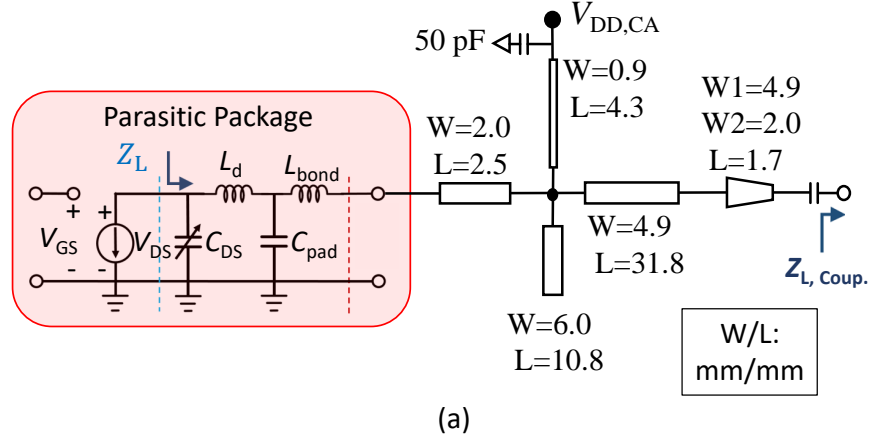


Figure 4.11: OMN design of CA: (a) schematic of the designed CA-OMN with continue-mode; (b) simulated matching results of the designed CA-OMN from 1.7 to 3.0 GHz on the Smith chart with reference impedance.

efficiency of CA standalone is considered, and meanwhile, its load modulation control of BA is also taken into account. However, a dilemma is envisioned: to ensure highest possible efficiency of standalone CA over the entire target bandwidth requires a complex harmonic-tuned wideband matching network, but an excessively complex matching network can cause uncontrollable phase dispersion [23] over frequency, which invalidates the precise phase control of BA. In [70], a simple three-segment transmission line is used as the output matching of the CA to maximize the



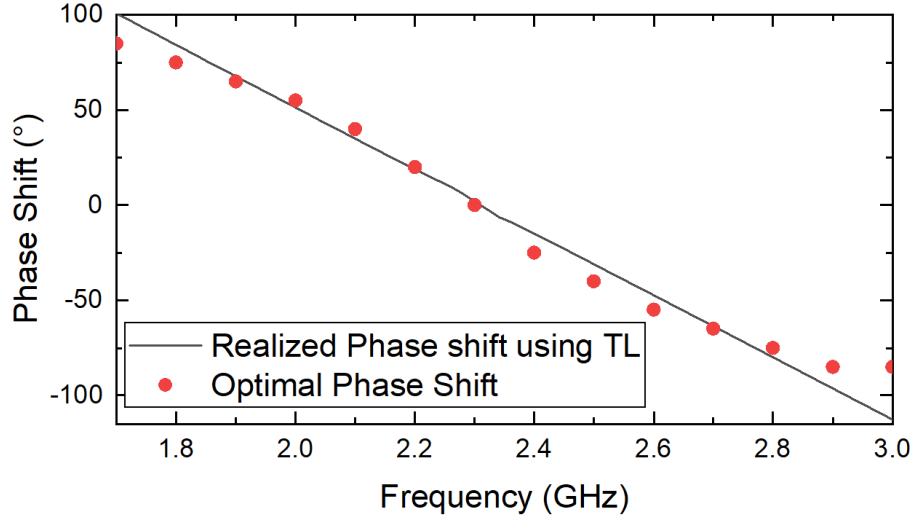


Figure 4.13: Simulated optimal BA1-CA phase offset at different frequencies.

shown in Fig. 4.11(b). Meanwhile, the frequency response of this OMN over the second harmonic frequency range from 3.4 – 6 GHz is distributed to the corresponding second harmonic impedance of the  $CCF^{-1}$  and CCF modes. Thus, a harmonic-tuned CA is realized in a transferring mode between  $CCF^{-1}$  and CCF.

On the other hand, the phase dispersion of this OMN is minimized since only one shunt stage (with a bias line and open-ended stub in parallel) is involved. The phase shift of series stages in the form of transmission lines (TLs) can be perfectly compensated with a phase offset line at BA input [55]. The wideband CA input-matching network (IMN) needs to ensure a decent gain performance within the target bandwidth. Therefore, a two-section lowpass network based on transmission lines is designed to provide wideband input matching for the selected GaN transistor.

#### 4.3.2 Design of Balanced Amplifier with Asymmetrical Gate-Bias Setting

In this design, the two peaking amplifiers, i.e., BA1 and BA2, are designed with identical matching but different gate bias voltages. The input coupler (IPP-7118, available from Innovative Power



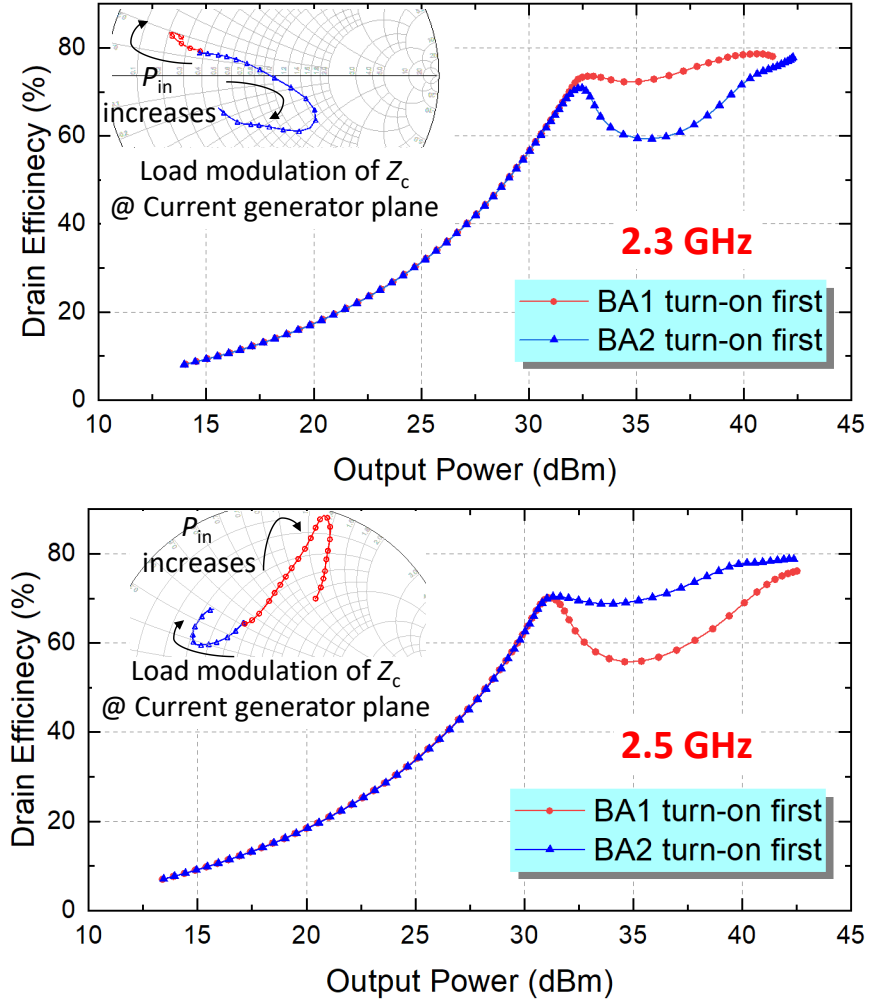


Figure 4.14: Reciprocal turning-on sequence of BA1 and BA2 at different frequencies and its impact on CA load modulation and efficiency profile.

Product [43]) is constructed using commercial equipment with a wide operating bandwidth of 1.7 to 3.0 GHz. The output coupler is realized with a non-50 $\Omega$  three-stage branch hybrid structure, which can provide enough bandwidth to cover the design goal [44]. BA1 and BA2 are implemented with 10-W packaged GaN transistors (CG2H40010). Following the well demonstrated method in [55, 69], the BA output matching is performed using the characteristic impedance of output coupler ( $Z_{0,Coupler}$ ) and bias lines (a shunt  $L$ ). Note that the BA1 and BA2 are in Class-C mode, and their efficiencies are intrinsically higher than that of Class-B. Thus, the simplified matching of BA1

and BA2 suffices the harmonic tuning. It should also be noted that in the H-ALMBA design, load impedances of BA1 and BA2 are determined by the power (amplitude) and phase of CA, as indicated by (4.2) and (4.3). Therefore, the value of  $Z_{0,Coupler}$  ( $= 25 \Omega$  in this design) and the length of the bias lines are finalized through co-simulation with the CA using the simulation setup shown in Fig. 4.12(a).

A four-stage low-pass network is designed and implemented with transmission lines to provide input matching covering the target bandwidth from 1.7 to 3.0 GHz. Each stage consists of a series  $L$  (high impedance TL) and a shunt  $C$  (low impedance open stub). The length and width of TL are adjusted to absorb the parasitic effects of RF and DC modules and device packaging. The design of this matching circuit follows the widely adopted method introduced in [46].

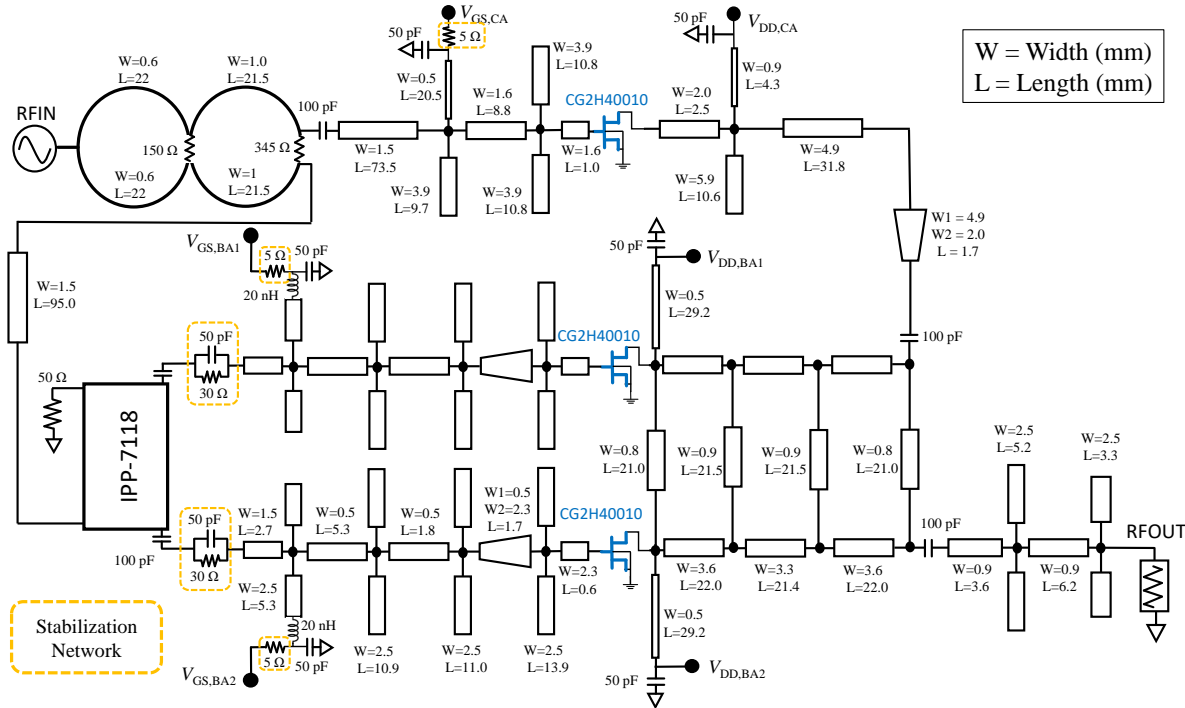


Figure 4.15: Circuit schematic overview of designed CM-H-ALMBA.

#### 4.3.3 Wideband BA-CA Phase Offset Design

The phase difference between BA1 and BA2 is fixed to  $90^\circ$  in a balanced amplifier. Therefore, after combining the complete BA (BA1 and BA2 with input and output couplers) and CA, the load modulation of all three amplifiers are mainly determined by the relative phase between BA and CA. In order to ensure the purely resistive load modulation of three amplifiers for maximized efficiency, a phase-adjustment network between BA and CA is required. Thus, an optimal phase offset is realized at the input of BA and CA, which can be determined using an equal-amplitude dual-input schematic diagram (similar to the method presented in [29]), as plotted in Fig. 4.12(b). By adding an ideal control signal to the isolation port of the output coupler, and scanning a large number of different phase values, the best phase corresponding to each frequency could be found. As shown in the red points of Fig. 4.13, the optimal phase shift between BA and CA is almost linearly proportional to the frequency with a negative slope. Therefore, an input-phase-adjustment network is added at the input side of BA by using a  $50\text{-}\Omega$  TL to suit the frequency-dependent phase-offset requirement [31, 55, 59]. The 'curve-fitting' results are plotted in Fig. 4.13. It can be seen that the realized TL phase shifter offers near-optimum phase setting at different frequencies. It should be noted that if the frequency continues to increase, the phase difference between BA and CA no longer completely comply to linear relationship, which could be due to the limited bandwidth of output quadrature coupler (i.e., three-section branch-line quadrature hybrid) and the phase dispersion of transistor parasitics. To further perfect the phase control over a broadened bandwidth, more precise phase control can be achieved through digital-assisted dual-input in the future designs.

It needs to be pointed out that, under ideal conditions, the CA impedance in the plane of the coupler isolation port should be  $Z_0$  for any in band frequencies. Then, when BA1 is turned on, the CA impedance should be modulated to the lower impedance region, so that the CA output

power can continue to increase, thus boosting the back-off efficiency, as the red curve shown in Fig. 4.14(a). However, due to the inevitable phase/amplitude imbalances of realistic broadband quadrature couplers, the load modulation of CA is affected as well as BA1 and BA2. Therefore, at some frequencies, the ideal turning on sequence does not lead to the desired back-off efficiency enhancement, e.g. 2.5 GHz of this design as the red curve shown in Fig. 4.14(b). Inspired by the reciprocal biasing scheme presented in [63], we can exchange the role of BA1 and BA2 with BA2 turned on first, in order to compensate the imperfections of quadrature coupler. At 2.5 GHz, the reciprocal biasing effectively re-establishes the desired load modulation trajectory and the overall efficiency profile, as shown in the Fig. 4.14(b). With a combination of nominal and reciprocal biasing modes, the three-way load-modulation can be optimized over a wide bandwidth without having to rely on any additional tuning elements. This is a main advantage over the conventional three-way Doherty PA, which is difficult for wideband design.

#### *4.3.4 Overall Schematic and Simulation Results*

The designed final circuit schematic is shown in Fig. 4.15, and the values of all actual circuit elements are displayed next to the symbols. A 5- $\Omega$  resistor is added to the gate bias of each way and a parallel RC tank is added before the input matching network of BA1 and BA2 to ensure the stabilization of the entire PA. Between exchangeable gate biasing of BA1 and BA2 that is frequency-dependent, the first turning-on threshold is set to a gate bias voltage of  $-4.5$  V, and the second one is set to  $-5.5$  V. There are fine adjustments for different frequencies to ensure a LBO of 10-dB and a HBO of 5-dB could be obtained, where the CA load modulation is performed concurrently.

Through the design of the wideband BA1, BA2, CA, and phase shifter described in this section, the theoretical derivation results in section II have been perfectly verified by the simulation results,

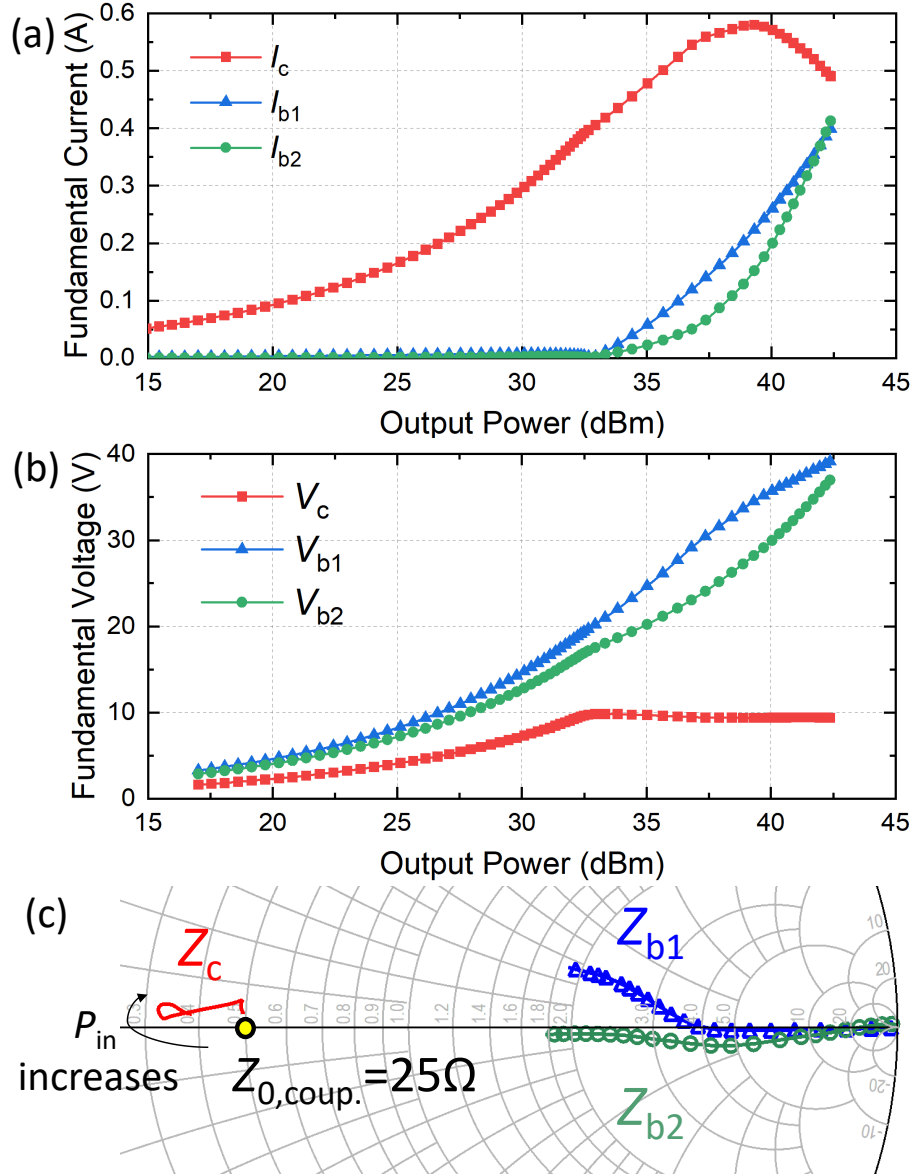


Figure 4.16: Simulation results of the designed H-ALMBA at 2.25 GHz: (a) fundamental current; (b) fundamental voltage; (c) drain plane load trajectory.

which are plotted in Fig. 4.16. Fig. 4.16(a) and (b) shows the simulated fundamental current and voltage at 2.2 GHz, respectively, and Fig. 4.16(c) depicts the load impedance trajectories of all three amplifiers at 2.2 GHz de-embedded to the intrinsic drain plane. The wideband drain efficiency and PAE of the designed H-ALMBA are simulated with swept input power, as shown

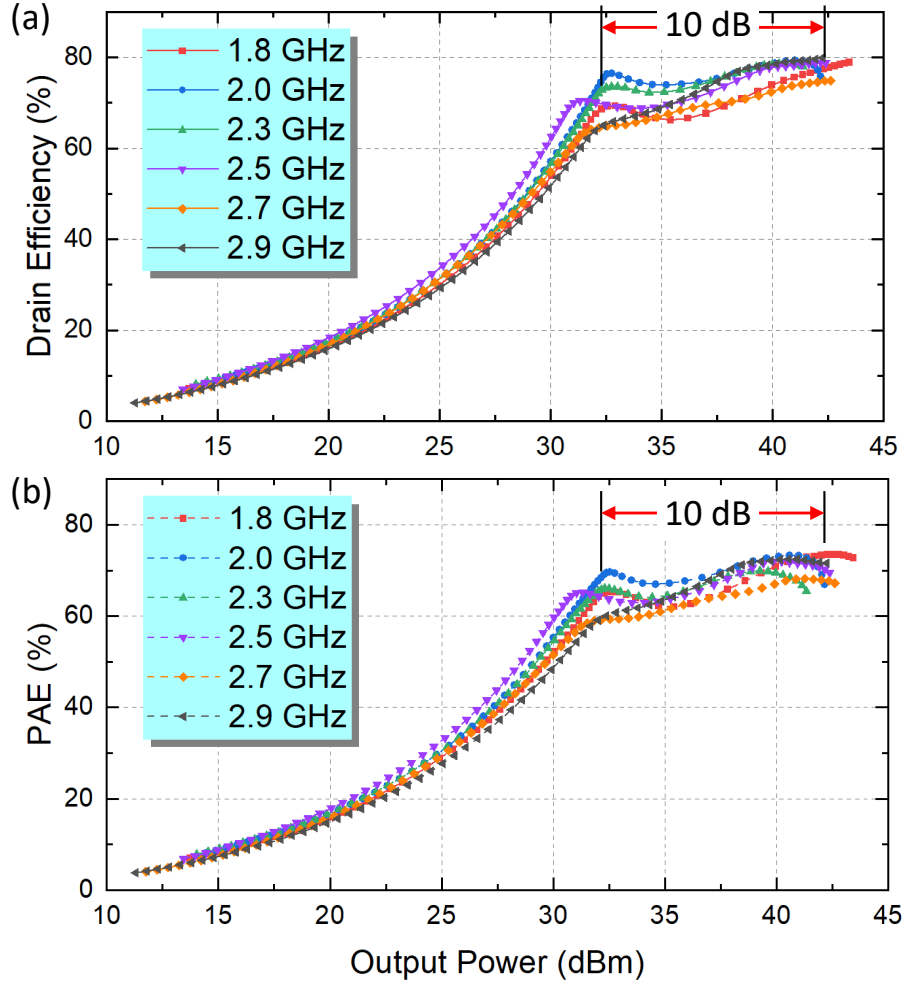


Figure 4.17: Power-swept CW simulation results of the designed H-ALMBA with the best BA-CA phase setting at different frequencies: (a) drain efficiency; (b) PAE.

in Fig. 4.17. It is clearly seen that a high efficiency of  $> 70\%$  is maintained from peak down to 10-dB back-off nearly across the entire frequency range. This is mainly due to the continuous-mode design of CA that ensures a high first efficiency peak and the effectiveness of the proposed H-ALMBA architecture.

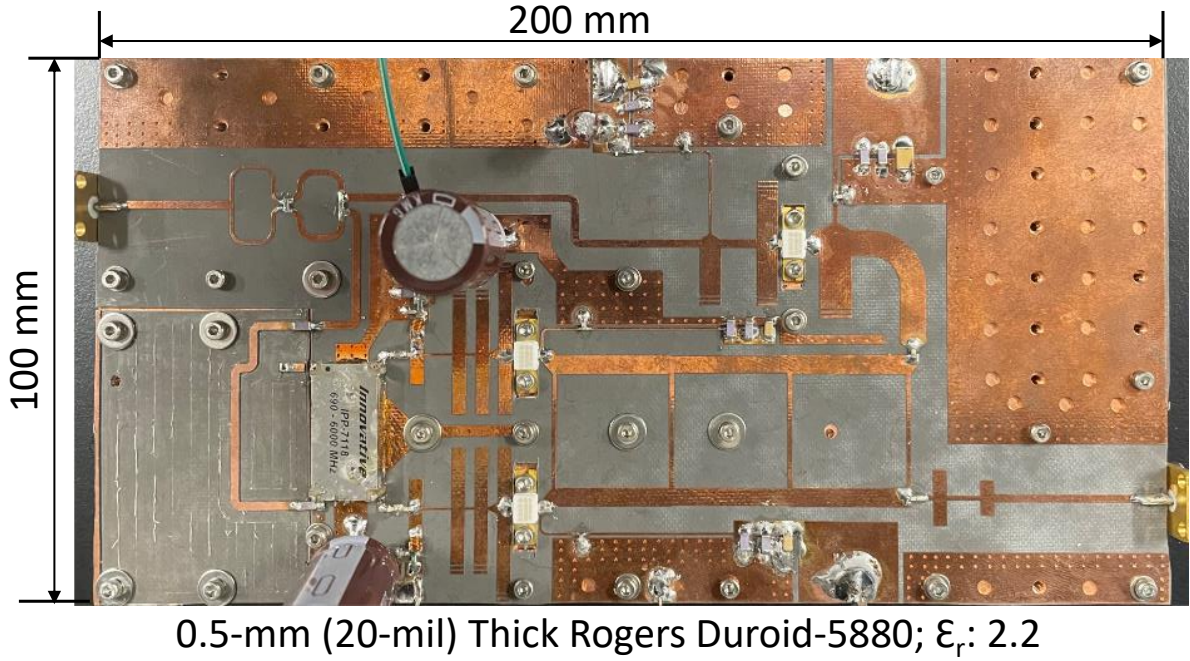


Figure 4.18: Fabricated H-ALMBA prototype.

#### 4.4 Implementation and Experimental Results

The overall layout is generated from circuit schematic, and it is electromagnetically modeled using ADS Momentum simulator. The proposed H-ALMBA is implemented on a 0.5-mm (20-mil) thick Rogers Duroid-5880 PCB board with a dielectric constant of 2.2. A photograph of the fabricated H-ALMBA is shown in Fig. 4.18. The size of the entire circuit is 100 mm  $\times$  200 mm. The fabricated H-ALMBA is measured using both continuous-wave (CW) and modulated LTE signals. In this implemented circuit, the BA1 and BA2 are biased in Class-C with same 28-V  $V_{DD}$ . Based on different frequency, CA is biased in Class-AB with a  $V_{DD,CA}$  range from 10 V to 13 V, which ensures CA saturation at 10-dB power back-off at all frequencies. The opening sequence of BA1 and BA2 is controlled by setting different  $V_{GS}$  bias voltages. The first opened BA  $V_{GS}$  is set at around  $-4.5$  V, and the later opened BA  $V_{GS}$  is set at about  $-5.5$  V. The value of  $V_{GS,BA1}$  and  $V_{GS,BA2}$  are adjusted to optimize the best PAE.

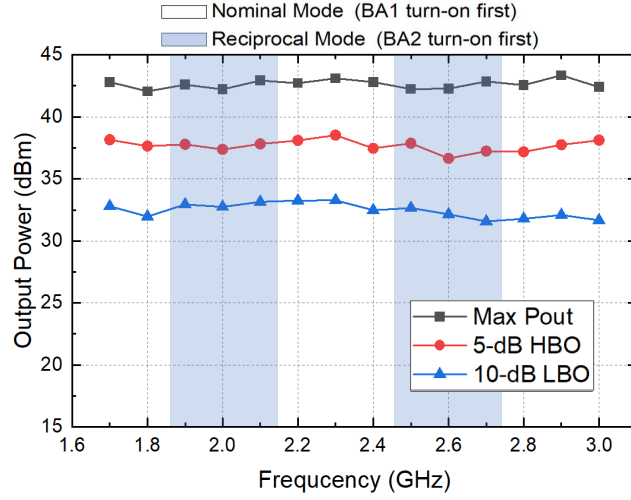


Figure 4.19: Measured output power at various OBO levels from 1.7 to 3.0 GHz.

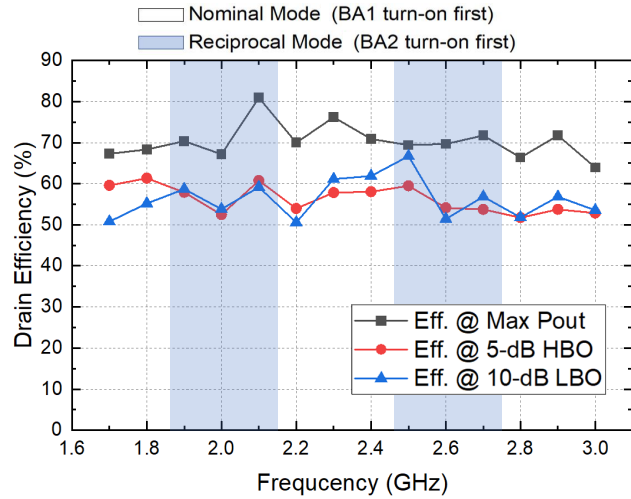


Figure 4.20: Measured DE at various OBO levels from 1.7 to 3.0 GHz.

#### 4.4.1 Continuous-Wave Measurement

The continuous-wave measurement is carried out with a CW power sweep inside the operating frequency band from 1.7 to 3.0 GHz. The CW signal is generated by a vector signal generator, and then boosted by a broadband linear driver amplifier to a sufficiently high level for driving the device under test (DUT). The output power is measured using power sensor and spectrum analyzer.



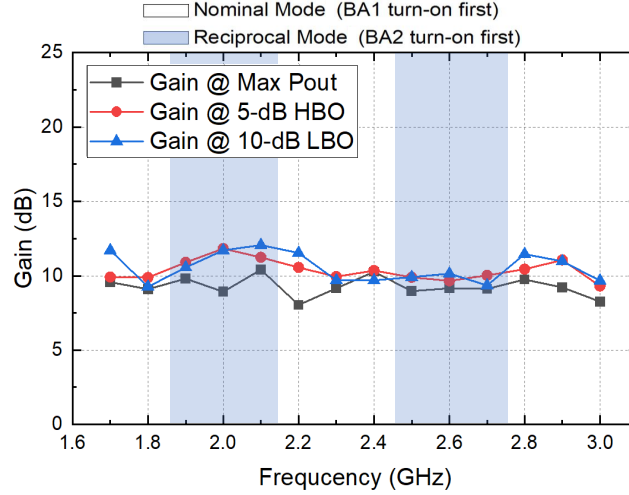


Figure 4.21: Measured gain at various OBO levels from 1.7 to 3.0 GHz.

Table 4.1: State-of-the-Art of Wideband Load-Modulated Power Amplifiers

Ref. / Year	Architecture	Freq. (GHz)	FBW (%)	$P_{\text{Max}}$ (dBm)	DE @ $P_{\text{Max}}$ (%)	DE @ HBO (%)	DE @ LBO (%)
[21] 2018	3-Way DPA	2.0-2.6	26	43.6-45.4	53-76	46-58@5 dB*	41-48@8 dB
[22] 2019	3-Way DPA	1.6-2.6	48	45.5-46	53-66	47-57@5 dB*	50-53@9.5 dB
[49] 2018	3-Way DPA	0.6-0.9	40	46.1-46.9	51.1-78	54-65@5 dB*	42-64@9.5 dB*
[40] 2016	DPA	1.6-2.2	31.6	46-47	60-71	-	51-55@10 dB
[50] 2018	DPA	1.5-3.8	86.8	42.3-43.4	42-63	40-55@5 dB*	22-40@10 dB*
[20] 2019	DEPA	2.55-3.8	40	48.8-49.8	54-67	38-46@5 dB*	47-60@8 dB
[74] 2020	DPA	2.8-3.55	23.62	43-45	66-78	55-65@5 dB*	50-60.6@10 dB
[54] 2020	Dual-Mode DPA	1.52-4.68	102	41.5	54-71	45-60@5 dB*	37-50@10 dB* <sup>†</sup>
[24] 2017	RF-Input LMBA	0.7-0.85	19	42	57-70	-	30-35@10 dB* <sup>†</sup>
[29] 2017	RF-Input LMBA	1.8-3.8	71	44	46-70	30-51@5 dB*	20-25@10 dB* <sup>†</sup>
[42] 2018	Dual-Input LMBA	1.7-2.5	38	48-48.9	48-58*	38-46@5 dB*	33-45@10 dB* <sup>†</sup>
[55] 2020	PD-LMBA	1.5-2.7	57	43	58-72	48-60@5 dB	47-58@10 dB
[75] 2020	CM-LMBA	1.45-2.45	52	45.6-46.7	67.1-77.9	46-55@5 dB*	37-43@10 dB
[69] 2021	ALMBA	0.55-2.2	120	41-43	49-82	44-60@5 dB	39-64@10 dB
[70] 2021	H-ALMBA	0.55-2.2	120	42	55-82	51-69@5 dB	40-61@10 dB
This Work	H-ALMBA	1.7-3.0	55	42-43	63-81	51-62@5 dB	50-66@10 dB

\* Graphically estimated, <sup>†</sup> PAE.

As shown in Fig. 4.19, 42 – 43 dBm peak output power is measured across the entire bandwidth. As shown in Fig. 4.20, the maximum drain efficiencies at peak power are measured in the range of 63 – 81%, the drain efficiencies at 10-dB and 5-dB OBOs are in the range of 50 – 66% and 51 – 62%, respectively. It can be observed from Fig. 4.21 that the gain is maintained around 8 – 13

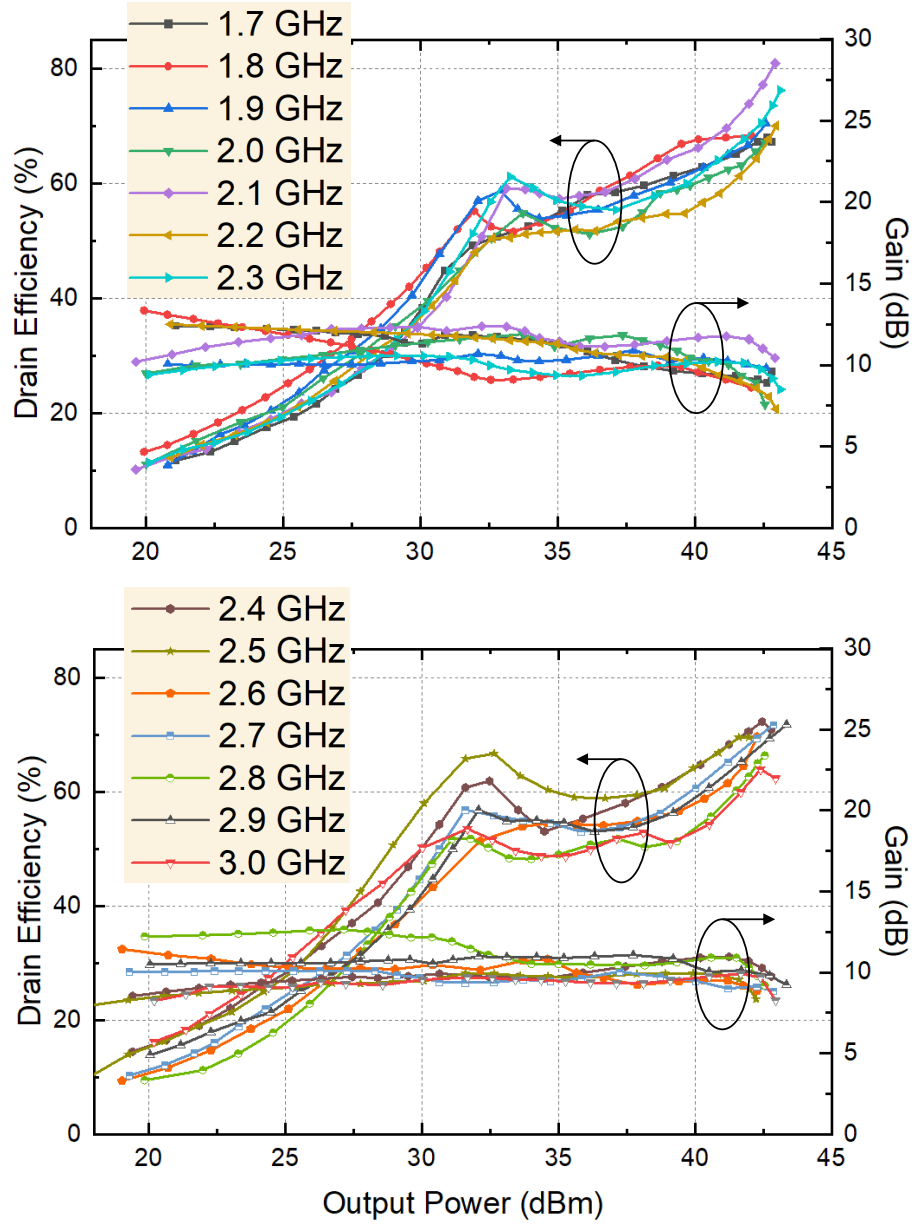


Figure 4.22: Measured DE and gain versus output power from 1.7 to 3.0 GHz.

dB at different OBO level. Fig. 4.22 shows the measured drain efficiency and gain performance versus the output power. Fig. 4.23 is the PAE measurement performance versus the output power, which matches its theoretical results.

Two difference bias modes, nominal mode and reverse mode, are used in CW measurement to

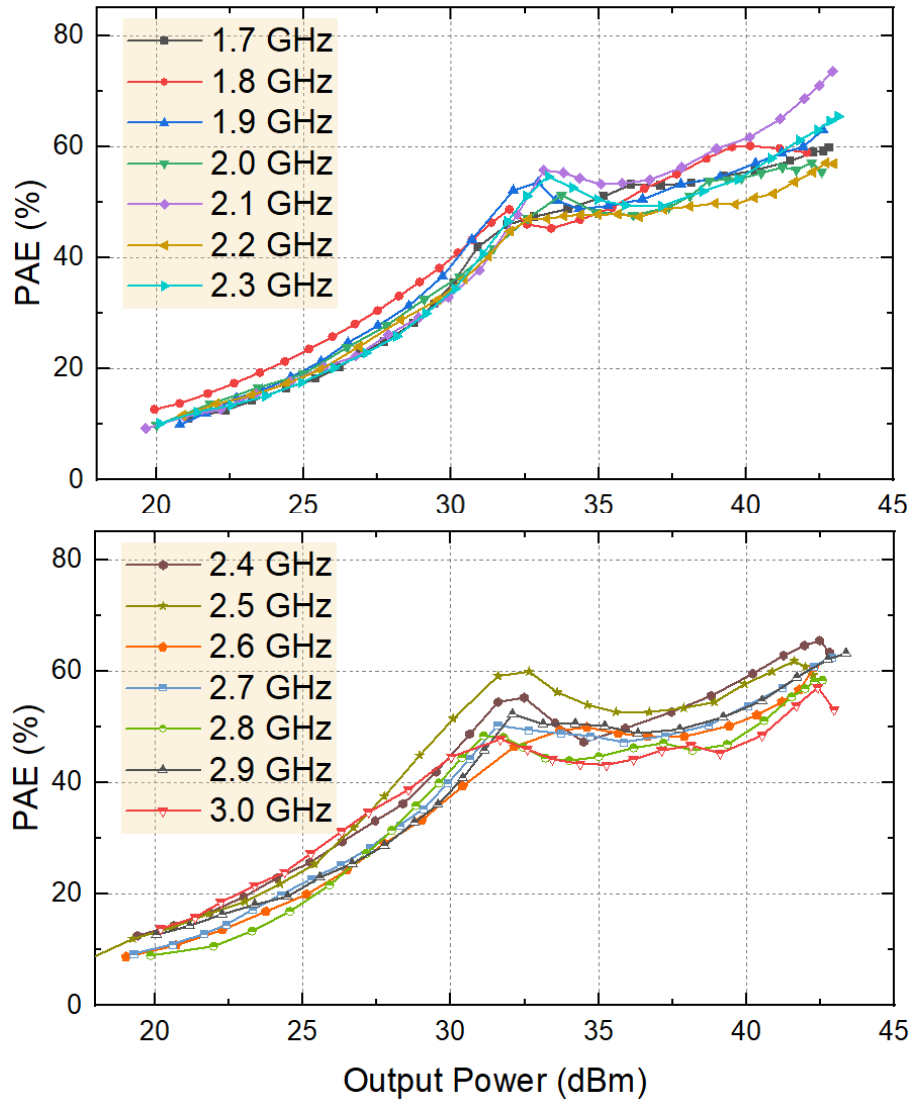


Figure 4.23: Measured PAE versus output power from 1.7 to 3.0 GHz.

ensure the optimal efficiency performance. As shown in Fig. 4.19, Fig. 4.20, Fig. 4.21, the white frequency interval is set to the nominal mode, where BA1 is turned-on first. And the blue frequency interval is set to reverse mode, where BA2 is turned-on first.

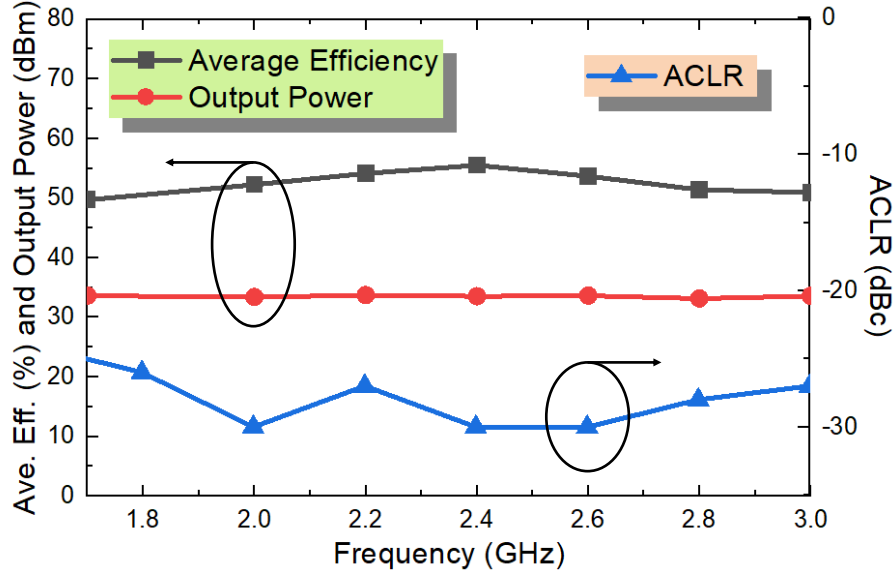


Figure 4.24: Measured average DE, output power and ACLR with 20-MHz 9.5-dB-PAPR LTE signal at 1.7, 2.0, 2.2, 2.4, 2.6, 2.8 and 3.0 GHz.

#### 4.4.2 Modulated Measurement

To evaluate the linearity and efficiency performance of the proposed PA under modulated signal stimulation, 20-MHz LTE signals with 10-dB PAPR are used to test the proposed H-ALMBA at 1.7, 2.0, 2.2, 2.4, 2.6, 2.8 and 3.0 GHz. The modulated-signal is generated and analyzed by a Keysight PXIe vector transceiver (VXT M9421). The generated LTE signal is further boosted by a linear pre-amplifier (ZHL-5W-422+) to a sufficient level for driving the developed prototype. The measurement results at an average output power around 32 dBm are presented in Fig. 4.24. The H-ALMBA achieves a high average efficiency of 50% – 56% over the target frequency band. The ACLR of most measured frequencies are higher than 27 dB without any digital predistortion. Due to the load modulation of CA, the over-driving issue of CA is greatly alleviated. As a result, the overall linearity of H-ALMBA has a better performance compared with PD-LMBA [55]. The measured output PSD are shown in Fig. 4.25. The performance of the prototype PA is summarized and compared with other published works in Table I. This proposed H-ALMBA greatly enhances

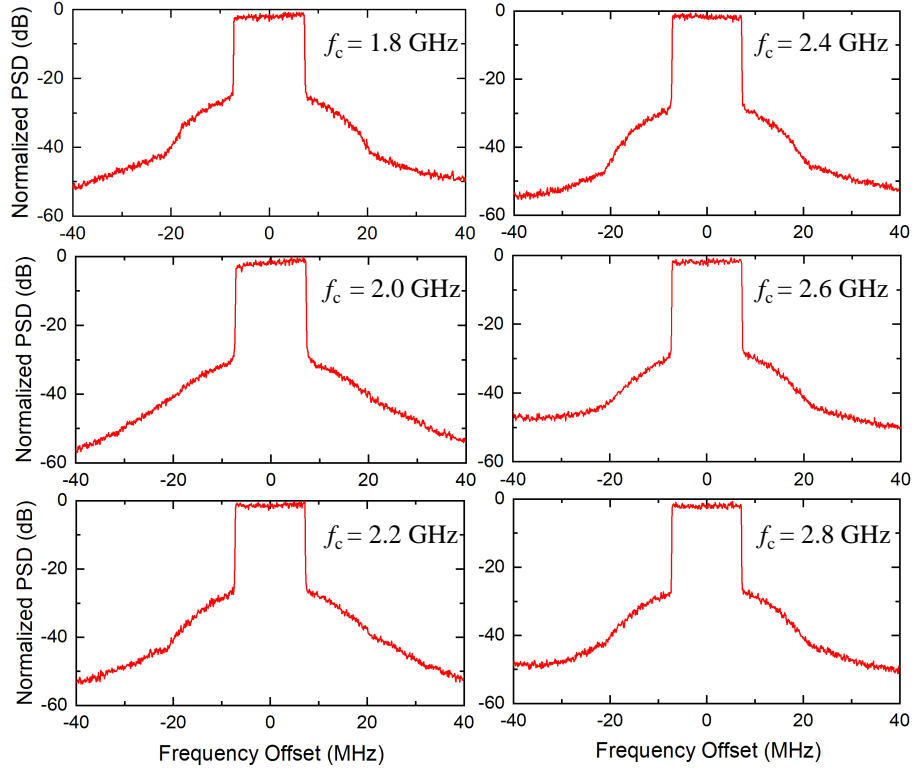


Figure 4.25: Output spectrum from modulated measurement using a 20-MHz 9.5-dB-PAPR LTE signal centered at 1.8, 2.0, 2.2, 2.4, 2.6 and 2.8 GHz.

the entire back-off region efficiency down to 10-dB compared with the other LMBA architecture; while compared with the 3-way DPA, great advantage in ultra-bandwidth has been proved in the proposed H-ALMBA.

#### 4.5 Conclusion

Based on the ALMBA theory, this paper proposes a new high-order load modulation mode, as well as its detailed design method and experimental validation. Through rigorous analysis and derivation, the design space of the load-modulation PA based on the quadrature coupler is further expanded with three-way modulation. In this new H-ALMBA mode, the asymmetry of the

balanced amplifier is realized by setting different thresholds for BA1 and BA2, which leads to a hybrid load modulation combining a Doherty-like region (CA and BA1) and an ALMBA region (with all three amplifiers). As a result, a high-order load modulation can be formed like a three-way Doherty PA, resulting in an extended power back-off range and enhanced overall efficiency. Moreover, the H-ALMBA not only mitigates the CA over-driving issue in PD-LMBA but also inherits its wideband nature through proper phase alignment. The proposed theory and design method are experimentally verified using a developed hardware prototype, which is able to efficiently amplify the signals with 10-dB PAPR within a fractional bandwidth of 55%. This design greatly expands the design space of original LMBA and provides a promising solution for next generation multi-band and energy-efficient wireless transmitters.

## **CHAPTER 5: HIGHLY MINIATURIZED AND WIDEBAND 3-dB QUADRATURE HYBRID USING SLOW-WAVE COUPLED LINE**

This chapter is based in part on the previously published article listed below. I have permission from my co-authors and publishers to use the work listed below in my dissertation. ["Highly Miniaturized and Wideband 3-dB Quadrature Hybrid Using Slow-Wave Coupled Line," 2021 IEEE MTT-S International Microwave Symposium (IMS), 2021, pp. 247-250.].

### **5.1 Introduction**

Nowadays, there is an overwhelming resurgence of balanced amplifier for its strong resilience to load mismatch that widely occurs in the emergent 5G massive MIMO systems due to the mutual coupling between multiple closely located antenna elements. On the other hand, the application and operational horizon of balanced amplifier has been substantially extended, forming a variety of new load modulation modes, including series/parallel quasi-balanced Doherty power amplifiers (QB-DPAs) [76] and various load modulated balanced amplifiers (LMBAs) [77, 78, 69]. Not only do these advanced architectures offer enhanced back-off efficiency, extended dynamic power range, and wide RF bandwidth, but also the mismatch-resilient operation is enabled through reconfiguration over different modes. Fig. 5.1 illustrates the entire family of quadrature-coupler-based PAs with different configuration of the output isolation port.

As being widely recognized, the major bottleneck for practically realizing the balanced PA and its variants lies in the compact, low-loss, and wideband implementation of the quadrature couplers. With the physical dimension proportional to a guided wavelength, the conventional branch-line and coupled-line couplers are very bulky at microwave frequencies, and the bulkiness is exacerbated

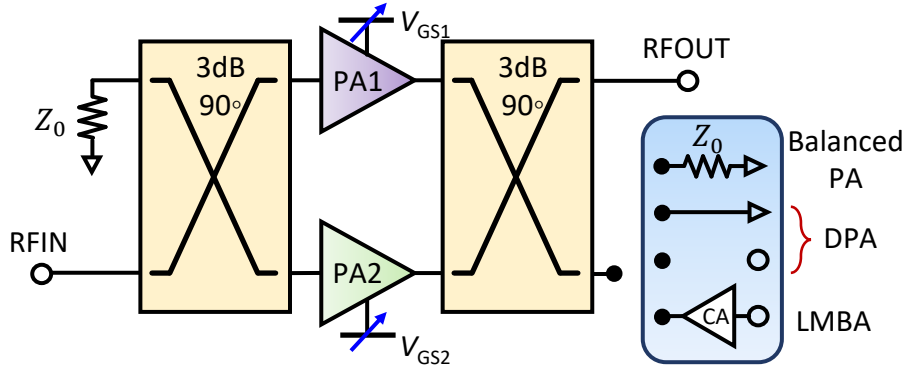


Figure 5.1: The entire series of quadrature-coupler-based PAs (CA: control amplifier, DPA: Doherty PA, LMBA: load modulated balanced amplifier).

for wideband designs [79, 80, 81]. The Lange couplers require very small line width and spacing, which are usually not compatible with standard PCB process but more suitable for IC processes (however very lossy). Recently, artificial slow-wave structures have shown promising potential in miniaturizing the quadrature couplers.

Inspired by the slow-wave coupled-line presented in [82], this paper redesigned the physical structure with enormously enhanced coupling strength which enables the implementation of 3-dB quadrature hybrid coupler. It is for the first time demonstrated that the designed slow-wave quadrature coupler can achieve the same bandwidth and frequency response as a three-section branch-line quadrature hybrid, while offering a characteristic dimension down to  $\lambda/15$ . Compared to the counterpart of wideband branch-line coupler, the proposed slow-wave coupler reduces 99.4% of the circuit area, as shown in Fig. 5.2. Further, the slow-wave quadrature coupler can be designed with different characteristic impedance which enables co-design with the balanced PAs.



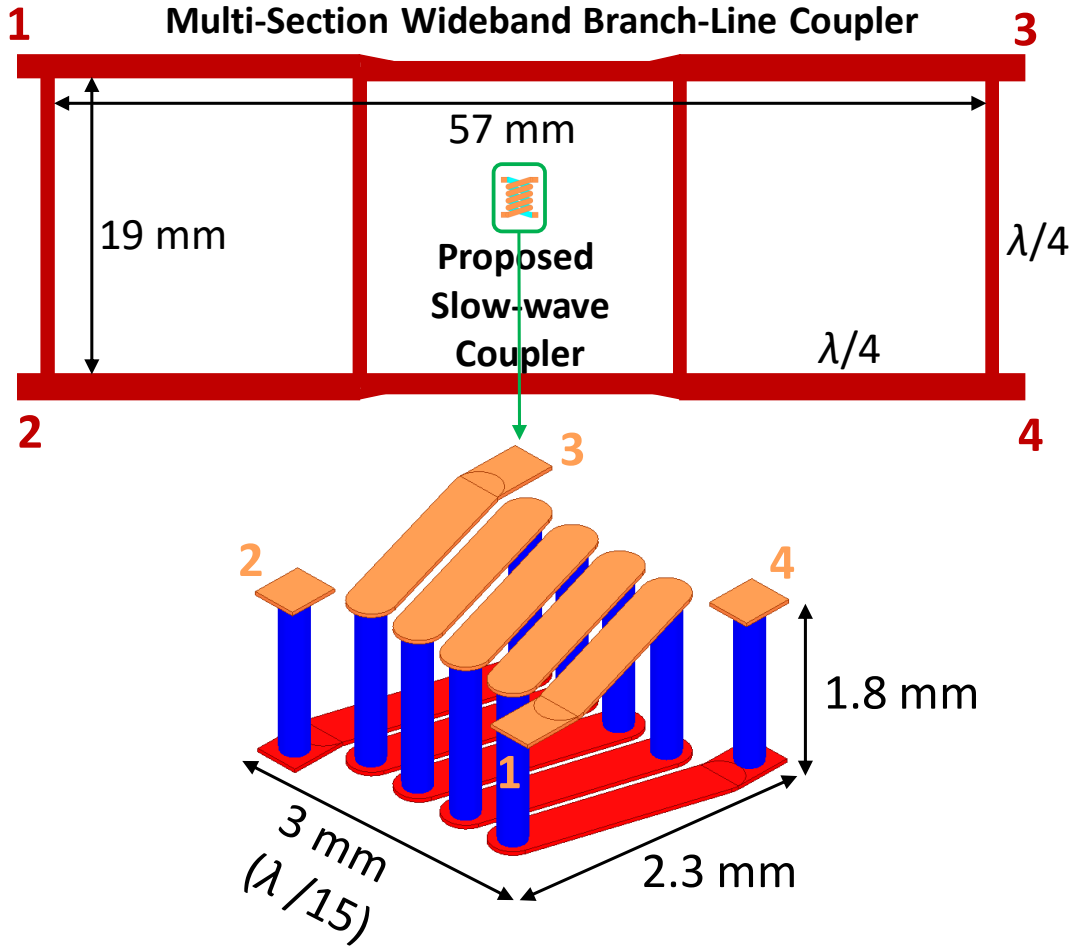


Figure 5.2: The circuit size comparison of the proposed wideband 3-dB slow-wave coupler and conventional branch line coupler with the same performance.

## 5.2 Analysis of Symmetric Slow-Wave Coupling Structure

The symmetric slow-wave coupling structure can be regarded as a cascade of multi-unit cells. Fig. 5.3 shows the effective lumped circuit model of a small unit cell with a four-port coupled line structure of parallel self-capacitance  $C$ , series self-inductance  $L$ , coupling capacitor  $C_M$  and mutual inductance  $L_M$ . By applying the even and odd mode analysis, the four-port symmetric circuit can be decomposed into an equivalent series inductance  $L_{e/o}$  and a shunt capacitance  $C_{e/o}$  [82]. The

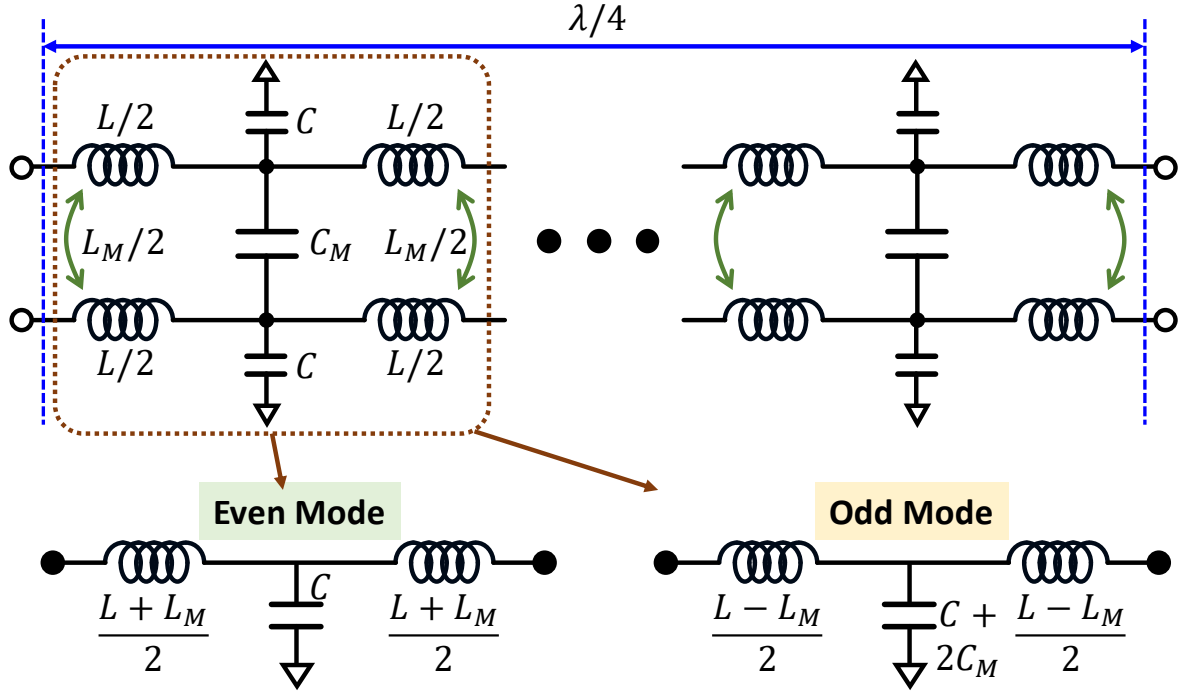


Figure 5.3: The even and odd mode analysis of the equivalent lumped circuit model of symmetric coupled lines.

relationship between  $L_{e/o}$  and  $C_{e/o}$  can be obtained as follows

$$L_e = L + L_M; \quad C_e = C; \quad (5.1)$$

$$L_o = L - L_M; \quad C_o = C + 2C_M. \quad (5.2)$$

This cascade of unit cells is equivalent to a transmission line with propagation constant  $\alpha_{e/o} + j\beta_{e/o}$  and line characteristic impedance  $Z_{0e/o}$  in even and odd modes.

The slow-wave factor (SWF), defined as the wavelength ratio of a free-space wave to a guided wave, is a normalized phase constant. In general case, the SWF and line impedance of the even

and odd modes can be approximated as

$$SWF_{e/o} = \beta_{e/o}/c \approx (c/d)\sqrt{L_{e/o}C_{e/o}}; \quad (5.3)$$

$$Z_{0e/o} = \sqrt{L_{e/o}/C_{e/o}}\sqrt{1 - (\omega^2 L_{e/o}C_{e/o})/4}. \quad (5.4)$$

where  $d$  is the electrical length of a unit cell, and  $c$  is the speed of light. It can be deduced from (5.4) that  $L_e C_e = L_o C_o$  has to be enforced to equalize the phase velocity of the even and odd mode.

Through the derivation of (1) and (2), it can be found that the same modal phase velocity can be obtained only when  $L_M$  is larger than 0. Positive mutual inductance will increase the even mode  $SWF_e$ , but will decrease the odd mode  $SWF_o$ . Coupling capacitors only help to increase odd  $SWF_o$ . From (1) – (4), it can be concluded that under the condition of phase equilibrium, the characteristic impedance of the even mode line should be greater than the characteristic impedance of the odd mode. As a very important parameter for quadrature hybrid, the voltage coupling coefficient is defined in [83] as

$$C_V = (Z_{0e} - Z_{0o})/(Z_{0e} + Z_{0o}). \quad (5.5)$$

### 5.3 Design Considerations of Slow-Wave Coupler

In this design, the slow-wave structure is composed of multiple coupling lines with coupling enhancement functions, as depicted in Figs. 5.2 and 5.4. The circuits of different layers are connected by dense vias, forming an interlaced symmetric 3-D metal structure between the two layers. A large number of quasi-lumped inductors and capacitors can be synthesized within small unit cells, which results in a slow-wave effect and provides appropriate impedance for each line. At the same time,

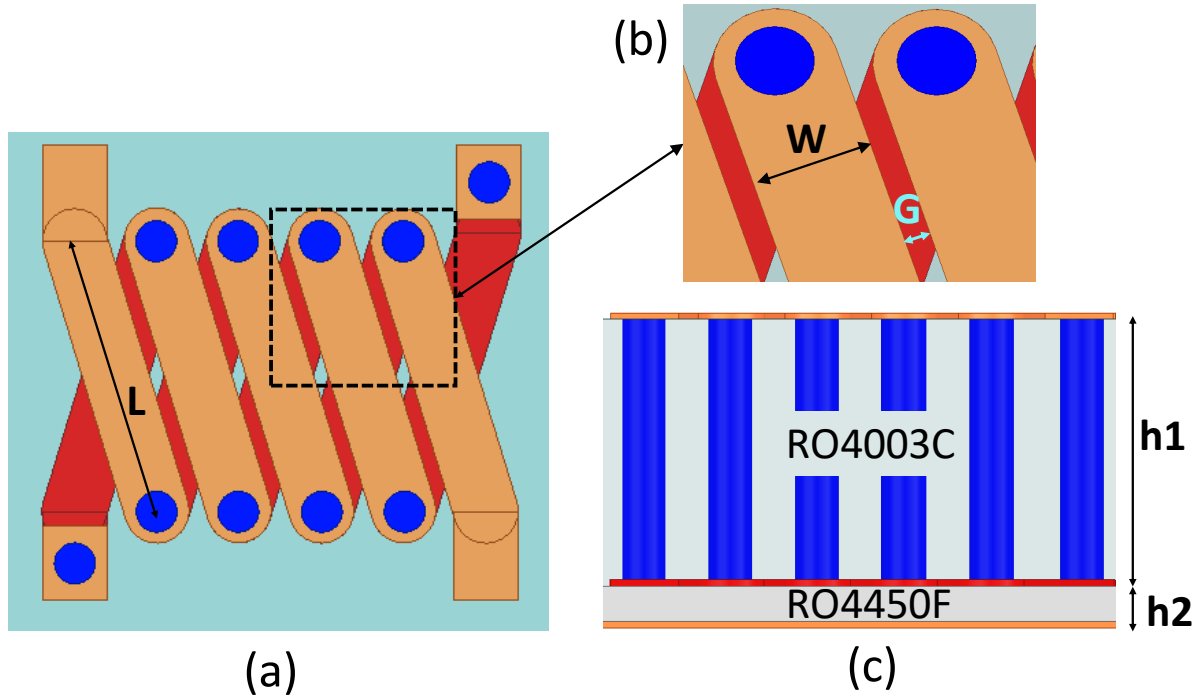


Figure 5.4: Diagram of the proposed compact slow-wave coupler. (a) top view, (b) enlarged of unit cell view, (c) side view.  $h_1$ : dielectric thickness between top and mid layer;  $h_2$ : dielectric thickness between mid and bottom layer.

the multi-layer 3-D folded inductors are wound together to form a parallel coupled inductor. In addition to the paralleled inductive and capacitive couplings, the slow-wave structure also restricts and guides the magnetic field by having more magnetic flux linkages between coupled inductors, so that the inductive coupling can be significantly enhanced.

Fig. 5.4 shows the schematic diagram of the circuit layout and cross-section view. According to (5), the coupling coefficient  $C_V$  can be improved by increasing  $Z_{0e}$  and reducing  $Z_{0o}$ . This requires increasing  $L_M$  and  $C_M$ , while  $L_M$  plays a more significant role based on (1) and (2). The coupling strength and load impedance can be tuned by changing trace width  $W$  and the spacing  $G$ , and the center frequency can be controlled by adjusting the trace length  $L$ . It is worth noting that the arrangement of vias connecting the top layer to the middle layer forms a high-density inductor

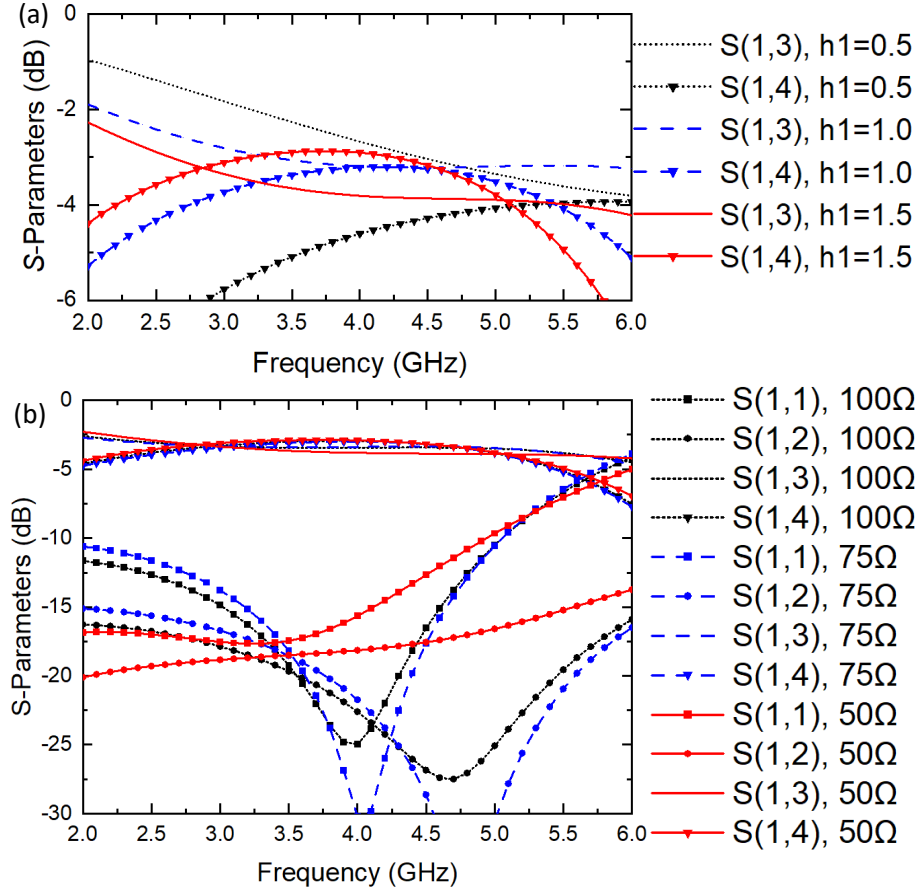


Figure 5.5: (a) S-parameters simulated results with different  $h_1$  (mm),  $\epsilon = 3.55$ ; (b) S-parameters simulated results with different load impedance.

array, so the inductive coupling  $L_M$  can be effectively enhanced by increasing the thickness of  $h_1$ .

#### 5.4 Simulation and Measurement Results

The design targets for a low loss and wideband coupler with  $-3$ -dB coupling coefficient. To achieve such a high coupling strength (i.e.,  $> 3$  dB at the center frequency), it is necessary to minimize the spacing between traces. Considering the limitation of standard PCB processes, the spacing  $G$  is set to the minimum of 0.08 mm. In order to further enhance the coupling coefficient,

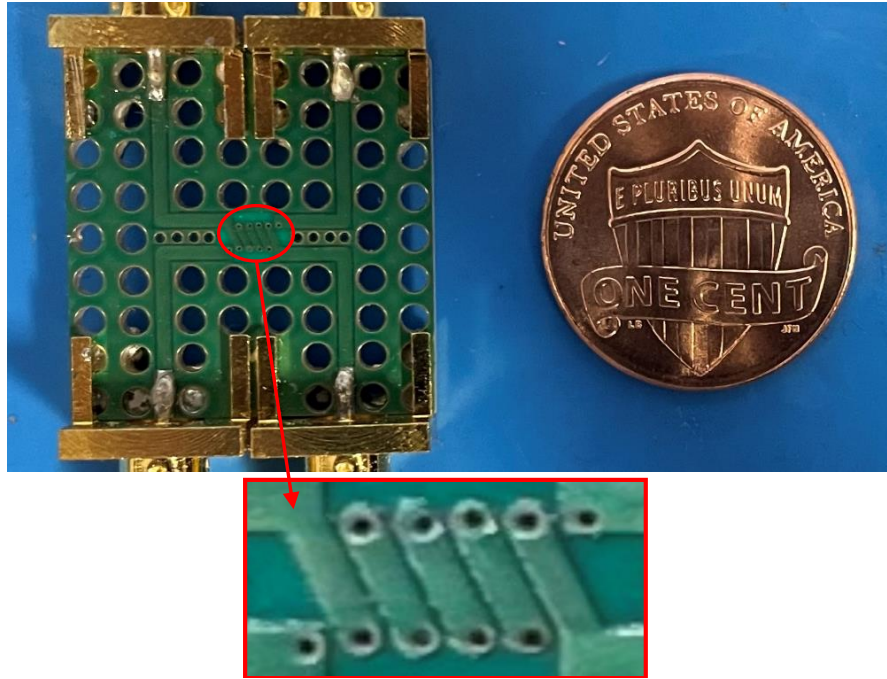


Figure 5.6: Photograph of fabricated 3-dB slow-wave quadrature hybrid.

the length of the via can be increased to obtain higher inductive coupling by increasing the thickness of  $h_1$ . Fig. 5.5 shows the HFSS simulation results. It can be seen from Fig. 5.5(a) that the coupling coefficient of the circuit is enhanced with the increase of  $h_1$ . With a large  $h_1$  of 1.5 mm, a clear wideband response of  $-3$ -dB quadrature hybrid can be achieved. Then, to result in a center frequency of 3.5 GHz, the trace length  $L$  is set to 1.8 mm and the trace width  $W$  to 0.4 mm. The above parameters can be re-synthesized for operating at different characteristic impedances, as the results shown in Fig. 5.5(b).

A prototype is fabricated with a two-layer PCB board with 1.5-mm RO4003C on top and 0.2-mm RO4450F on bottom. Fig. 5.6 shows the picture of the prototype. For measurement using VNA, the slow-wave coupler is connected to the SMA connectors through four 50- $\Omega$  CPW lead lines. Fig. 5.7 shows the measurement results. Due to the fabrication tolerance, the center frequency of

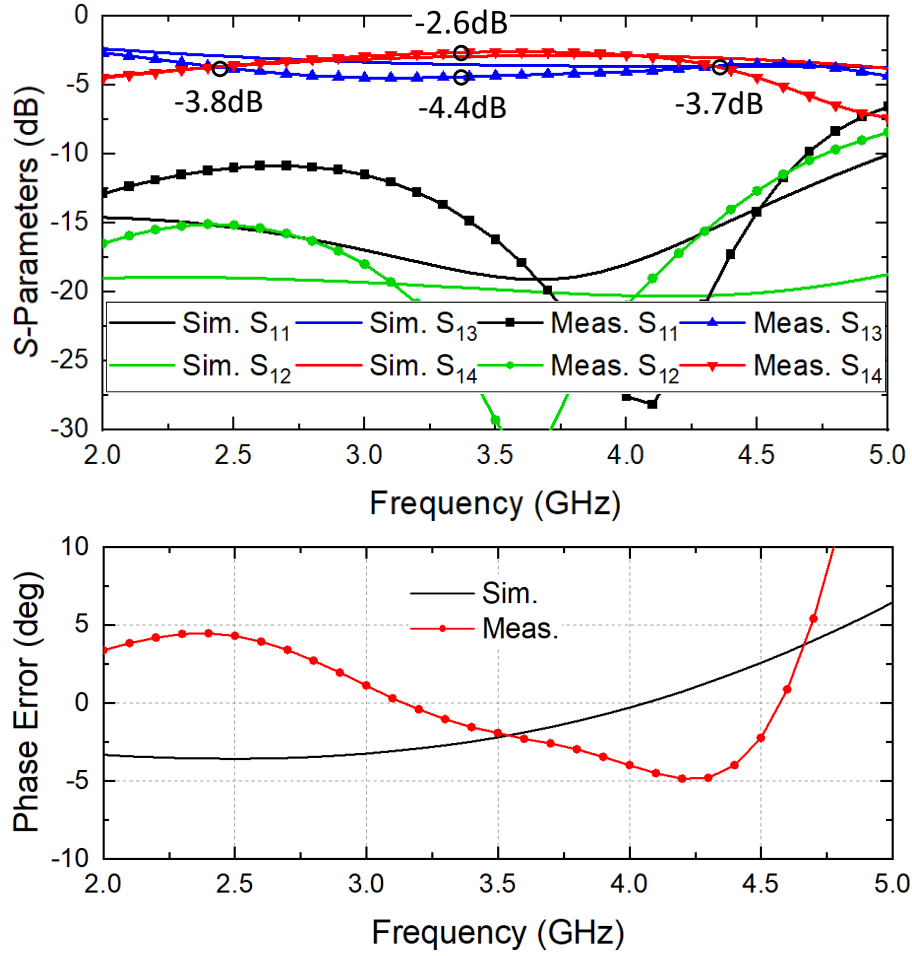


Figure 5.7: Measured S-parameters and phase error of the 3-dB slow-wave quadrature hybrid.

the physical prototype is slightly shifted, but a good agreement between testing and simulation is still observed. The measured return loss is better than 10 dB and combined insertion loss between 0.4 – 0.9 dB. The phase variation is limited to  $\pm 5^\circ$  in 60% fractional bandwidth.

## 5.5 Conclusion

A highly miniaturized 3-dB slow-wave quadrature hybrid covering 2.3 – 4.3 GHz has been successfully demonstrated in this paper. The state-of-the-art results published for the 3-dB quadrature

Table 5.1: Comparison with State-of-the-Art 3-dB Slow-Wave Couplers

Ref.	$f_0$ (GHz)	$\text{FBW}_{\text{IL}}$ (%)	$\angle S(4,1) - \angle S(3,1)$ (deg.)	IL (dB)	$WL/\lambda^2$
[84]	12	21	90	3.5	1.07
[85]	7	7.1	102.5	4.28	0.47
[86]	9.5	14	90	4	0.85
[87]	14.1	41	90	3.3	2.1
[88]	11.15	18	91	3.4-3.6	1.6
This Work	3.3	60	92	3.6-3.8	0.003

couplers are compared in Table 1. Compared with similar designs in the table, this slow-wave quadrature hybrid has an excellent wideband coupler performance along with a very compact size. Moreover, this design leaves much room for adjustment and improvement, and can be applied to different bandwidth and load impedance design requirements. The proposed slow-wave structure is well-suited for the design of the compact RF and mm-wave radio front ends.



## CHAPTER 6: SUMMARY

The 5G deployment is driven by two key factors: system capacity, which will be primarily determined by spectral efficiency; and system cost, which is dominated by energy efficiency. Therefore, the modern wireless communication systems require broadband high efficiency PAs. Load modulated balanced amplifiers have been proposed as solution to traditional and Doherty amplifier limitations. Among a few LMBA configurations, PD-ALMBA is selected as the most promising architecture, with features of free of dynamic phase control, minimum matching required for BAs, performance optimization through CA amplitude and phase control. At the same time, PD-ALMBA and its subsequent improved architectures have great potential in RFIC design, mismatch resilience field and filter co-design, etc. It is believed that in the near future, PD-ALMBA will play an irreplaceable role in 5G, 6G and future communication systems.

## LIST OF REFERENCES

- [1] M. S. Afaqui, E. Garcia-Villegas, and E. Lopez-Aguilera, "IEEE 802.11ax: Challenges and requirements for future high efficiency Wi-Fi," *IEEE Wireless Commun.*, vol. 24, pp. 130–137, Jun. 2017.
- [2] B. Liu, M. Mao, C. C. Boon, P. Choi, D. Khanna, and E. A. Fitzgerald, "A fully integrated Class-J GaN MMIC power amplifier for 5-GHz WLAN 802.11ax application," *IEEE Microw. Wireless Compon. Lett.*, vol. 28, pp. 434–436, May 2018.
- [3] R. Wu, Y. Liu, J. Lopez, C. Schecht, Y. Li, and D. Y. C. Lie, "High-efficiency silicon-based envelope-tracking power amplifier design with envelope shaping for broadband wireless applications," *IEEE Journal of Solid-State Circuits*, vol. 48, pp. 2030–2040, Sep. 2013.
- [4] W. H. Doherty, "A new high efficiency power amplifier for modulated waves," *Proceedings of the Institute of Radio Engineers*, vol. 24, pp. 1163–1182, Sep. 1936.
- [5] R. Darraji, D. Bhaskar, T. Sharma, M. Helaloui, P. Mousavi, and F. M. Ghannouchi, "Generalized theory and design methodology of wideband Doherty amplifiers applied to the realization of an octave-bandwidth prototype," *IEEE Trans. Microw. Theory Techn.*, vol. 65, pp. 3014–3023, Aug. 2017.
- [6] V. Camarchia, M. Pirola, R. Quaglia, S. Jee, Y. Cho, and B. Kim, "The Doherty power amplifier: Review of recent solutions and trends," *IEEE Trans. Microw. Theory Techn.*, vol. 63, pp. 559–571, Feb. 2015.
- [7] A. Banerjee, L. Ding, and R. Hezar, "High efficiency multi-mode outphasing RF power amplifier in 45nm CMOS," in *European Solid-State Circuits Conf. (ESSCIRC)*, pp. 168–171, Sep. 2015.

- [8] J. Hur, H. Kim, O. Lee, K. Kim, F. Bien, K. Lim, C. Lee, and J. Laskar, “A multilevel Class-D CMOS power amplifier for an out-phasing transmitter with a nonisolated power combiner,” *IEEE Trans. on Circuits and Systems II: Express Briefs*, vol. 63, pp. 618–622, Jul. 2016.
- [9] R. A. Beltran, “Broadband outphasing transmitter using Class-E power amplifiers,” in *IEEE MTT-S Int. Microw. Symp. Dig.*, pp. 67–70, Jun. 2019.
- [10] S. Chung, P. A. Godoy, T. W. Barton, D. J. Perreault, and J. L. Dawson, “Asymmetric multilevel outphasing transmitter using Class-E PAs with discrete pulse width modulation,” in *IEEE MTT-S Int. Microw. Symp. Dig.*, pp. 264–267, May 2010.
- [11] K. Chen and D. Peroulis, “Design of adaptive highly efficient GaN power amplifier for octave-bandwidth application and dynamic load modulation,” *IEEE Trans. Microw. Theory Techn.*, vol. 60, pp. 1829–1839, Jun. 2012.
- [12] C. Sánchez-Pérez, M. Özen, C. M. Andersson, D. Kuylenskierna, N. Rorsman, and C. Fager, “Optimized design of a dual-band power amplifier with SiC varactor-based dynamic load modulation,” *IEEE Trans. Microw. Theory Techn.*, vol. 63, pp. 2579–2588, Aug. 2015.
- [13] H. M. Nemati, C. Fager, U. Gustavsson, R. Jos, and H. Zirath, “Design of varactor-based tunable matching networks for dynamic load modulation of high power amplifiers,” *IEEE Trans. Microw. Theory Techn.*, vol. 57, pp. 1110–1118, May 2009.
- [14] H. M. Nemati, H. Cao, B. Almgren, T. Eriksson, and C. Fager, “Design of highly efficient load modulation transmitter for wideband cellular applications,” *IEEE Trans. Microw. Theory Techn.*, vol. 58, pp. 2820–2828, Nov. 2010.
- [15] C. M. Andersson, D. Gustafsson, K. Yamanaka, E. Kuwata, H. Otsuka, M. Nakayama, Y. Hirano, I. Angelov, C. Fager, and N. Rorsman, “Theory and design of Class-J power amplifiers

- with dynamic load modulation,” *IEEE Trans. Microw. Theory Techn.*, vol. 60, pp. 3778–3786, Dec. 2012.
- [16] H. Jang, P. Roblin, C. Quindroit, Y. Lin, and R. D. Pond, “Asymmetric Doherty power amplifier designed using model-based nonlinear embedding,” *IEEE Trans. Microw. Theory Techn.*, vol. 62, pp. 3436–3451, Dec. 2014.
- [17] H. Oh, H. Kang, H. Lee, H. Koo, M. Kim, W. Lee, W. Lim, C. Park, K. C. Hwang, K. Lee, and Y. Yang, “Doherty power amplifier based on the fundamental current ratio for asymmetric cells,” *IEEE Trans. Microw. Theory Techn.*, vol. 65, pp. 4190–4197, Nov. 2017.
- [18] B. Merrick, J. King, and T. Brazil, “A wideband sequential power amplifier,” in *IEEE MTT-S Int. Microw. Symp. Dig.*, pp. 1–3, Jun. 2014.
- [19] P. Saad, R. Hou, R. Hellberg, and B. Berglund, “A 1.8–3.8-GHz power amplifier with 40% efficiency at 8-dB power back-off,” *IEEE Trans. Microw. Theory Techn.*, vol. 66, pp. 4870–4882, Nov. 2018.
- [20] P. Saad, R. Hou, R. Hellberg, and B. Berglund, “The continuum of load modulation ratio from Doherty to traveling-wave amplifiers,” *IEEE Trans. Microw. Theory Techn.*, vol. 67, pp. 5101–5113, Dec. 2019.
- [21] S. Chen, W. Wang, X. Kuiwen, and G. Wang, “A reactance compensated three-device Doherty power amplifier for bandwidth and back-off range extension,” *Wireless Commun. and Mobile Computing*, vol. 2018, pp. 1–10, May 2018.
- [22] J. Xia, W. Chen, F. Meng, C. Yu, and X. Zhu, “Improved three-stage Doherty amplifier design with impedance compensation in load combiner for broadband applications,” *IEEE Trans. Microw. Theory Techn.*, vol. 67, pp. 778–786, Feb. 2019.

- [23] D. J. Shepphard, J. Powell, and S. C. Cripps, “An efficient broadband reconfigurable power amplifier using active load modulation,” *IEEE Microw. Wireless Compon. Lett.*, vol. 26, pp. 443–445, Jun. 2016.
- [24] P. H. Pednekar and T. W. Barton, “RF-input load modulated balanced amplifier,” in *IEEE MTT-S Int. Microw. Symp. Dig.*, pp. 1730–1733, Jun. 2017.
- [25] D. Collins, R. Quaglia, J. Powell, and S. Cripps, “Experimental characterization of a load modulated balanced amplifier with simplified input power splitter,” in *2018 Asia-Pacific Microwave Conf. (APMC)*, pp. 461–463, Nov. 2018.
- [26] T. Cappello, P. Pednekar, C. Florian, S. Cripps, Z. Popovic, and T. W. Barton, “Supply- and load-modulated balanced amplifier for efficient broadband 5G base stations,” *IEEE Trans. Microw. Theory Techn.*, vol. 67, pp. 3122–3133, Jul. 2019.
- [27] H. Jeon, Y. Park, Y. Huang, J. Kim, K. Lee, C. Lee, and J. S. Kenney, “A triple-mode balanced linear CMOS power amplifier using a switched-quadrature coupler,” *IEEE Journal of Solid-State Circuits*, vol. 47, pp. 2019–2032, Sep. 2012.
- [28] T. Cappello, P. H. Pednekar, C. Florian, Z. Popovic, and T. W. Barton, “Supply modulation of a broadband load modulated balanced amplifier,” in *IEEE MTT-S Int. Microw. Symp. Dig.*, pp. 304–307, Jun. 2018.
- [29] P. H. Pednekar, E. Berry, and T. W. Barton, “RF-input load modulated balanced amplifier with octave bandwidth,” *IEEE Trans. Microw. Theory Techn.*, vol. 65, pp. 5181–5191, Dec. 2017.
- [30] P. H. Pednekar, W. Hallberg, C. Fager, and T. W. Barton, “Analysis and design of a Doherty-like RF-input load modulated balanced amplifier,” *IEEE Trans. Microw. Theory Techn.*, vol. 66, pp. 5322–5335, Dec. 2018.

- [31] Y. Cao, H. Lyu, and K. Chen, "Load modulated balanced amplifier with reconfigurable phase control for extended dynamic range," in *IEEE MTT-S Int. Microw. Symp. Dig.*, pp. 1335–1338, Jun. 2019.
- [32] J. Xia, X. Zhu, L. Zhang, J. Zhai, and Y. Sun, "High-efficiency GaN Doherty power amplifier for 100-MHz LTE-advanced application based on modified load modulation network," *IEEE Trans. Microw. Theory Techn.*, vol. 61, pp. 2911–2921, Aug. 2013.
- [33] A. Barakat, M. Thian, V. Fusco, S. Bulja, and L. Guan, "Toward a more generalized Doherty power amplifier design for broadband operation," *IEEE Trans. Microw. Theory Techn.*, vol. 65, pp. 846–859, Mar. 2017.
- [34] K. B. Niclas, W. T. Wilser, R. B. Gold, and W. R. Hitchens, "Application of the two-way balanced amplifier concept to wide-band power amplification using gaas mesfet's," *IEEE Trans. Microw. Theory Techn.*, vol. 28, pp. 172–179, Mar 1980.
- [35] Y. Cao, H. Lyu, and K. Chen, "Wideband Doherty power amplifier in quasi-balanced configuration," in *IEEE 20th Wireless and Microw. Tech. Conf. (WAMICON)*, pp. 1–4, Apr. 2019.
- [36] A. Barthwal, K. Rawat, and S. Koul, "Wideband tri-stage Doherty power amplifier with asymmetric current ratios," in *IEEE MTT-S Int. Microw. and RF Conf. (IMaRC)*, pp. 1–4, Dec. 2016.
- [37] X. A. Nghiem, J. Guan, and R. Negra, "Broadband sequential power amplifier with Doherty-type active load modulation," *IEEE Trans. Microw. Theory Techn.*, vol. 63, pp. 2821–2832, Sep. 2015.
- [38] S. C. Cripps, "RF power amplifiers for wireless communications," 2nd ed., Norwood, MA, USA: Artech House, Inc., pp. 323–326, 2006.

- [39] J. Kim, B. Fehri, S. Boumaiza, and J. Wood, "Power efficiency and linearity enhancement using optimized asymmetrical Doherty power amplifiers," *IEEE Trans. Microw. Theory Techn.*, vol. 59, pp. 425–434, Feb. 2011.
- [40] J. Xia, M. Yang, and A. Zhu, "Improved Doherty amplifier design with minimum phase delay in output matching network for wideband application," *IEEE Microw. Wireless Compon. Lett.*, vol. 26, pp. 915–917, Nov. 2016.
- [41] D. J. Shepphard, J. Powell, and S. C. Cripps, "A broadband reconfigurable load modulated balanced amplifier (LMBA)," in *IEEE MTT-S Int. Microw. Symp. Dig.*, pp. 947–949, Jun. 2017.
- [42] R. Quaglia and S. Cripps, "A load modulated balanced amplifier for telecom applications," *IEEE Trans. Microw. Theory Techn.*, vol. 66, pp. 1328–1338, Mar. 2018.
- [43] Innovative Power Products, NY, USA. Surface Mount 90 Degree Hybrid Couplers. [Online]. Available: <https://innovativepp.com/product/ipp-7118/>, Accessed on: Sep. 15, 2019.
- [44] M. Muraguchi, T. Yukitake, and Y. Naito, "Optimum design of 3-dB branch-line couplers using microstrip lines," *IEEE Trans. Microw. Theory Techn.*, vol. 31, pp. 674–678, Aug. 1983.
- [45] Cree, Inc., Wolfspeed, CA, USA. gallium nitride transistor. [Online]. Available: [www.cree.com/RF](http://www.cree.com/RF).
- [46] K. Chen and D. Peroulis, "Design of highly efficient broadband Class-E power amplifier using synthesized low-pass matching networks," *IEEE Trans. Microw. Theory Techn.*, vol. 59, pp. 3162–3173, Dec. 2011.

- [47] K. Chen and D. Peroulis, "Design of broadband highly efficient harmonic-tuned power amplifier using in-band continuous Class-F<sup>-1</sup>/F mode transferring," *IEEE Trans. Microw. Theory Techn.*, vol. 60, pp. 4107–4116, Dec. 2012.
- [48] P. Saad, C. Fager, H. Cao, H. Zirath, and K. Andersson, "Design of a highly efficient 2–4-GHz octave bandwidth GaN-HEMT power amplifier," *IEEE Trans. Microw. Theory Techn.*, vol. 58, pp. 1677–1685, Jul. 2010.
- [49] A. Barthwal, K. Rawat, and S. K. Koul, "A design strategy for bandwidth enhancement in three-stage Doherty power amplifier with extended dynamic range," *IEEE Trans. Microw. Theory Techn.*, vol. 66, pp. 1024–1033, Feb. 2018.
- [50] J. J. M. Rubio, V. Camarchia, M. Pirola, and R. Quaglia, "Design of an 87% fractional bandwidth Doherty power amplifier supported by a simplified bandwidth estimation method," *IEEE Trans. Microw. Theory Techn.*, vol. 66, pp. 1319–1327, Mar. 2018.
- [51] A. K. Kwan, M. Younes, O. Hammi, M. Helaoui, and F. M. Ghannouchi, "Linearization of a highly nonlinear envelope tracking power amplifier targeting maximum efficiency," *IEEE Microw. Wireless Compon. Lett.*, vol. 27, no. 1, pp. 82–84, 2017.
- [52] M. Özen, K. Andersson, and C. Fager, "Symmetrical Doherty power amplifier with extended efficiency range," *IEEE Trans. Microw. Theory Techn.*, vol. 64, pp. 1273–1284, April 2016.
- [53] P. Saad, R. Hou, R. Hellberg, and B. Berglund, "An 80W power amplifier with 50% efficiency at 8db power back-off over 2.6-3.8 GHz," in *IEEE MTT-S Int. Microw. Symp. Dig.*, pp. 1328–1330, June 2019.
- [54] J. Pang, Z. Dai, Y. Li, M. Li, and A. Zhu, "Multiband dual-mode Doherty power amplifier employing phase periodic matching network and reciprocal gate bias for 5G applications," *IEEE Trans. Microw. Theory Techn.*, pp. 1–16, 2020.



- [55] Y. Cao and K. Chen, "Pseudo-Doherty load-modulated balanced amplifier with wide bandwidth and extended power back-off range," *IEEE Trans. Microw. Theory Techn.*, 2020.
- [56] J. Pang, Y. Li, M. Li, Y. Zhang, X. Y. Zhou, Z. Dai, and A. Zhu, "Analysis and design of highly efficient wideband RF-input sequential load modulated balanced power amplifier," *IEEE Trans. Microw. Theory Techn.*, pp. 1–13, 2020.
- [57] P. Saad, R. Hou, R. Hellberg, and B. Berglund, "Ultra-wideband Doherty-like power amplifier," in *IEEE MTT-S Int. Microw. Symp. Dig.*, pp. 1215–1218, 2018.
- [58] H. Lyu and K. Chen, "Balanced-to-Doherty mode-reconfigurable power amplifier with high efficiency and linearity against load mismatch," *IEEE Trans. Microw. Theory Techn.*, pp. 1–1, 2020.
- [59] Y. Cao and K. Chen, "Dual-octave-bandwidth RF-input pseudo-Doherty load modulated balanced amplifier with  $\geq 10$ -dB power back-off range," in *IEEE MTT-S Int. Microw. Symp. Dig.*, 2020.
- [60] X. Y. Zhou, S. Y. Zheng, W. S. Chan, S. Chen, and D. Ho, "Broadband efficiency-enhanced mutually coupled harmonic postmatching doherty power amplifier," *IEEE Trans. Circuits Syst. I: Regular Papers*, vol. 64, no. 7, pp. 1758–1771, 2017.
- [61] H. Kang, H. Lee, W. Lee, H. Oh, W. Lim, H. Koo, C.-s. Park, K. C. Hwang, K.-Y. Lee, and Y. Yang, "Octave bandwidth doherty power amplifier using multiple resonance circuit for the peaking amplifier," *IEEE Trans. Circuits Syst. I: Regular Papers*, vol. 66, no. 2, pp. 583–593, 2019.
- [62] H. Lyu, Y. Cao, and K. Chen, "Doherty-to-balanced switchable power amplifier," in *IEEE MTT-S Int. Microw. Symp. Dig.*, pp. 1339–1342, 2019.

- [63] H. Lyu, Y. Cao, and K. Chen, “Linearity-enhanced quasi-balanced doherty power amplifier with mismatch resilience through series/parallel reconfiguration for massive mimo,” *IEEE Trans. Microw. Theory Techn.*, vol. 69, no. 4, pp. 2319–2335, 2021.
- [64] C. Liang, P. Roblin, Y. Hahn, Z. Popovic, and H.-C. Chang, “Novel outphasing power amplifiers designed with an analytic generalized doherty–chireix continuum theory,” *IEEE Trans. Circuits Syst. I: Regular Papers*, vol. 66, no. 8, pp. 2935–2948, 2019.
- [65] C. Li, F. You, S. He, X. Tang, W. Shi, and J. Wang, “High-efficiency power amplifier employing minimum-power harmonic active load modulator,” *IEEE Trans. Circuits Syst. II: Express Briefs*, vol. 66, no. 8, pp. 1371–1375, 2019.
- [66] V. Carrubba, A. L. Clarke, M. Akmal, J. Lees, J. Benedikt, P. J. Tasker, and S. C. Cripps, “On the extension of the continuous Class-F mode power amplifier,” *IEEE Trans. Microw. Theory Techn.*, vol. 59, no. 5, pp. 1294–1303, 2011.
- [67] M. Akbarpour, F. M. Ghannouchi, and M. Helaloui, “Current-biasing of power-amplifier transistors and its application for ultra-wideband high efficiency at power back-off,” *IEEE Trans. Microw. Theory Techn.*, vol. 65, no. 4, pp. 1257–1271, 2017.
- [68] Y. Zhao, X. Li, C. Gai, C. Liu, T. Qi, B. Hu, X. Hu, W. Chen, M. Helaloui, and F. M. Ghannouchi, “Theory and design methodology for reverse-modulated dual-branch power amplifiers applied to a 4g/5g broadband gan mmic pa design,” *IEEE Trans. Microw. Theory Techn.*, vol. 69, no. 6, pp. 3120–3131, 2021.
- [69] Y. Cao, H. Lyu, and K. Chen, “Asymmetrical load modulated balanced amplifier with continuum of modulation ratio and dual-octave bandwidth,” *IEEE Trans. Microw. Theory Techn.*, vol. 69, no. 1, pp. 682–696, 2021.

- [70] Y. Cao and K. Chen, “Hybrid asymmetrical load modulated balanced amplifier with wide bandwidth and three-way-doherty efficiency enhancement,” *IEEE Microw. Wireless Compon. Lett.*, pp. 1–1, 2021.
- [71] H. Lyu and K. Chen, “Hybrid load-modulated balanced amplifier with high linearity and extended dynamic range,” *IEEE Microw. Wireless Compon. Lett.*, pp. 1–1, 2021.
- [72] Y. Xu, J. Pang, X. Wang, and A. Zhu, “Three-stage load modulated power amplifier with efficiency enhancement at power back-off,” *IEEE Trans. Microw. Theory Techn.*, vol. 69, no. 6, pp. 3107–3119, 2021.
- [73] G. R. Nikandish, R. B. Staszewski, and A. Zhu, “Unbalanced power amplifier: An architecture for broadband back-off efficiency enhancement,” *IEEE J. Solid-State Circuits*, vol. 56, no. 2, pp. 367–381, 2021.
- [74] M. Li, J. Pang, Y. Li, and A. Zhu, “Bandwidth enhancement of doherty power amplifier using modified load modulation network,” *IEEE Trans. Circuits Syst. I, Reg. Papers*, vol. 67, no. 6, pp. 1824–1834, 2020.
- [75] J. Pang, C. Chu, Y. Li, and A. Zhu, “Broadband rf-input continuous-mode load-modulated balanced power amplifier with input phase adjustment,” *IEEE Trans. Microw. Theory Techn.*, vol. 68, no. 10, pp. 4466–4478, 2020.
- [76] H. Lyu, Y. Cao, and K. Chen, “Linearity-enhanced quasi-balanced Doherty power amplifier with mismatch resilience through series/parallel reconfiguration for massive MIMO,” *IEEE Transactions on Microwave Theory and Techniques*, pp. 1–1, 2021.
- [77] D. J. Shepphard, J. Powell, and S. C. Cripps, “A broadband reconfigurable load modulated balanced amplifier (LMBA),” in *2017 IEEE MTT-S International Microwave Symposium (IMS)*, pp. 947–949, 2017.

- [78] Y. Cao and K. Chen, "Pseudo-Doherty load-modulated balanced amplifier with wide bandwidth and extended power back-off range," *IEEE Transactions on Microwave Theory and Techniques*, vol. 68, no. 7, pp. 3172–3183, 2020.
- [79] H. Yoon and B. Min, "Two section wideband 90° hybrid coupler using parallel-coupled three-line," *IEEE Microwave and Wireless Components Letters*, vol. 27, no. 6, pp. 548–550, 2017.
- [80] P. Bhowmik, T. Moyra, and P. K. Deb, "Size miniaturization of 3 dB branch line coupler by using open stubs," in *2015 2nd International Conference on Signal Processing and Integrated Networks (SPIN)*, pp. 642–645, 2015.
- [81] C. Tang, C. Tseng, and K. Hsu, "Design of wide passband microstrip branch-line couplers with multiple sections," *IEEE Transactions on Components, Packaging and Manufacturing Technology*, vol. 4, no. 7, pp. 1222–1227, 2014.
- [82] H. Ma and H. Y. D. Yang, "Novel slow-wave coupled lines with coupling enhancement," in *2011 IEEE MTT-S International Microwave Symposium*, pp. 1–4, 2011.
- [83] D. Pozar in *Microwave Engineering*, pp. 337–345, 3rd ed. New York: Wiley, 2005.
- [84] B. Liu, W. Hong, Y. Wang, Q. Lai, and K. Wu, "Half mode substrate integrated waveguide (HMSIW) 3-dB coupler," *IEEE Microwave and Wireless Components Letters*, vol. 17, no. 1, pp. 22–24, 2007.
- [85] T. R. Jones and M. Daneshmand, "The characterization of a ridged half-mode substrate-integrated waveguide and its application in coupler design," *IEEE Transactions on Microwave Theory and Techniques*, vol. 64, no. 11, pp. 3580–3591, 2016.
- [86] G. H. Zhai, W. Hong, K. Wu, J. X. Chen, P. Chen, J. Wei, and H. J. Tang, "Folded half mode substrate integrated waveguide 3 dB coupler," *IEEE Microwave and Wireless Components Letters*, vol. 18, no. 8, pp. 512–514, 2008.

- [87] H. Jin, Y. Zhou, Y. M. Huang, S. Ding, and K. Wu, “Miniaturized broadband coupler made of slow-wave half-mode substrate integrated waveguide,” *IEEE Microwave and Wireless Components Letters*, vol. 27, no. 2, pp. 132–134, 2017.
- [88] M. Bertrand, H. El Dirani, E. Pistono, D. Kaddour, V. Puyal, and P. Ferrari, “A 3-dB coupler in slow wave substrate integrated waveguide technology,” *IEEE Microwave and Wireless Components Letters*, vol. 29, no. 4, pp. 270–272, 2019.